Control of electronic and optical properties of single and double quantum dots via electroelastic fields

von der Fakultät für Naturwissenschaften der Technischen Universität Chemnitz
genehmigte Dissertation zur Erlangung des akademischen Grades

doctor rerum naturalium

(Dr. rer. nat.)

vorgelegt von **M.Sc. Eugenio Zallo**

geboren am 12.09.1983 in Frascati

Eingereicht am 08. Oktober 2014

Gutachter:
Prof. Dr. Oliver G. Schmidt
Prof. Dr. Armando Rastelli

Tag der Verteidigung: 12. März 2015
http://nbn-resolving.de/urn:nbn:de:bsz:ch1-qucosa-162870

Abstract

Semiconductor quantum dots (QDs) are fascinating systems for potential applications in quantum information processing and communication, since they can emit single photons and polarisation entangled photons pairs on demand. The asymmetry and inhomogeneity of real QDs has driven the development of a universal and fine post-growth tuning technique. In parallel, new growth methods are desired to create QDs with high emission efficiency and to control combinations of closely-spaced QDs, so-called "QD molecules" (QDMs). These systems are crucial for the realisation of a scalable information processing device after a tuning of their interaction energies.

In this work, GaAs/AlGaAs QDs with low surface densities, high optical quality and widely tuneable emission wavelength are demonstrated, by infilling nanoholes fabricated by droplet etching epitaxy with different GaAs amounts. A tuning over a spectral range exceeding 10 meV is obtained by inducing strain in the dot layer. These results allow a fine tuning of the QD emission to the rubidium absorption lines, increasing the yield of single photons that can be used as hybrid semiconductor-atomic-interface.

By embedding InGaAs/GaAs QDs into diode-like nanomembranes integrated onto piezoelectric actuators, the first device allowing the QD emission properties to be engineered by large electroelastic fields is presented. The two external fields reshape the QD electronic properties and allow the universal recovery of the QD symmetry and the generation of entangled photons, featuring the highest degree of entanglement reported to date for QD-based photon sources.

A method for controlling the lateral QDM formation over randomly distributed nanoholes, created by droplet etching epitaxy, is demonstrated by depositing a thin GaAs buffer over the nanoholes. The effect on the nanohole occupancy of the growth parameters, such as InAs amount, substrate temperature and arsenic overpressure, is investigated as well. The QD pairs show good optical quality and selective etching post-growth is used for a better characterisation of the system.

For the first time, the active tuning of the hole tunnelling rates in vertically aligned InGaAs/GaAs QDM is demonstrated, by the simultaneous application of electric and strain fields, optimising the device concept developed for the single QDs. This result is relevant for the creation and control of entangled states in optically active QDs. The modification of the electronic properties of QDMs, obtained by the combination of the two external fields, may enable controlled quantum operations.

Keywords: III-V semiconductors, quantum dots, quantum dot molecules, exciton fine structure splitting, indium arsenide, gallium arsenide, strain, ferroelectric crystal, anticrossing, photoluminescence, tunnelling, entangled photon pairs

“Il faut cultiver notre jardin”
Candide, chapitre XXX
Voltaire

Acknowledgements

This work would not have been possible without the help of several people.

First I would like to thank Prof. Dr. Oliver G. Schmidt for the opportunity to perform research in his group, for his supervision, guidance, availability and supports.

I thank Prof. Dr. Armando Rastelli for the great time spent in the QD group in Dresden before moving to Linz, for his supervision and guidance, for excellent ideas and scientific discussions, for help with all the software programming and for his struggling attitude to overcome the next challenge.

I am grateful to Dr. Paola Atkinson for transferring her idea of science, for introducing many different topics and several techniques in the first period of my PhD, above all the MBE, and for proofreading this thesis very thoroughly. Her deep understanding of physics was crucial for the study of GaAs/AlGaAs QDs and the works on devices with QDs. Her guidance was invaluable over the all PhD period.

I am also grateful to Dr. Rinaldo Trotta for sharing his knowledge in optics, material science and processing, giving always good suggestions, motivating for going beyond my limits. The work on InGaAs/GaAs QDs in section 4.2 was mainly the result of this team synergy. The time I spent in the optics lab was very helpful for my future development as a scientist.

Thanks must go to Dr. Santosh Kumar for introducing the optics lab, always willing to help and discuss, for his constant good mood and more importantly for nicely stretching and performing the photon antibunching of my GaAs/AlGaAs QD sample in section 4.1.2.

I would like to thank Dr. Johannes D. Plumhof for the great working atmosphere at the beginning of my PhD, the scientific discussions, the advices and the great social activities organised.

Jörg R. Schröter was very important with software programming using LabView to successfully implement all the stage protocols we needed.

I am very thankful to Dr. Yongheng Huo for the pleasant atmosphere in the MBE lab even during the hard times of fixing problems and chamber opening, for his availability, nice ideas, to have continued my initial work on Al droplet etching of AlGaAs surfaces with great success, for discussions of any kind, for sharing his life philosophy.

Many thanks to Dr. Vlastimil Křápek for the $\mathbf{k}\cdot\mathbf{p}$ calculations and the scientific discussions. Dr. Carmine Ortix was also important for the understanding of theoretical growth aspects for the lateral InGaAs/GaAs QD pairs, for helping with modelling the fine structure splitting in InGaAs/GaAs QDs under electroelastic fields and for suggestions on the analysis of the strain effect on the vertical InGaAs/GaAs QDMs.

Many thanks to Barbara Eichler for AFM measurement, wire bonding of strain and electric tuneable devices, to Ronny Engelhard, Dr. Christoph Deneke and Dr. Dominic J. Thurmer for technical assistance in the MBE lab, to Dr. Daniel Grimm and

Dr. Dominic J. Thurmer for technical assistance in the clean room, to Anja Bonatto-Minella for TEM measurements and to Prof. Dr. Kathrin Dörr and Dr. Andreas Herklotz for help with the piezoelectric actuators.

Thanks also to Dr. Fei Ding and Jiaxiang Zhang for many fruitful discussions about device processing, technical assistance in the optics lab and helping for the cross-correlation measurements of InGaAs/GaAs QDMs.

Dr. Nika Akopian and Prof. Dr. Val Zwiller performed the high resolution measurement of my GaAs/AlGaAs QD sample in section 4.1.2. Dr. Rinaldo Trotta, Johannes Wildmann and Prof. Dr. Armando Rastelli performed the cross-correlation measurements of my InGaAs/GaAs QD sample and reconstructed the density matrix in section 4.2.4.

I would like to thank Prof. Dr. Amalia Patanè for giving me the chance to work for a short period in her lab in Nottingham, for very good advices and scientific discussions.

I am very grateful to Ulrike Steere, Anja Schanze and Grit Rötzer for helping with all the administrative works and much more.

I thank all the colleagues from IIN, in particular Martin Bauer, Dr. Stefan Baunack, Stefan Böttner, Dr. Carlos Cesar Bof Bufon, Peixuan Chen, Prof. Dr. Vladimir Fomin, Dr. Georgios Katsaros, Abbas Madani, Dr. Elisabeth Mägerl, Dr. Ingolf Mönch, Bianca Höfer, Dr. Fabio Pezzoli, Dr. Roman Rezaev, Dr. Jianjun Zhang.

Most of all, I am grateful to my parents, my dear Daniela and my friends who have supported and encouraged me along the way.

Table of contents

List of tables

List of figures

List of abbreviations, constants and symbols

Abbreviations

AC	anticrossing
AFM	atomic force microscope
APD	avalanche photo diode
CB	conduction band
FSS	fine structure splitting
FWHM	full width at half maximum
HBT	Hanbury Brown and Twiss
HH	heavy hole
LED	light emitting diode
LH	light hole
MBE	molecular beam epitaxy
ML	monolayer
PL	photoluminescence
PMN-PT	lead magnesium niobate-lead titanate
QCSE	quantum confined Stark effect
QD	quantum dot
QDM	quantum dot molecule
QW	quantum well
RHEED	reflection high energy electron diffraction
SK	Stranski-Krastanow

UHV	ultra high vacuum
VB	valence band
VW	Volmer-Weber
$\mathbf{X}^0$	neutral exciton
$\mathbf{X}^+$	positively charged exciton
$\mathbf{X}^-$	negatively charged exciton
XX	biexciton
WL	wetting layer

Constants

Planck constant	$h = 6.626 \times 10^{-34}$ Js
Electron rest mass	$m_0 = 9.109 \times 10^{-31}$ Kg
Boltzmann constant	$k_B = 1.381 \times 10^{-23}$ JK^{-1}
Surface diffusion coefficient at 500 K	$D = 4.2 \times 10^{-6}$ cm^{2}s^{-1}
Elastic compliance tensor elements at $T = 10$ K	$s_{11} = 0.0114$ GPa^{-1} $s_{12} = -0.0035$ GPa^{-1} $s_{44} = 0.0163$ GPa^{-1}
Hydrostatic deformation potentials of the GaAs bandgap	$a = -8.4$ eV
Hydrostatic deformation potentials of the GaAs VB	$a_v = -7.17$ eV
Hydrostatic deformation potentials of the GaAs CB	$a_c = -1.23$ eV
Tetragonal deformation potentials of the GaAs VB	$b_v = -1.67$ eV
Rhomboedral deformation potentials of the GaAs VB	$d_v = -4.6$ eV
HH effective mass (growth direction)	$m^*_{\mathrm{hh,z}}/m_0 = 0.333$
LH effective mass (growth direction)	$m^*_{\mathrm{lh,z}}/m_0 = 0.094$

Symbols

a_0	lattice constant of unstrained crystal
a_ε	lattice constant of strained crystal
AC_1	anticrossing of the single hole
AC_2	anticrossing of the positively charged exciton
β	polarisability
C_{ij}	direct coulomb interaction
$\Delta\theta$	angle between two neutral excitonic states
E_B	binding energy
E_g	energy bandgap or bandgap
ε_{ij}	strain tensor
$\varepsilon_{//}$	strain perpendicular to F_p
$\varepsilon_\perp$	strain parallel to F_p
$\epsilon(\mathbf{r})$	screened dielectric function
F_c	coercive field of the PMN-PT substrate
F_d	electric field applied to the diode structure
F_p	electric field applied to the PMN-PT substrate
γ_{epi}	epilayer free energy
γ_{int}	interface free energy
γ_{sub}	substrate free energy
$g^{(2)}(\tau)$	2nd-order correlation function
$\mathrm{I}_{\mathrm{L,H}}$	PL integrated intensity for the low,high excitonic energy component
J	angular momentum
J_{eh}	exchange interaction
J_z	projection of J on the z-axis
$\mathbf{k}$	wavevector
λ	wavelength in the corresponding medium
λ_D	diffusion length
m^*	effective mass
ρ	nanohole/dot number density
σ_{ij}	stress tensor
S	spin momentum
s	fine structure splitting
S_z	projection of S on the z-axis
τ_c	lifetime incorporation adatom
T_c	Curie temperature
T_{sub}	substrate temperature
V_d	voltage applied to the diode structure
V_{bi}	built in voltage
V_p	voltage applied to the PMN-PT substrate
ϕ	angle of QDs elongation axis with respect to [110] crystal direction
X_b	bright excitons
X_d	dark excitons

1. Introduction

The discovery in the early 20th century that the classical laws governing macroscopic objects do not work the same way at the microscopic level marked the birth of the quantum physics [1]. Since then, tremendous progress has been made in the field of atomic and solid state physics, where the quantum behaviour can be exploited for practical applications in daily life. For example, using the property that quantum particles can exist in multiple states at the same time, a modestly sized quantum computer would outperform the largest classical supercomputer, allowing for an exponential amount of computation to take place simultaneously [2–4]. Quantum key distribution, which enables confidentiality of data transmissions of classical information, is another important subgroup of quantum information science. Here, random secret keys can be distributed and transported via entanglement, a quantum process where two particles are linked to each other regardless of how far apart they are [5]. Moreover, highly sensitive measurements of distance and time that were never achieved before could be performed via quantum metrology.
All these operations require the ability to create, control and transmit quantum bits of information, also known as "qubits"−a two-state quantum mechanical system−instead of only one state (1 or 0) as for the classical bit. Several systems have been proposed to realise the qubit, such as an isolated atom, an ion in a trap, a nitrogen vacancy centre and optical lattices, a polarisation state of a photon, nuclear spins in molecules, Josephson junctions, or the spin of electron and holes in quantum dots (QDs).

QDs are nanostructures made of several thousands of atoms showing atomic-like electronic properties. This "artificial atom" behaviour occurs when a small semiconductor nanostructure binds one or more electrons or holes into a localised potential with discrete energy levels. At sufficiently low temperatures electrons and holes can bind forming complexes called excitons. Several unique properties make single QDs advantageous over other optical systems. For example, QDs such as InGaAs/GaAs QDs, which self-assemble during molecular beam epitaxial (MBE) growth, have a very high emission efficiency and their electronic properties are governed by the interplay between quantum confinement, direct Coulomb interactions among charged carriers, exchange and correlation effects [6]. They can generate single photons [7, 8] and can be easily integrated into optoelectronic devices [8], or in photonic crystal cavities [9] together with attractive applications as QD lasers [10]. Moreover, they can act as convenient hosts of spin qubits [11] and are practical for any applications where either optical spin control or coherent interfacing between spin and optical qubits would be required. Rapid optical initialisation and control on the order of picoseconds have been also demonstrated for both electrons and holes [11, 12] in these structures, which could enable extremely fast quantum computers.
However, self-assembled QDs form in random locations because of the stochastic growth

processes and, unlike atoms, the emission properties vary from dot to dot, due to their different composition, size, and shape [13]. QDs with a certain atomic symmetry are required for establishing remote entanglement, which is the motivation for a large-scale quantum networks. In fact, Benson *et al.* proposed in the year 2000 that a similar cascade process to that which produces entangled photons in a single atom could occur in a semiconductor QD, where the biexciton-exciton decay cascade would lead to the emission of polarisation entangled photon pairs [14]. This remarkable property makes them promising building blocks of future solid-state quantum information processing and communication [15–19]. This scheme has the advantage that the photons can be emitted on demand, i.e., using an optical or electrical trigger pulse. The irregularities in the as-grown QDs spoil the entanglement by causing a mismatch in the energies of the emitted photon pairs, called the fine structure splitting (FSS). Although polarisation entangled photons have been experimentally realised [8, 20–22] by cherry picking a dot with very low FSS value and tuning it after growth to values of the order of the radiative linewidth, a universal tuning method to engineer exciton spin degeneracy in almost any QD is still needed.
Besides generating and transmitting qubits, it is necessary to develop concepts for storing them. Due to their long coherence times, atomic vapours could open up the possibility of storing single photons emitted by QDs. First steps in this direction have been made by Akopian *et al.* [23]. Single photons emitted by GaAs/AlGaAs QDs were slowed down by tuning their emission energy into resonance with the middle of the ^{87}Rb D_2 hyperfine absorption lines. In order to make this concept useful for practical applications, high quality single photon sources with limited spectral diffusion and an on-chip fine tuning technique for engineering their optical properties are still required.

Only one or two qubit operations can be carried out using a single dot [24] whereas computation will require arrays of qubits. This drawback pushed the research in the past few years to study coupled QD systems [25, 26]. One potential way to realise a quantum gate for quantum information processing [27–29] is to use interacting QDs, so-called "QD molecules" (QDMs), aligned in different configurations by a variety of techniques [30]. For example, QDMs can be self-assembled during MBE growth as the strain field of a buried QD creates a preferred nucleation site for a second QD on top of the first [31, 32]. The separating barrier between the QD pairs can be engineered, in order to control the alignment and coupling strength between the energy levels [33]. QDMs represent a striking example of the analogy between artificial and natural atomic combinations. Similar to the energy levels in a hydrogen molecule, bonding and anti-bonding states are formed via coherent tunneling [34] of charges in a QDM, giving rise to anticrossing (AC) patterns in the luminescence spectra [35–37]. Recently, control over two spin qubits [38,39] and the reduced dephasing [40] in coupled QDs with respect to single dots have been shown. The use of QDMs as potential sources of higher order entanglement was also investigated [41], due to their capability to preserve the spatial overlaps of excitonic orbitals.
However, it is rather difficult to control the rate of electron/hole tunnelling inside QDMs and a post-growth tuning of the coupling strength in individual QDMs is still sought. This fulfilment would produce better sources of entanglement.

Within this framework this thesis presents a detailed study of the growth, optical

and electronic properties of single III-V QDs and QDMs and explores new technological routes for the realisation of tuneable sources of single photons and entangled photon pairs. The work is organised as follows:
Chapter 2 provides a description of the electronic properties of GaAs, in particular when stress is applied, and the optical properties of semiconductor QDs and QDMs with a review of the state of the art of experimental and theoretical studies. A brief overview of the materials and the experimental details of this work is given in chapter 3. The results are described in chapter 4, divided in four sections.
Section 4.1 deals with the optimisation of GaAs/AlGaAs QDs, obtained by infilling self-assembled nanoholes fabricated by droplet etching epitaxy. Control over the dot density with unprecedentedly narrow excitonic emission lines, and tuning of the emission energy by growth, strain and magnetic fields are demonstrated.
In section 4.2, a device design allowing the simultaneous combination of electric and strain fields on single InGaAs/GaAs QDs is presented, with independent control of the emission energies of the excitonic species. Via these two "knobs", it is always possible to drive the excitons confined in arbitrary QDs towards a universal level crossing and generate highly polarisation-entangled photons.
An alternative and robust method for the formation of InGaAs/GaAs QD pairs over nanoholes created by droplet etching epitaxy is given in section 4.3. The effect of growth parameters such as indium deposition amount, substrate temperature and arsenic overpressure on this system is investigated.
In section 4.4, a strain-tuneable InGaAs/GaAs QDM-based device is demonstrated with the possibility to actively tune the coupling strength of holes, by externally induced strains and electric fields. Finally, the effect of these external perturbations on the FSS and the polarisation angle are discussed.

2. Theoretical background

This chapter provides background on semiconductor QDs and QDMs. At first, the electronic properties of GaAs are described with the theoretical methods for calculating the electronic band as well as the influence of stress. Then, the optical properties of QDs and QDMs are discussed in detail together with a review of the state of the art of experimental and theoretical studies.

2.1. Electronic properties of GaAs

GaAs is a semiconductor compound with direct bandgap emitting ∼1.424 eV at room temperature, corresponding to light in the near infrared at 870.7 nm. The transition of an electron across the direct gap is accompanied by the emission of light. This is because the crystal momenta (**k** vectors) in the Brillouin zone[1] of the minimal energy-state in the conduction band (CB) and the maximal energy-state in the valence band (VB) are the same. As a result, GaAs-based heterostructures are optimal for light emitting diodes (LEDs) and solid-state lasers [42, 43].

The crystal structure of GaAs is called zincblende. It consists of two fcc (face-centered cubic) lattices shifted along the body diagonal by a quarter of the cubic cell diagonal, as shown in Fig. 2.1(a), where the violet and red points mark the positions of the gallium and arsenic atoms, respectively.

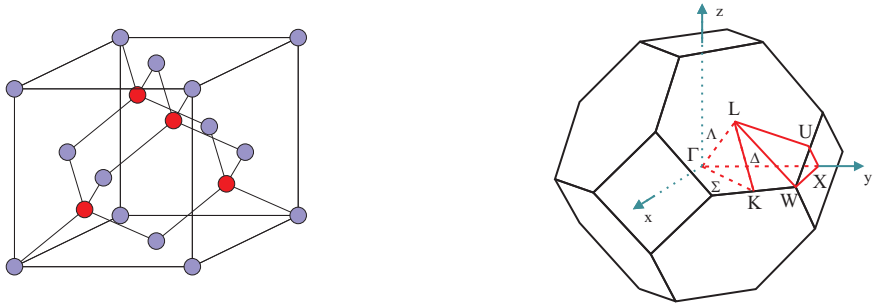

Figure 2.1.: (a) Crystal structure and (b) Brillouin zone of the GaAs.

The Brillouin zone of the GaAs is shown in Fig. 2.1(b): Γ denotes the centre of the Brillouin zone corresponding to the wavevector $\mathbf{k} = 0$. L and X denote the centres of the hexagonal and square faces of the Brillouin zone. Λ and Δ denote the segments joining Γ and L and X, respectively. Figure 2.2(a) shows the calculated electronic band structures with wavevectors between the centre and the border of the Brillouin zone along the directions Γ-L and Γ-X.

[1]The Brillouin zone is defined as the smallest volume entirely enclosed by the planes that are perpendicular bisectors of the wavevectors connecting a lattice site to its nearest neighbours.

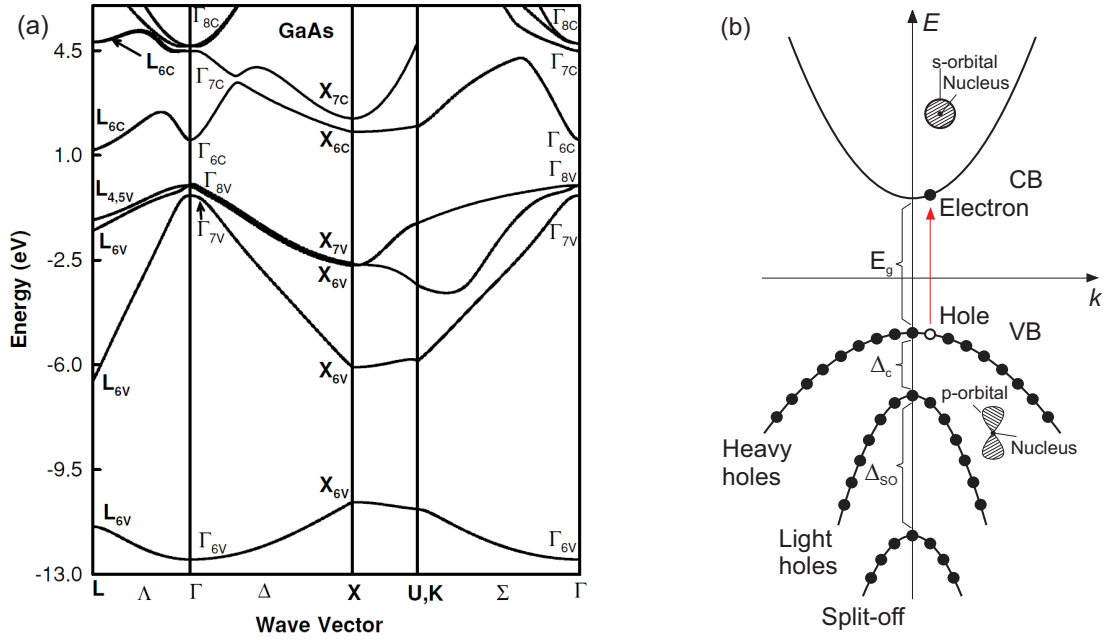

Figure 2.2.: (a) Calculated electronic band structures along lines of high symmetry for the GaAs. (b) Sketch of the GaAs band structure close to $\mathbf{k} = 0$. Figures (a) from Ref. [44] and (b) readapted from Ref. [45].

Electrons moving in the periodic potential of positively charged ion cores in a crystal are described by Bloch waves in the Brillouin zone. In intrinsic GaAs at 0 K the VB is completely full and the CB completely empty. As the temperature is increased a few electrons are thermally excited to the CB. The vacancies left in the VB are called *holes* and they are described as particles with positive charge [46]. If only the electronic dispersion relationship close to the CB minimum ($\mathbf{k} = 0$) is considered, the energy of electrons can be described by a parabola, as shown in Fig. 2.2(b), originating from s-type atomic orbitals and having spin $S = \frac{1}{2}$ and projection of the spin on the z-axis $S_z = \pm\frac{1}{2}$. The curvature of the bands represents the effective mass $m^* \propto (d^2E/dk^2)^{-1}$. The forbidden energy region between bottom of CB and top of VB is called the bandgap (E_g). The VB consists of three subbands: the light hole (LH) having a larger dispersion hence a smaller mass, the heavy hole (HH) with larger mass and the spin-orbit split-off band [Γ_{7V} in Fig. 2.2(a)]. The last plays a minor role since it is energetically well separated from the above mentioned bands ($\Delta_{SO} = 0.34$ eV [47]). The dispersion of these bands deviates from a parabolic behaviour (band warping) and reflects the cubic symmetry of the crystal.
In unstrained GaAs, the upper two VBs arising from p-type atomic orbitals are energetically degenerate in the Γ-point. In heterostructures and nanostructures, such as a QD, the LH and HH subbands are split (Δ_c) by the confinement and/or strain (see section 2.4.1). As a result, the hole states can be treated to a first approximation as pure HH states [46]. Both VBs have a total angular momentum of $J = \frac{3}{2}$ due to the orbital angular momentum $L = 1$ and spin $S = \pm\frac{1}{2}$. Furthermore, HHs have angular momentum projection $J_z = \pm\frac{3}{2}$ whereas for LHs $J_z = \pm\frac{1}{2}$ [48]. Similarly, the SO band has $J = \frac{1}{2}$ and $J_z = \pm\frac{1}{2}$.

2.2. k·p theory of semiconductors

In this section the **k·p** method, which can describe the electronic band structure of a semiconductor near the Γ-point, will be briefly introduced following Ref. [49].

An ideal crystal with translational symmetry is considered. The wavefunction $\psi(\mathbf{r})$ of an electron subject to an effective periodic potential

$$V(\mathbf{r}+\mathbf{R}_m) = V(\mathbf{r}), \tag{2.1}$$

where $\mathbf{R}_m$ is a translation vector of the lattice, has to satisfy the Schrödinger equation

$$H\psi(\mathbf{r}) = \left[-\frac{\hbar^2}{2m_0}\nabla^2 + V(\mathbf{r})\right]\psi(\mathbf{r}) = E\psi(\mathbf{r}), \tag{2.2}$$

where m_0 is the electron rest mass and $\hbar$ the reduced Planck constant. According to the Bloch theorem, the wavefunctions have a form of Bloch waves,

$$\psi(\mathbf{r}) = e^{i\mathbf{k}\mathbf{r}}u_{n\mathbf{k}}(\mathbf{r}), \tag{2.3}$$

where $u_{n\mathbf{k}}$ is the periodic part of the Bloch wave, $u_{n\mathbf{k}}(\mathbf{r}) = u_{n\mathbf{k}}(\mathbf{r}+\mathbf{R}_m)$, n denotes the band and $\mathbf{k}$ fulfils the Born-von Karman periodic boundary conditions. By inserting 2.3 into 2.2, the following equation for $u_{n\mathbf{k}}$ is obtained:

$$\left[-\frac{\hbar^2}{2m_0}\nabla^2 + \frac{\hbar}{m_0}\mathbf{k}\cdot\mathbf{p} + \frac{\hbar^2k^2}{2m_0} + V(\mathbf{r})\right]u_{n\mathbf{k}}(\mathbf{r}) = E_n(\mathbf{k})u_{n\mathbf{k}}(\mathbf{r}). \tag{2.4}$$

The term **k·p**, which is absent at the Γ point, gives the origin of the name **k·p** theory. If the Γ point ($\mathbf{k}_0 = 0 \equiv \Gamma$) is chosen, and if it is assumed that the eigenenergies $E_n(\Gamma)$ and eigenfunctions $u_{n\Gamma}$ of the system are known in such point, the solution of 2.4 can be expanded as the series

$$u_{n\mathbf{k}} = \sum_m c_{nm\mathbf{k}}u_{m\Gamma}. \tag{2.5}$$

The expansion 2.5 can be now inserted into equation 2.4, multiplied by $u^*_{l\Gamma}$, and integrated over the unit cell volume. Using the orthogonality of the set $u_{m\Gamma}$ and the relation

$$\left[-\frac{\hbar^2}{2m_0}\nabla^2 + V(\mathbf{r})\right]u_{n\Gamma}(\mathbf{r}) = E_n(\Gamma)u_{n\Gamma}(\mathbf{r}), \tag{2.6}$$

the set of equations for the coefficients $c_{nm\mathbf{k}}$ is finally obtained:

$$\sum_m H_{lm}(\mathbf{k})c_{nm\mathbf{k}} = E_n(\mathbf{k})c_{nl\mathbf{k}}, \tag{2.7}$$

where the matrix elements of the Hamiltonian are

$$H_{lm}(\mathbf{k}) = \left[E_m(\Gamma) + \frac{\hbar^2}{2m_0}\right]\delta_{lm} + \frac{\hbar}{m_0}\mathbf{k}\cdot\langle u_{l\Gamma}|\,\mathbf{p}\,|u_{m\Gamma}\rangle\,. \tag{2.8}$$

The solution of the system 2.7 provides the exact band structure. However, to reduce

the calculation complexity it is possible to restrict the expansion 2.5 to a finite set of u-functions (for example VBs and CBs for the expansions) and include the distant bands perturbatively [51]. The above treatment applies to non degenerate bands and can be used to describe the CB. In case of more bands the coupling effects give important contribution and the description becomes more complicated.

The $\mathbf{k}\cdot\mathbf{p}$ theory provides a useful formula for the effective mass m^*. Consider the n-th band having maxima or minima at the Γ-point, the band energy is expanded near this point using a Taylor series up to the second order:

$$E_n(\mathbf{k}) = E_n(\Gamma) + \frac{\hbar^2}{2m_0} \sum_{i,j\in\{x,y,z\}} \left(\frac{1}{m^*}\right)_{ij} k_i k_j. \tag{2.9}$$

On the other hand, it is also possible to retrieve the energy $E_n(\mathbf{k})$ using $\mathbf{k}\cdot\mathbf{p}$ theory, when only one band is used for the expansion and the remaining bands are included as a perturbation. We obtain

$$E_n(\mathbf{k}) = E_n(\Gamma) + \frac{\hbar^2}{2m_0}\mathbf{k}^2 + \sum_{m\neq n} \frac{|H_{nm}|^2}{E_n(\Gamma) - E_m(\Gamma)}. \tag{2.10}$$

Comparing equations 2.9 and 2.10 and using 2.8 for the matrix elements of the Hamiltonian, the formula for the tensor of reciprocal effective mass is obtained:

$$\left(\frac{1}{m^*}\right)_{ij} = \delta_{ij} + \frac{2}{m_0} \sum_{m\neq n} \frac{Re[\hat{\mathbf{i}}p_{nm} \cdot \hat{\mathbf{j}}p_{mn}]}{E_n(\Gamma) - E_m(\Gamma)}, \tag{2.11}$$

where $\hat{\mathbf{i}}$, $\hat{\mathbf{j}}$ are unit vectors in a given direction and p_{ab} the momentum matrix elements.

2.3. Influence of stress on the GaAs band structure

In this section the effect of stress on the band structure of GaAs is discussed. First, a general introduction to the concepts of stress and strain is given, then the $\mathbf{k}\cdot\mathbf{p}$ method is used to describe the effects occurring in the band structure of bulk GaAs if anisotropic stress in the (001)-plane is applied, following the work of Chuang [50].

Strain, generally denoted as ε, is a normalised measure of deformation representing the displacement between particles in the body relative to a reference length. Figures 2.3(a) and 2.3(b) show the unit vectors of the atom A before ($\mathbf{r}$) and after ($\mathbf{r}'$) the crystal deformation, respectively. If ε describes the tensor for the strain state of the crystal, the relation between the unit vectors of the unstrained and the strained unit cell is given by:

$$\begin{aligned} \mathbf{x}' &= (1+\varepsilon_{xx})\hat{x} + \varepsilon_{xy}\hat{y} + \varepsilon_{xz}\hat{z}, \\ \mathbf{y}' &= \varepsilon_{yx}\hat{x} + (1+\varepsilon_{yy})\hat{y} + \varepsilon_{yz}\hat{z}, \\ \mathbf{z}' &= \varepsilon_{zx}\hat{x} + \varepsilon_{zy}\hat{y} + (1+\varepsilon_{zz})\hat{z}. \end{aligned} \tag{2.12}$$

For the case of in-plane strain originating from lattice-mismatched growth, $\varepsilon_{xx} = \varepsilon_{yy}$

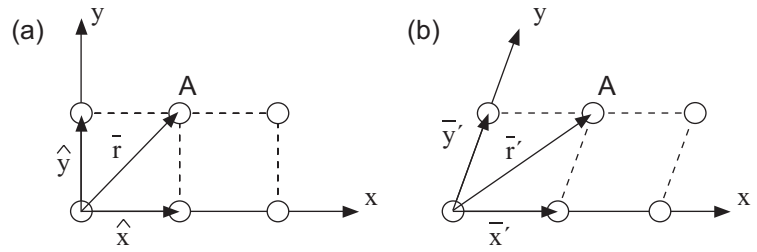

Figure 2.3.: Sketch of (a) an unstrained and (b) a strained lattice with position vector of atom A, respectively, $\mathbf{r}$ and $\mathbf{r}'$.

$= (a_0 - a)/a$, where a_0 and a are the lattice constants of the substrate and strained layer, respectively.

Stress (σ) is defined as force per unit area (1 N/m^2 = 1 Pa). Strain and stress are symmetric second-rank tensors (i.e., $\varepsilon_{ij} = \varepsilon_{ji}$ and $\sigma_{ij} = \sigma_{ji}$, where i, $j \in \{\mathrm{x,y,z}\}$). In the linear-elastic regime, the stress-strain relation is the generalised Hooke's law, which can be written in matrix form for the cubic crystal as:

$$\begin{pmatrix} \sigma_{xx} \\ \sigma_{yy} \\ \sigma_{zz} \\ \sigma_{xy} \\ \sigma_{yx} \\ \sigma_{zx} \end{pmatrix} = \begin{pmatrix} C_{11} & C_{12} & C_{12} & 0 & 0 & 0 \\ C_{12} & C_{11} & C_{12} & 0 & 0 & 0 \\ C_{12} & C_{12} & C_{11} & 0 & 0 & 0 \\ 0 & 0 & 0 & C_{44} & 0 & 0 \\ 0 & 0 & 0 & 0 & C_{44} & 0 \\ 0 & 0 & 0 & 0 & 0 & C_{44} \end{pmatrix} \begin{pmatrix} \varepsilon_{xx} \\ \varepsilon_{yy} \\ \varepsilon_{zz} \\ 2\varepsilon_{xy} \\ 2\varepsilon_{yx} \\ 2\varepsilon_{zx} \end{pmatrix}. \tag{2.13}$$

The 6×6 matrix on right-hand side of the equation 2.13 represents the elastic stiffness of the cubic crystal. When the stress components are known an inverse Hooke's law permits the strain components to be calculated in a similar tensor via the elastic compliance constants.

In contrast with the unstrained case, there are two reasons why the band structure of the strained crystal cannot be determined directly by perturbation theory [52]. First, even for an infinitesimally small strain, the strain-induced potential difference is not really small. If $V(\mathbf{r})$ and $V_0(\mathbf{r})$ are the potentials at the position vector $\mathbf{r}$ in strained and unstrained crystal systems, then for a sufficiently large $\mathbf{r}$ the potential difference $V(\mathbf{r}) - V_0(\mathbf{r})$ can be the order of $V_0(\mathbf{r})$. The second, stress changes the interatomic distances, as can be seen in Fig. 2.3, and thus also the periodicity of the wavefunctions $u_{nk}(\mathbf{r})$. This leads to a shift of the band-edge energy, a change of the effective mass, and can also lead to mixing of different bands.

G. E. Pikus and G. L. Bir showed how to calculate strain effects on the band structure using deformation potentials. They introduced a coordinate transformation in such a way that both an undeformed and a deformed crystal can have the same boundary conditions. In this way, they brought the strain effect into the scope of the perturbation theory. The details of the transformation can be found in Refs. [50, 52, 53]. While the effect of strain on the CB is mostly limited to a shift proportional to the volumetric strain, $\varepsilon_{vol} = \mathrm{tr}(\varepsilon)$, the effects on the VBs are richer, because application of a non-purely-hydrostatic stress leads to symmetry breaking and thus to lifting of degeneracy.

The energy values are obtained by solving the Schrödinger equation, taking into account the periodicity of the lattice by using the Bloch wavefunctions (see section 2.2). In particular, the dispersion relation of the CB for the strained GaAs is given by:

$$E(k) = E_g + \frac{\hbar^2}{2m_e^*}(k_x^2 + k_y^2 + k_z^2) + a_c(\varepsilon_{xx} + \varepsilon_{yy} + \varepsilon_{zz}), \tag{2.14}$$

where a_c is the hydrostatic deformation potential.
The effects on the VBs can be described by the so-called 6×6 Pikus-Bir Hamiltonian (H^{PB}), which takes into account the linear strain [53]:

$$H_{jj'} = H_{jj'}^{LK} + (H_\varepsilon^{PB})_{jj'} = E_j(0)\delta_{jj'} + \sum_{\alpha,\beta} \hat{D}_{jj'}^{\alpha\beta} k_\alpha k_\beta + \sum_{\alpha,\beta} \hat{D}_{jj'}^{\alpha\beta} \varepsilon_{\alpha\beta}, \tag{2.15}$$

where the first two terms belong to the Luttinger-Kohn Hamiltonian (**k**·**p** method with multiple bands).
For most III-V semiconductors the spin-orbit split-off bands can be ignored. In fact, they are several hundred meV below the HH-LH degenerate bands whereas the energy change due to strain lies in the range of only several tens of meV. The 4×4 Hamiltonian given in the basis $|J, J_z\rangle$ of HH and LH ($|\frac{3}{2}, \frac{3}{2}\rangle$, $|\frac{3}{2}, \frac{1}{2}\rangle$, $|\frac{3}{2}, -\frac{1}{2}\rangle$, $|\frac{3}{2}, -\frac{3}{2}\rangle$), consists of two parts and reads as follows:

$$H = H^{LK} + H_\varepsilon^{PB} = -\begin{pmatrix} P+Q & -S & R & 0 \\ -S^+ & P-Q & 0 & R \\ R^+ & 0 & P-Q & S \\ 0 & R^+ & S^+ & P+Q \end{pmatrix}, \tag{2.16}$$

where the superscript "+" stands for Hermitian conjugate and the following notation is used:

$$\begin{aligned} P &= P_k + P_\varepsilon, \quad Q = Q_k + Q_\varepsilon, \\ R &= R_k + R_\varepsilon, \quad S = S_k + S_\varepsilon, \end{aligned} \tag{2.17}$$

with

$$\begin{aligned} P_k &= \frac{\hbar^2\gamma_1}{2m_0}(k_x^2 + k_y^2 + k_z^2), \;\; Q_k = \frac{\hbar^2\gamma_2}{2m_0}(k_x^2 + k_y^2 - 2k_z^2), \\ R_k &= \frac{\hbar^2}{2m_0}[-\sqrt{2}\gamma_2(k_x^2 - k_y^2) + i2\sqrt{3}\gamma_3 k_x k_y], \;\; S_k = \frac{\hbar^2\gamma_3}{m_0}\sqrt{3}(k_x - ik_y)k_z, \\ P_\varepsilon &= a_v(\varepsilon_{xx} + \varepsilon_{yy} + \varepsilon_{zz}), \;\; Q_\varepsilon = -\frac{b}{2}(\varepsilon_{xx} + \varepsilon_{yy} - 2\varepsilon_{zz}), \\ R_\varepsilon &= \frac{\sqrt{3}b}{2}(\varepsilon_{xx} - \varepsilon_{yy}) - id\varepsilon_{zz}, \;\; S_\varepsilon = -d(\varepsilon_{xz} - i\varepsilon_{yz}), \end{aligned}$$

where a_v is the hydrostatic deformation potential, and b and d the shear deformation potentials. The constants γ_1, γ_2 and γ_3 are the Luttinger parameters, specific for every

material, giving rise to the bending of the corresponding band. They are related to a_v, b and d via the correspondence $k_i k_j \leftrightarrow \varepsilon_{ij}$:

$$\begin{aligned}\frac{\hbar^2\gamma_1}{2m_0} &\leftrightarrow -a_v \\ \frac{\hbar^2\gamma_2}{2m_0} &\leftrightarrow -\frac{b}{2} \\ \frac{\hbar^2\gamma_3}{2m_0} &\leftrightarrow -\frac{d}{2\sqrt{3}}.\end{aligned}$$

Since optical measurements involving the lowest direct bandgap region, e.g., at Γ point ($\mathbf{k} = 0$) in GaAs, are mainly investigated in this work, the kinetic part of the matrix 2.16 is zero and the total Hamiltonian of the VBs can be reduced to the following diagonal matrix, only in the case of isotropic biaxial strain applied in the (001) plane:

$$H_\varepsilon^{PB} = -\begin{pmatrix} P_\varepsilon + Q_\varepsilon & 0 & 0 & 0 \\ 0 & P_\varepsilon - Q_\varepsilon & 0 & 0 \\ 0 & 0 & P_\varepsilon - Q_\varepsilon & 0 \\ 0 & 0 & 0 & P_\varepsilon + Q_\varepsilon \end{pmatrix}. \tag{2.20}$$

In fact, the Hamiltonian matrix shown in 2.20 has $R_\varepsilon = S_\varepsilon = 0$ when $\varepsilon_{xx} = \varepsilon_{yy} \neq \varepsilon_{zz}$ and $\varepsilon_{xy} = \varepsilon_{yz} = \varepsilon_{zx} = 0$. In the case of anisotropic strains the H^{PB} is not diagonal anymore, since R_ε, $R_\varepsilon^+ \neq 0$ and HH and LH are mixed. The effect of isotropic biaxial strain on the corresponding band-edge energy is shown in Fig. 2.4.

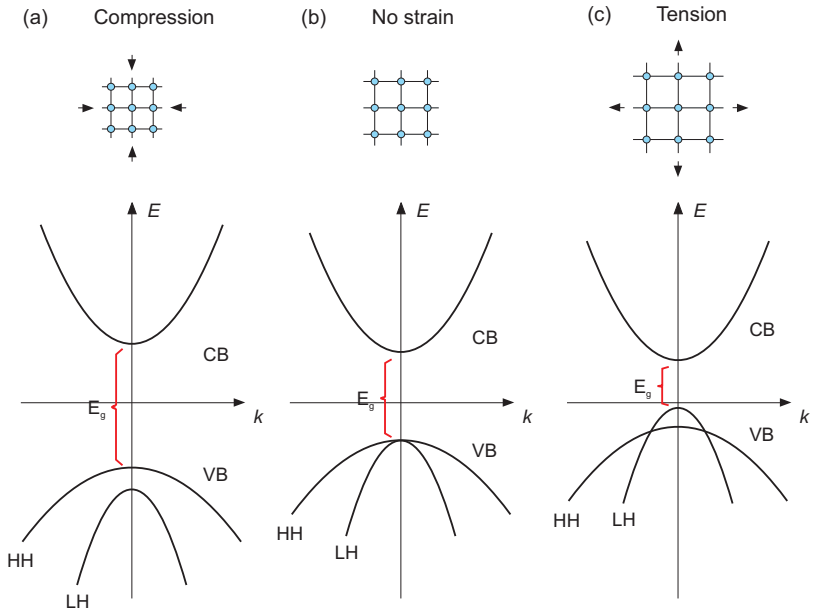

Figure 2.4.: The energy-band structure in the momentum space for a bulk GaAs material under (a) isotropic biaxial compression, (b) no strain, and (c) isotropic biaxial tension. The top sketches illustrate the in-plane deformation of the lattice. The k vector in the central panel is parallel to the z direction.

When no strain is induced in the crystal, the HH and LH bands are degenerate. Under compression the HH band is above the LH band whereas the LH band shifts above the HH band in the case of tension. Strain affects also the effective masses but the effect is not shown here for a sake of simplicity.
The HH and LH bands are separated by $2Q_\varepsilon$. The net energy transitions for the CB to VBs are:

$$E_{\text{C-HH}}(\mathbf{k}=0) = E_g + (a_c - a_v)(\varepsilon_{xx} + \varepsilon_{yy} + \varepsilon_{zz}) - \frac{b}{2}(\varepsilon_{xx} + \varepsilon_{yy} - 2\varepsilon_{zz})$$
$$E_{\text{C-LH}}(\mathbf{k}=0) = E_g + (a_c - a_v)(\varepsilon_{xx} + \varepsilon_{yy} + \varepsilon_{zz}) + \frac{b}{2}(\varepsilon_{xx} + \varepsilon_{yy} - 2\varepsilon_{zz})$$

2.4. Semiconductor quantum dots

The section describes how the reduction of the dimensions of materials affects the quantum confinement and energy of carriers in semiconductor QDs. Then, the specific interactions energies of the QD species, which influence the emission spectrum, and the fine structure splitting, which originates from the electron-hole exchange interaction, are introduced. As a conclusion, a review of the state of the art of the field will be given.

2.4.1. Effect of confinement

Semiconductor QDs can be created as nanometre sized crystals of a semiconductor material embedded in another material with a larger bandgap E_g [54].
These heterostructures form a potential well where carriers are confined in all three directions. Since the dimensions of a QD are comparable to the de Broglie wavelength (λ_b) of trapped carriers, then the motion in these directions is quantised. λ_b of electrons or holes in a semiconductor is given by

$$\lambda_b \sim \frac{h}{\sqrt{m^* k_B T}}, \tag{2.22}$$

where h and k_B are Planck's and Boltzmann's constants, m^* is the carrier effective mass, and T is the temperature. For an electron in the conduction band of GaAs with $m^*/m^0 = 0.063$ [55], $\lambda_b \sim$40 nm at room temperatures, which is close to the typical size of a self-assembled semiconductor QD (see section 3.1.1). Due to a process known as "thermal escape" of carriers from the material [56], activated by carrier-phonon interactions [57], the quantum effects are visible only at cryogenics temperatures, where λ_b increases. For materials with large band discontinuity, such as nanocrystals surrounded by vacuum/air, quantisation effects persist up to room temperature and above.

The general classification of quantum-confined structures is illustrated schematically in Fig. 2.5. The density of states (DOS), i.e., the number of states per energy interval, and the energy spectrum change significantly with the dimensionality of the confinement potential [58], resulting in an increase of the effective bandgap energy. For bulk material, i.e., the non confined case, the DOS is approximately proportional

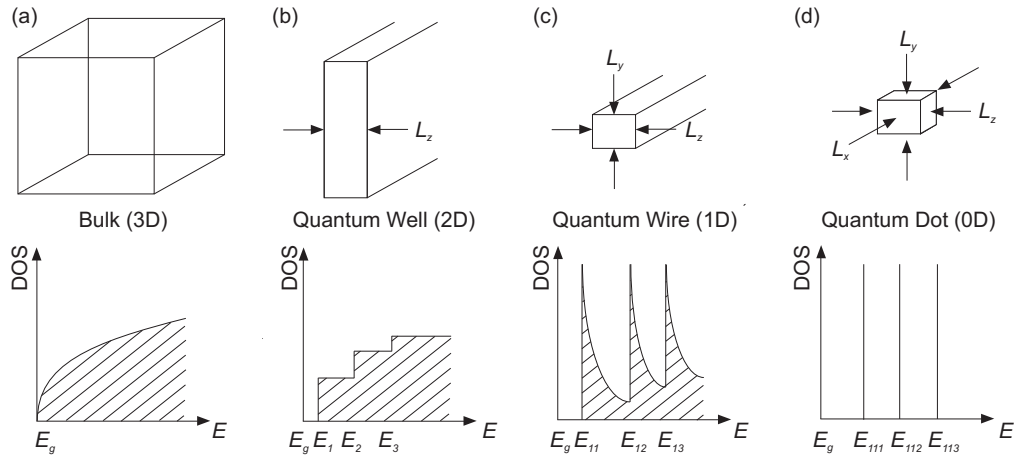

Figure 2.5.: Sketches (upper row) and density of states (DOS) as a function of carriers energy (lower row) for heterostructures of different dimensionalities.

to $(E - E_g)^{1/2}$ for energies above E_g and vanishes for energies below the bandgap [59] [see Fig. 2.5(a)]. For particles confined in a quantum well (QW), i.e., a two-dimensional system with quantum confinement in one direction, the DOS shows a staircase pattern [see Fig. 2.5(b)]. The confinement in a quantum wire (2D confinement) leads to $E^{-1/2}$ dependence with peaks of the DOS for each new quantised state, as shown in Fig. 2.5(c). The only structure for which the particles have discrete energy states is the QD (3D confinement) and the DOS consists of a series of Dirac-δ functions at each quantised level [see Fig. 2.5(d)]. The discrete states of electrons and holes lead to a discrete energy spectrum for the photons emitted when electrons and holes recombine (see section 2.4.2). This is the reason why QDs are considered as "artificial atoms".

In analogy with the quantum mechanical problem of the "particle in a box", the electron wavefunction Ψ can be defined as a product of a periodic part, the Bloch function $u(\mathbf{r})$, and an envelope wavefunction $F_{\mathbf{k}}(\mathbf{r})$ [60]:

$$\Psi = F_{\mathbf{k}}(\mathbf{r})u(\mathbf{r}). \tag{2.23}$$

The equation of motion is given by the Schrödinger equation in "the effective-mass approximation",

$$\left(-\frac{\hbar^2}{2m^*} \bigtriangledown^2 + V(\mathbf{r})\right) F_{\mathbf{k}}(\mathbf{r}) = E(\mathbf{k})F_{\mathbf{k}}(\mathbf{r}), \tag{2.24}$$

and the potential $V(\mathbf{r}) = V(x) + V(y) + V(z)$ corresponds to the energy of the appropriate band edge. m^* is usually calculated using the $\mathbf{k}\cdot\mathbf{p}$ perturbation theory (see section 2.2). In GaAs and InAs, $u(\mathbf{r})$ is a s-like wavefunction for electrons in the CB, and is a p-like wavefunction for holes in the VB.
By solving the equation 2.24 for a QD of volume $L_xL_yL_z$ and an infinite confinement potential for all the directions, we obtain the discrete energy levels

$$E(\mathbf{k}) = E_{n_x} + E_{n_y} + E_{n_z} = \frac{\hbar^2}{2m^*}\left[\left(\frac{n_x\pi}{L_x}\right)^2 + \left(\frac{n_y\pi}{L_y}\right)^2 + \left(\frac{n_z\pi}{L_z}\right)^2\right], \tag{2.25}$$

with corresponding standing wave patterns

$$F_{\mathbf{k}} = \frac{1}{\sqrt{L_x L_y L_z}} \phi_{n_x}(x)\phi_{n_y}(y)\phi_{n_z}(z), \tag{2.26}$$

where n_x, n_y, n_z are integers and $\mathbf{k} = (\frac{n_x\pi}{L_x}, \frac{n_y\pi}{L_y}, \frac{n_z\pi}{L_z})$.
Finally, the DOS is given by:

$$g(E) = 2N_d \sum_{n_x,n_y,n_z} \delta(E - E_{n_x} - E_{n_y} - E_{n_z}), \tag{2.27}$$

where N_d is the volume density of QDs and the factor 2 accounts for spin degeneracy.

2.4.2. Quantum dot states and fine structure splitting

Two types of QDs are generally distinguished depending on the band alignment: the QDs of type I, where both particles are localised in the same layer of semiconductor, this means both type of carriers are trapped. The type-II system has localisation in different layers with the result that only one type of carrier is trapped [61, 62].
Since optically active nanostructures are more desirable for the purposes of this work, type-I QDs were investigated. They are grown by MBE (see section 3.1) with a smaller bandgap material than the bulk material in which they are embedded, e.g., InAs in GaAs or GaAs in AlGaAs. The carriers are created through photo-excitation in the bulk material promoting electrons from the VB into the CB and leaving holes in the VB. Through non-radiative processes, electrons and holes relax to the lowest energy position in the QD region, in the CB and VB respectively [63]. The bound electron and hole pair produced is called *exciton* and the recombination leads to a single photon emission with a time scale of hundreds of picoseconds. This process is called photoluminescence (PL). The total exciton energy is the combination of the bandgap energy, the confinement energy of electron and hole and the Coulombic potential energy.
Several parameters influence the QD emission spectra such as the size of the QD, the shape of the confining potential barrier [46], the effective mass of the carriers, the composition profile of the materials [64], the built-in strain fields [65] and the defects in the QD surrounding [66].

The Pauli exclusion principle reduces the possible charge configurations in a QD, since each energy level can accommodate only two carriers with opposite spins. Figure 2.6 shows different excitonic configurations starting from the ones that are created first (at low temperature the lowest energy levels are occupied first).
The neutral exciton (X or X^0) can have the following total angular momentum projection along the quantisation axis $M = S_z + J_z = +2, -2, +1, -1$. Excitons with $M = \pm 2$ are called dark excitons (X_d) since the decay to the ground state (vacuum) via the emission of a single photon is forbidden, due to the total angular momentum conservation (the photon carries $S = 1$). Contrarily, $M = \pm 1$ describes bright excitons (X_b) that can decay to the vacuum state through emission of a single photon.
When the QD traps an additional electron or hole, the trions X^- or X^+ are formed, usually referred as negatively or positively charged excitons, respectively. They can

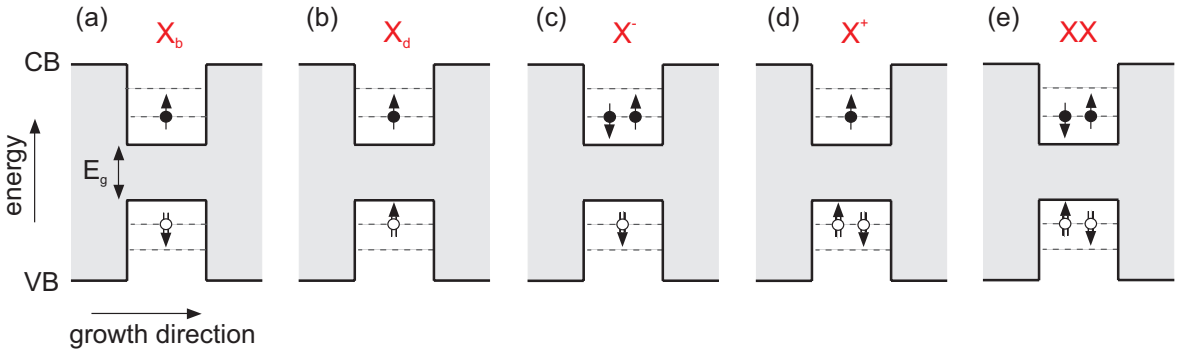

Figure 2.6.: Schematic representation of a type-I QD in different lowest energy states: (a) the bright exciton X_b, (b) the dark exciton X_d, (c) the negatively charged exciton X^-, (d) the positively charged exciton X^+, and (e) the biexciton XX. Single and double arrows indicate the directions of the electron's spin S and the hole's total angular momentum J, respectively.

have two different spin states, either electron or hole spin up or down. Another important state is the biexciton (XX), consisting of two electron-hole pairs with zero total spin and angular momentum, respectively, because of Pauli's exclusion principle. It can decay via emission of a single photon to either one of the bright X states (see Fig. 2.8).

The emission from a single QD consists of a number of lines spectrally separated, corresponding each to a different excitonic state decay, as shown in Fig. 2.7 for an InGaAs/GaAs QD.

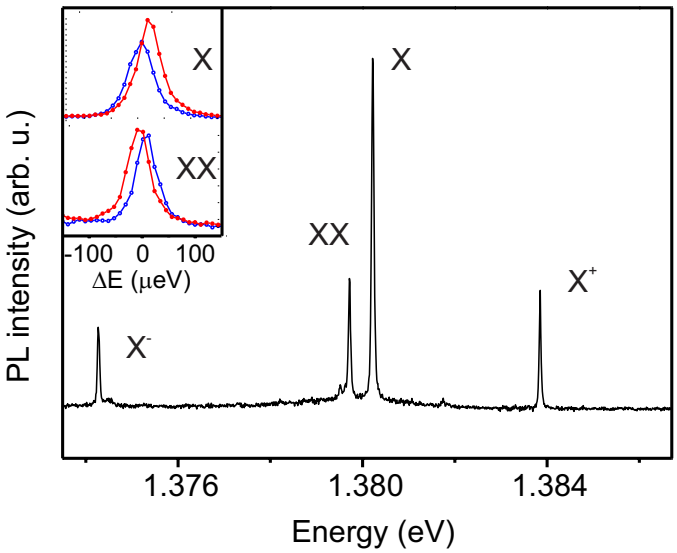

Figure 2.7.: Typical photoluminescence (PL) emission spectrum of a single InGaAs/GaAs QD with neutral exciton (X), biexciton (XX), negatively (X^-) and positively (X^+) charged excitons. The inset shows an expanded view of the orthogonally polarised X and XX states.

The energy of the photons emitted after the recombination is determined by the complex Coulomb and exchange interactions between the carriers in the initial and final excitonic states [63]. The direct Coulomb interaction is defined as:

$$C_{ij} = \frac{q_i q_j}{4\pi\epsilon_0} \int\int \frac{|\psi_i(\mathbf{r_1})|^2 |\psi_j(\mathbf{r_2})|^2}{\epsilon(\mathbf{r_1}-\mathbf{r_2})|\mathbf{r_1}-\mathbf{r_2}|} d\mathbf{r_1} d\mathbf{r_2}, \tag{2.28}$$

where i, j represent electron or hole, q is the elementary charge, ϵ_0 is the permittivity in the free space, ϵ is the screened dielectric function, $|\psi|^2$ and $\mathbf{r}$ are the density probability and the coordinate of the carrier, respectively. As a result, C_{ee} and C_{hh} are repulsive whereas C_{eh} is attractive. The total emission energies of the excitonic species can be estimated following the work of Schliwa *et al.* [6]:

$$\begin{aligned}
E(X) &= E_e - E_h + C_{eh} + \delta_{corr}(X) + \delta_{exc}(X), \\
E(X^-) &= 2E_e - E_h + 2C_{eh} + C_{ee} + \delta_{corr}(X^-) + \delta_{exc}(X^-), \\
E(X^+) &= E_e - 2E_h + 2C_{eh} + C_{hh} + \delta_{corr}(X^+) + \delta_{exc}(X^+), \\
E(XX) &= 2E_e - 2E_h + 4C_{eh} + C_{ee} + C_{hh} + \delta_{corr}(XX) + \delta_{exc}(XX),
\end{aligned} \tag{2.29}$$

where $E_{e,h}$ is the confinement energy of the single particle, δ_{exc} describes corrections due to exchange interaction, δ_{corr} is the energy correction due to self-consistency and correlation effects. The latter is a many particle contribution originating from the finite probability of the particle to populate higher energetic states in the band structure, leading to a change of the emission energy [67].
More importantly, the excitonic energies measured in the experiment correspond to energy differences or binding energies (E_B), defined as:

$$\begin{aligned}
E_B(X) &= E_e + E_h - E(X) = \\
&\quad - C_{eh} - \delta_{corr}(X) - \delta_{exc}(X), \\
E_B(X^-) &= E(X) - E(X^-) + E_e = \\
&\quad - C_{eh} - C_{ee} + \delta_{corr}(X) - \delta_{corr}(X^-) + \delta_{exc}(X) - \delta_{exc}(X^-), \\
E_B(X^+) &= E(X) - E(X^+) - E_h = \\
&\quad - C_{eh} - C_{hh} + \delta_{corr}(X) - \delta_{corr}(X^+) + \delta_{exc}(X) - \delta_{exc}(X^+), \\
E_B(XX) &= E(X) - E(XX) + E(X) = \\
&\quad - 2C_{eh} - C_{ee} - C_{hh} + 2\delta_{corr}(X) - \delta_{corr}(XX) + 2\delta_{exc}(X) - \delta_{exc}(XX).
\end{aligned} \tag{2.30}$$

Since in InGaAs/GaAs QDs, the hole wavefunction is much more localised than the electron wavefunction (due to the larger effective mass) and the centres of mass of the two carriers are close, if correlation and exchange effects can be neglected the following relation holds:

$$C_{ee} < |C_{eh}| < C_{hh}. \tag{2.31}$$

This implies that the negative (positive) trion is always at the low- (high-) energy side of the X in these kind of QDs, as observed in Fig. 2.7. For a more precise estimate, correlation and exchange interactions have to be considered.

The electron-hole exchange interaction (J_{eh}) is a purely quantum mechanical effect, due to the spatial overlapping of two or more identical particles and it is responsible for the exciton FSS measured in structures with symmetry lower than D_{2d}[2].
The states X_b and X_d having the total angular momentum M = ±1, ±2, respectively, have been already introduced. They are four-fold degenerate in the case of negligible interactions between the spin of the electron S_z and total angular momentum of the hole J_z, as shown in the decay of the XX to the ground state in Fig. 2.8(a).
If the QD has circular symmetry and there are no anisotropic external fields, the effect of the electron-hole exchange is the splitting of the bright and dark doublets and the lifting of the degeneracy of the X_d. The dark doublet is at lower energy since S_z and J_z are parallel. In a more realistic picture asymmetries give rise to anisotropic exchange interactions between the carriers in the dot. They are caused by several mechanisms such as elongation of QDs along one of the in-plane crystal axes (e.g., [1-10] for InGaAs/GaAs QDs or [110] for GaAs/AlGaAs QDs), intrinsic strain field of the dot which remains after the QD formation (see section 3.1.1), alloy fluctuations or ordering or crystal inversion asymmetry [68]. In addition, there is a contribution from the piezoelectricity of the InAs and GaAs bulk materials usually leading to a small inbuilt electric field [69]. As a result, X_b is split into two non-degenerate states and the magnitude of the splitting is the FSS, denoted by s in Fig. 2.8.

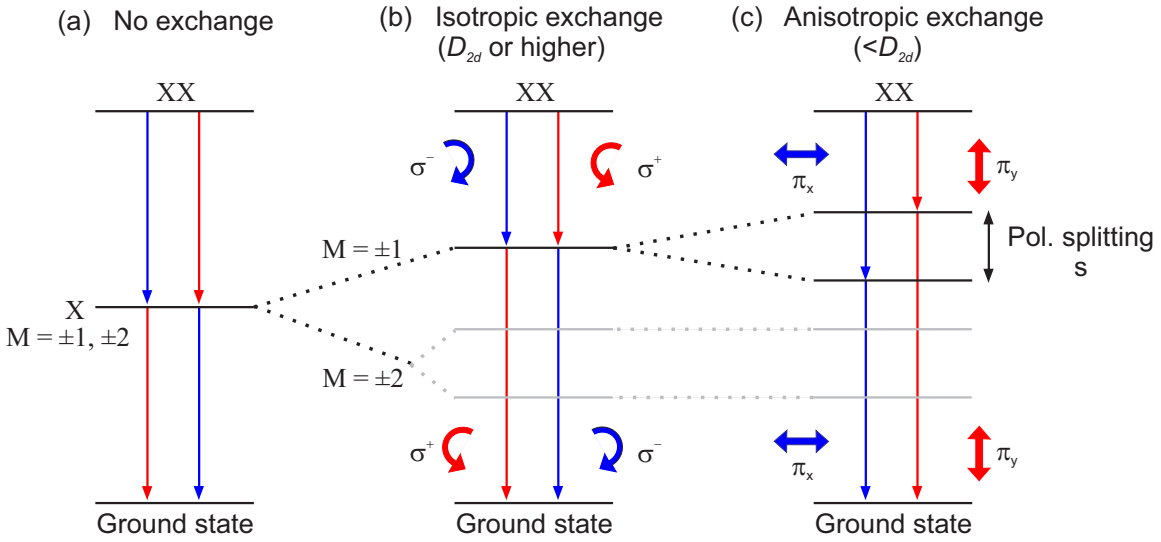

Figure 2.8.: Scheme of the radiative decay of the XX to the ground state in a QD (a) without exchange interaction, (b) in the case of D_{2d} or higher symmetry and isotropic exchange interaction, and (c) if the anisotropic exchange interaction is included (symmetry lower than D_{2d}).

The spin Hamiltonian describing the spin-spin coupling of the electron and hole forming the exciton X, obtained from symmetry considerations of the bulk structure,

[2]The group D_{2d} is characterised by two-fold rotational symmetry for three different axes (perpendicular to each other), symmetry under reflection at two planes (perpendicular to each other), invariant under a combination of a reflection and a 90° rotation around an axis perpendicular to the reflection plane.

is given by [48, 70]:

$$H_{exc} = -\sum_{i=x,y,z} (a_i J_i S_i + b_i J_i^3 S_i), \tag{2.32}$$

where the projections of the spins on the i-axis for hole and electron are J_i and S_i, respectively, and a_i and b_i are the spin-spin coupling constants, with $i = x, y, z$. The energy arising from the exchange interaction of an excitonic wavefunction Ψ_X is given by the integral shown in the work of Bayer *et al.* [46]:

$$E_{exc} \propto \int\int d^3r_1 d^3r_2 \Psi_X^*(\mathbf{r}_e = \mathbf{r}_1, \mathbf{r}_h = \mathbf{r}_2) \frac{1}{|\mathbf{r}_1 - \mathbf{r}_2|} \Psi_X(\mathbf{r}_e = \mathbf{r}_2, \mathbf{r}_h = \mathbf{r}_1), \tag{2.33}$$

where $\mathbf{r}_{e,h}$ are the electron or hole coordinates.
The electron-hole exchange can be separated into two parts: a short-range interaction, arising from the crystal symmetry, which mainly splits the X_b and X_d but contributes also to the FSS in QDs with symmetry lower than D_{2d}, and a long-range interaction originating from the macroscopic anisotropy of the QD, which contributes to the splitting of the X_b and X_d and to the FSS but does not split the X_d.

The FSS-concept is very important for applications in quantum communication technology (see section 2.4.3). In the past years, several proposal have been studied for the creation of sources of entangled photon pairs. For example, Benson *et al.* [14] proposed the use of the radiative decay of the XX to the X to the crystal ground state via the emission of a XX photon and an X photon (see Fig. 2.8). For dots with zero FSS, the photon pairs emitted via the radiative decay of XX to the ground state are cross-circularly (σ_- and σ_+) polarised pairs and are entangled. In particular, the emission of a right-circularly-polarised biexciton photon (R_{XX}) followed by a left-circularly-polarised exciton photon (L_X) has equal probability of the emission of a L_{XX} photon followed by a R_X photon. The photon-pair results entangled in polarisation and predicted to be in the maximally entangled Bell state:

$$\psi = \frac{1}{\sqrt{2}}(|R_{XX}L_X\rangle + |L_{XX}R_X\rangle). \tag{2.34}$$

Typical dots show FSS and the emission becomes linearly polarised (horizontally, π_x, or vertically, π_y) with distinct polarisations parallel to the [110] and [1-10] axes of the crystal [71] (blue and red lines, respectively, in the inset of Fig. 2.7) or to the elongation directions of the QD potential. In fact, the XX ground state has total spin projection 0 and it consists of a single non-degenerate state. The decay of the XX to either one of the X_b states with total spin projection ± 1 leads to a photon differing in energy with respect to the subsequently emitted photon as the X decays to the ground state. This is the reason why the XX line also exhibits a splitting, in an equal and opposite sense to the X line, as shown in the inset of Fig. 2.7.

Charged excitons in single QDs, differently to neutral excitons, don't show FSS. For example, the ground state of X^- consists of two electrons with opposite spin and a hole having two possible spin orientations. Practically, the hole interacts with a spin singlet electron pair, where the two electron wavefunctions have about the same spatial distributions. If the strong confinement regime for the QD is assumed, the

contribution from the higher energy orbitals can be neglected and the exchange energy splitting should vanish. After the recombination the final state consists of a single electron that cannot show splitting. The same arguments are valid for the X^+. In the case of QDs coupled together, trions can show more complex behaviours, as reported in section 4.4.4.

2.4.3. State of the art

A multitude of tuning techniques has been investigated by many groups across the world for tailoring the optical properties of QDs. Among the non-reversible ones, change of the growth parameters [72] or annealing treatments after growth, such as rapid thermal annealing [73], can blueshift the InAs/GaAs QD emission energy up to 300 meV, due to In-Ga intermixing. This technique can also be applied to GaAs/AlGaAs QDs [74]. However, annealing based methods are unidirectional and not precise. Reversible and fine tuning of the QD emission energies to longer wavelength can be obtained via the application of cryogenic temperature [75], which decreases the bandgap of the QD material, and by the application of an external magnetic field [46], due to the diamagnetic shift.

Apart from the high temperature tuning, which broadens the emission linewidths together with a drop of the intensity, all the above mentioned techniques are characterised by narrow tuning ranges (of the order of meV), much smaller than the typical natural emission range of the QD ensemble (tens of meV). A large tuning range is desirable in order to tune the QD emission energy in resonance to a photonic crystal cavity [9], or in resonance to an atomic vapour system [23], or for the realisation of entangled photon pair sources [21, 22]. The last two topics will be investigated in sections 4.1 and 4.2, respectively.

In order to produce entangled photon pairs via the XX-X cascade, large fields are needed for erasing the FSS and recovering a QD symmetry D_{2d} or higher (see section 2.4.2). Control of FSS has been demonstrated by several studies dealing with post-growth tuning of the FSS using annealing [64], application of external lateral and vertical magnetic [22], lateral electric [76] fields or uniaxial stress [77], and interaction with laser fields via the optical Stark effect [78]. The latter is an elegant and flexible technique to tune the FSS, at the expense of a comparably small tuning range of only 20 μeV. Magnetic fields have a large tuning range of up to more than 100 μeV but require a bulky setup. On the other hand, the electric field in conventional QD structures separates electrons and holes in the QD, leading to a decrease of the emission intensity [79].

Recently, Bennett *et al.* developed a device that is able to avoid this problem [80] (see also section 4.2). By embedding the InAs/GaAs QDs in a GaAs/AlGaAs QW, the escape of the carriers from the dot region is reduced and it is possible to apply large vertical electric fields along the growth direction, which extend the tunability up to 25 meV, as shown in Fig. 2.9(a). An experimental proof of the anticrossing between the bright excitonic states for three different QDs is shown in Fig. 2.9(b).
The FSS changes as the relative electric field $F - F_0$ is varied, where F_0 is the value of the electric field for which the FSS reaches its minimum magnitude, s_0. Away from

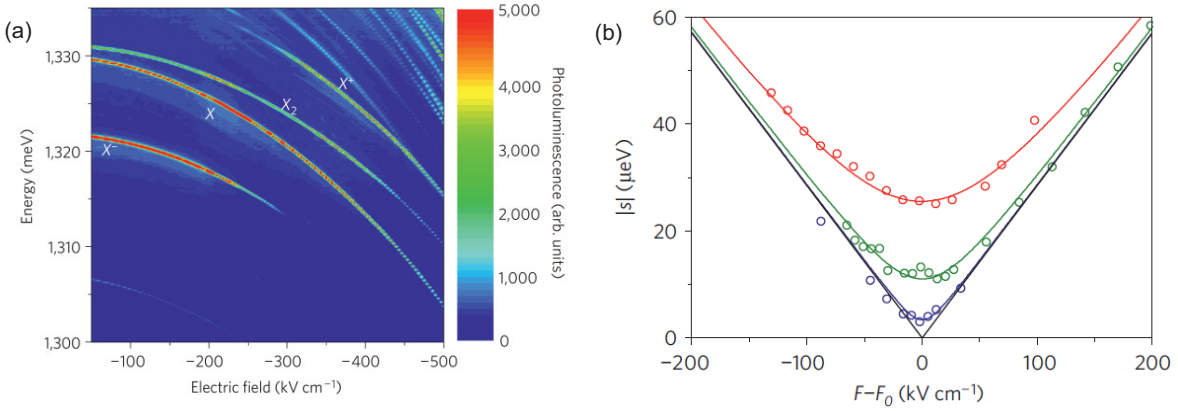

Figure 2.9.: (a) Typical plot of PL energy as a function of the electric field for a single InGaAs/GaAs QD. (b) FSS of three QDs as a function of the relative electric field $(F - F_0)$, where F_0 is the field at which the minimum of FSS (s_0) is reached for each QD. Figure from Ref. [80].

the minimum (FSS $\gg s_0$) they measure a linear change in the magnitude of FSS with electric field $F - F_0$. The quantum confined Stark effect (QCSE), which occurs when an electric field is applied to a QD [76, 81], can explain this behaviour. The energy of the exciton is well described by the formula:

$$E = E_0 - pF + \beta F^2, \tag{2.35}$$

where E_0 is the energy of the exciton at $F = 0$ kV/cm, p is the permanent dipole in the z direction and β stands for its polarisability. In particular, p takes into account the distance between the centre of masses of the electron and hole wavefunctions [81]. At large values of FSS the two bright exciton states can be thought as radiating electric dipoles being aligned along the [110]/[1-10] directions of the crystal. This means that the light emitted by the exciton recombination is linearly polarised. Due to different values of the dipole moments p_H and p_V [82], the FSS has a linear change:

$$\text{FSS} = (p_H - p_V)F, \tag{2.36}$$

where it was assumed that β does not depend on the in-plane anisotropy of the QD [82]. The fact that in the limit FSS $\gg s_0$ all QDs show a similar relative change of the FSS as F is varied indicates that all QDs have similar in-plane anisotropy. Interestingly, the polarisation angle with respect to the crystal axes [110]/[1-10] shows faster rotation the smaller the minimum value of the FSS is (not shown).
In spite of the anticrossing of the bright exciton states, this tuning technique can also be used to decrease the FSS to values small enough for the creation of entangled photon pairs [80]. This can be obtained by cherry picking the QD with a minimum splitting below the value required in the proposals from Benson *et al.* [14].

Unfortunately, the use of electric fields to tune the FSS requires optical excitation hindering the possibility to charge the QD electrically [83], which is crucial for on-chip integration of the devices. A "tuning knob" overcoming these issues could be strain

(see section 2.3).
It has been known for many years that strain can be used to manipulate the electronic properties in semiconductors [84]. However, only in 2006 Seidl *et al.* showed the effect of uniaxial stress on excitons in QDs [77]. In order to control the deformation, they glued a sample containing InGaAs/GaAs QDs onto a piezoelectric lead zirconate titanate (PZT) stack actuator. The voltage applied to the PZT expands/contracts uniaxially the sample and the two excitonic emission lines of the QD can be shifted through the QCSE, as shown in Fig. 2.10(a).

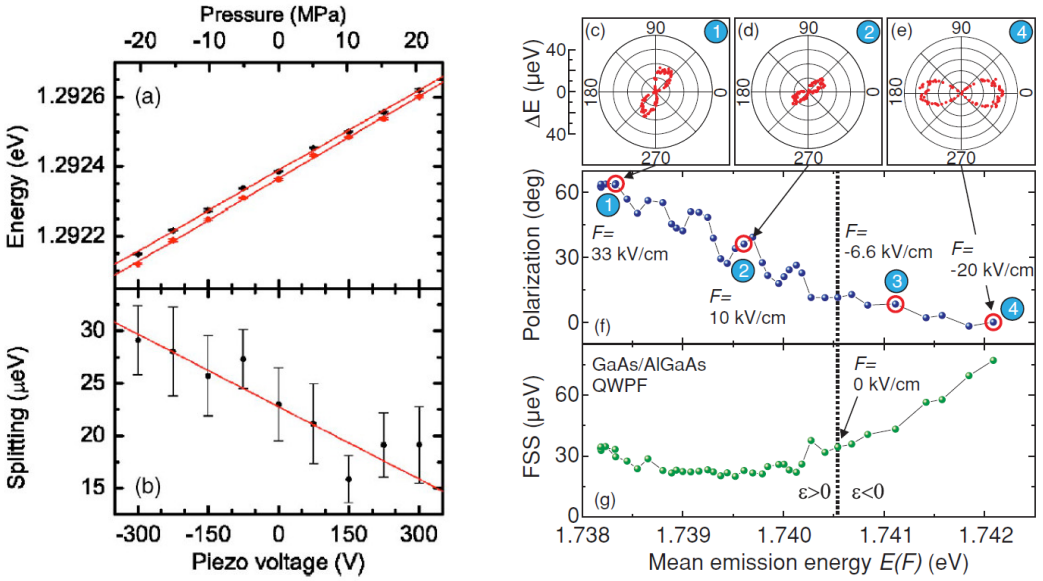

Figure 2.10.: Piezovoltage dependence of (a) the two X^0 resonances and (b) the splitting between the two resonances in InGaAs/GaAs QDs. In both (a) and (b) the solid lines are linear fits to the measured data points. (c)-(e) Polarisation dependence in polar coordinates of the relative emission energy (ΔE) in GaAs/AlGaAs QDs for three values of the field applied to the piezo (F), reported in (f) (the mean emission energy, $E(F)$, for each value of F is subtracted). (f) Polarisation orientation of the high-energy component with respect to x, parallel to F and $\varepsilon_{//}$, as a function of $E(F)$. (g) FSS as a function of $E(F)$. Figures (a-b) from Ref. [77] and (c-g) from Ref. [86].

The QD emission energy increases (decreases) as a function of increasing (decreasing) piezostack voltage up to ∼0.5 meV in the whole range, due to the change in the bandgap of the QD material under the effect of compressive (tensile) strain. The strain transferred to the QD was smaller than 0.05% and it was quantified by measuring the shift of the free exciton transitions of the GaAs host material. The behaviour of the FSS as a function of the piezo voltage/pressure is shown in Fig. 2.10(b), where a maximum total change in FSS of ∼10 μeV was observed.

In late 2009, Zander *et al.* [85] were able to transfer relatively large biaxial stresses by gluing (via a thermoplastic PMMA) micro-(μ-)ring resonators containing InGaAs/GaAs QDs onto a relaxor ferroelectric material (lead magnesium niobate-lead titanate, PMN-PT, see section 3.3 for more details). The tuning of various emission lines from a single

μ-ring showed a maximum energy tuning for the QDs of $\sim$3.8 meV. It was also observed that the strain transfer to the QDs can be improved by immersing the μ-rings in PMMA or by using a stiffer material than PMMA, as will be demonstrated in sections 4.1 and 4.2.

Recently, Plumhof *et al.* [86] showed that the polarisation direction of the X^0-states of the QDs can be tuned over a broad range by applying anisotropic stresses. Samples containing different kinds of QDs were integrated on PMN-PT via a commercial glue. The polarisation angle (θ) and FSS for an exciton confined in a GaAs/AlGaAs QW potential fluctuation can be seen, respectively, in Figs. 2.10(f) and 2.10(g) as a function of the field to the piezo (F). Varying F from 33 to -20 kV/cm (i.e., from compressive to tensile strains) the emission energy $E(\theta,\ F)$ shifts by approximately 4 meV and the polarisation orientation rotates by around 70°. Simultaneously, the FSS shows an anticrossing. The polar plots of Figs. 2.10(c-e) show clearly that FSS and θ change for different fields F. The polarisation angles are given by the orientation of the high-energy emission line of an exciton with respect to the direction of F.
In addition to this result, it was shown a tuning of the FSS for certain QDs down to values that are expected to be small enough to create polarisation entangled photon pairs. Calculations based on $\mathbf{k}\cdot\mathbf{p}$ theory (see section 2.2) and configuration interaction models show that the minimum reachable FSS highly depends on the alignment of stress with respect to the QD elongation direction. The tuning of the FSS was attributed to the anisotropy of the effective mass originating from the HH-LH band mixing.

In conclusion, strain tuning can reversibly shift the QD exciton energy without affecting its emission linewidth (see also section 4.1.2). It can be easily combined with other tuning techniques, such as electric (see sections 4.2 and 4.4) or magnetic field, and allows the on-chip integration of an electrically triggered QD based LED [87], with tuneable FSS by anisotropic stress. On the other hand, the piezoelectric materials have some disadvantages due to the creep, which reduces the speed of operation, and the difficulty to apply locally the stress.

2.5. Semiconductor quantum dot molecules

A QDM−two semiconductor QDs separated by a thin barrier that are quantum mechanically coupled−represents a striking example of the analogy between artificial and natural atomic combinations. In this section, after a review of the literature of PL measurements of QDMs, the growth of vertically stacked QDs and the fundamental physical mechanisms of coupling will be described together with a method for controllably select tunnel coupling of electrons or holes. In conclusion, some recent achievements will be presented, important for the creation of spin entanglement and for reducing the decoherence induced by the fluctuating QD environment, which highlights the advantages of QDMs compared to single QDs in quantum information processing.

2.5.1. Historical synopsis

The simplest QDM is composed of two QDs coupled either vertically (in the growth direction) or laterally (in the growth plane). The first spectroscopic evidence of verti-

cal electronic coupling between the dots was found in year 2001 through magneto-PL experiments [34]. They suggested that external electric field applied along the growth direction, which would control the carrier transfer from one dot to the other, can lead to mixing of the excitonic states. Then, Sheng and Leburton [88] predicted a complex energy spectrum for stacked self-assembled InAs/GaAs QDs and a nonparabolic dependence on the electric field of the interband transition energy, which represents the QCSE in QDM, not encountered in single QD structures.

In these systems the coupling is mediated by electron or hole tunnelling between the dots and it appears in the PL spectra as anticrossings (see section 2.5.3). Magneto-PL spectroscopy of single QDMs showed splittings and anticrossings, indicating a mixing of X_b and X_d [89] and systematic investigations were performed as a function of the barrier width [90, 91].

Substantial progress has been achieved since year 2005 when the QDMs were embedded into a diode structure, which permits the relative energy levels of the two dots to be tuned by choosing a suitable spacer layer thickness and by applying an electric field [35, 36, 92]. In this way, AC patterns in two-dimensional PL intensity maps as a function of electric field and emission energy have been observed, representing single electron tunnelling. At the same time, another source of coupling was experimentally identified as dipole-dipole interactions, supported by theoretical predictions from Nazir *et al.* [93], and photon correlation measurements between each spectral line confirmed unambiguously the inter-dot coupling [94].

The spectroscopic signatures of coupling in charged QDMs were assigned only in year 2006 by Stinaff *et al.* [37] and this has lead to a much better understanding of the properties of QDMs [95, 96], including the origins of spin fine structure [97, 98], supported by advances in the calculation of the optical spectra [99–102]. More recently, the design of molecular spin states and tunnel resonances made it possible to electrically control the g factor for a single confined spin in a QDM [103] and to measure the antibonding molecular ground state [104].

2.5.2. Lateral QDMs

Several difficulties pertain to the fabrication of lateral QDMs using self-assembled QDs, as will be shown in section 4.3. Nevertheless, the lateral geometry has the advantage that more than two dots can be coupled independently via a top gate over the QDM. The electric field can be produced by positioning electrodes on the sides of the QDMs and positive and negative biases can be applied for studying the electron and hole tunnelling on the very same QDM. Moreover, QDs have larger polarisability in the lateral direction respect to the vertical alignment.
Theoretical studies predicted even more complex PL spectra for this geometry with additional ACs, due to the electric field that deforms drastically the wavefunctions within each QD and mixes the energy levels of the single dot [102]. Experimental demonstration of the coupling in lateral self-assembled QDMs has been shown in a limited number of works, such as the dipole-dipole coupling occurring at thickness fluctuations of an AlGaAs/GaAs/AlGaAs QW [105] or the coupling mediated by electron tunnelling in InGaAs/GaAs QDMs [106, 107].

2.5.3. Growth of vertical QDMs and avoided level crossing

QDMs can be vertically stacked in a self-assembled manner during epitaxial deposition [31, 32]. Due to the strain-field generated by the lattice mismatch between InAs and GaAs (see section 3.1.1), two InAs QDs separated by a thin GaAs barrier can be vertically aligned, as will be shown in section 4.4. The strain field from the bottom layer leads to net migration of InAs towards the region above the buried dot, resulting in a larger QD in the second layer [108], with lower energy levels. Another possible way is to realise GaAs/AlGaAs QDMs by filling nanoholes etched on the surface via droplet epitaxy (see section 4.1.1) with two GaAs layers separated by a thin AlGaAs barrier [see Fig. 2.12(a)].

In the following, the better known InAs QDMs will be described. The *indium flush* growth method [108–110] allows the centre emission wavelength of the dot ensemble to be controlled by truncating the dot height (see section 3.1.1 for details). Consequently, this control can be extended to the stacked dot in the QDM. Even if the growth conditions are nominally the same, strain and asymmetry generally lead to slightly different energy levels. A high-resolution scanning transmission electron microscope (HR-STEM) image of a QDM grown with such technique is shown in Fig. 2.11(a).

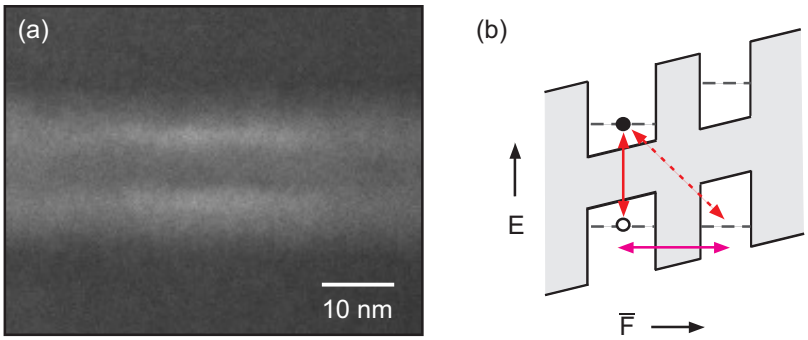

Figure 2.11.: (a) High-resolution scanning transmission electron microscope (HR-STEM) image of a QDM used in this work, realised by partial cap and annealing method with non degenerate dots (4 nm and 3 nm height, separated by 6 nm GaAs barrier). (b) Schematic of the band-edge potential of a QDM showing hole tunnelling resonance (pink arrow) under electric field F. HR-STEM image courtesy of Anja Bonatto-Minella.

The image contrast is given by the InAs (white areas) and the GaAs (black areas) and the dots have slightly different sizes.
By embedding the QDMs in a Schottky diode structure and applying an electric field (F) in the growth direction, the energy levels can be tuned into resonance allowing for quantum tunnelling of holes or electrons between the QDs (see section 2.5.4 for details). This is shown in Fig. 2.11(b), where the bottom dot is taller than the top dot, and a positive electric field compensates the difference in confined energy levels, leading to hole tunnelling.

The following theoretical treatment is given by the work of Doty *et al.* [111]. In contrast to single QDs, the PL lines of a QDM appear split into a doublet when the energy levels of the electrons and holes in the two dots are out of resonance. This

is due to the high number of possible states given by the distribution of charges over both QDs in the molecule. For the sake of simplicity, only the ground state for the electrons and holes in each dot will be considered. The notation $\left(\begin{smallmatrix} eb & et \\ hb & ht \end{smallmatrix}\right)$ is used to label the spatial distribution of the electron and the hole within a QDM, where eb (hb) represents the number of electrons (holes) in the bottom QD and et (ht) denotes the number of electrons (holes) in the top QD. The presence of charge carriers in both dots also leads to two main classes of optical transition: direct or "intradot", where the recombining carriers (forming a direct exciton) are in the same QD, and indirect or "interdot", where the carriers (forming an indirect exciton) are distributed across the QDM. These two configurations can be written in matrix form as $\left(\begin{smallmatrix} 1 & 0 \\ 1 & 0 \end{smallmatrix}\right)$ and $\left(\begin{smallmatrix} 1 & 0 \\ 0 & 1 \end{smallmatrix}\right)$ and they are shown by the continuous and dashed red arrows of Fig. 2.11(b), respectively. Under electric field, direct excitons show very weak QCSE, similar to the single dot case, whereas indirect excitons appear in spectral maps as diagonal lines, due to the spatial separation between the dots.

Quantum tunnelling is a quantum phenomenon active when the confined energy levels of the two QDs are in resonance. The electrons and holes can penetrate the potential barrier (GaAs barrier in this case), which is higher than their kinetic energies, but not simultaneously because of the non degenerate energy levels. The relative sizes of the two dots and the sign of the applied electric field will determine the particular charge carrier that tunnels (see section 2.5.4). Similar to the H_2 molecule with the bonding and anti-bonding states, coherent tunnelling [34] results in the formation of molecular orbitals delocalised over both dots and the barrier. These molecular states are constructed from the symmetric and antisymmetric combination of the basis states, i.e., $\frac{1}{\sqrt{2}}\left[\left(\begin{smallmatrix} 1 & 0 \\ 1 & 0 \end{smallmatrix}\right)+\left(\begin{smallmatrix} 1 & 0 \\ 0 & 1 \end{smallmatrix}\right)\right]$ and $\frac{1}{\sqrt{2}}\left[\left(\begin{smallmatrix} 1 & 0 \\ 1 & 0 \end{smallmatrix}\right)-\left(\begin{smallmatrix} 1 & 0 \\ 0 & 1 \end{smallmatrix}\right)\right]$. As a result, avoided level crossings or ACs between the direct and indirect excitons can be measured in electric field dependent PL spectral maps [35], as shown in Fig. 2.12(a) for another material such as GaAs/AlGaAs QDM embedded in a Schottky diode.

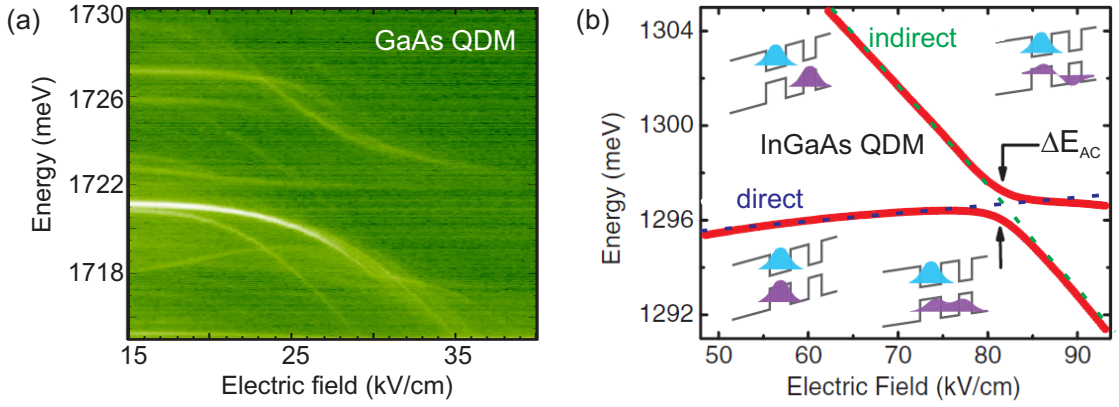

Figure 2.12.: (a) Anticrossing (AC) pattern representing electron tunnelling in GaAs/AlGaAs QDMs realised by droplet etching epitaxy. (b) Schematic of the AC pattern for the X^0 in InGaAs/GaAs QDM with 2 nm GaAs barrier. The dotted lines represent the indirect (green) and direct (blue) excitons in the non interacting case. Figure (b) readapted from Ref. [104].

In a similar way, Fig. 2.12(b) shows the calculated AC of the X^0 in InGaAs/GaAs QDM, originated by hole tunnelling through a 5 nm GaAs barrier. At fixed value of the electric field, the PL lines indicate two recombinations, the indirect and the direct, with different spatial distributions of the electron and hole. At the crossing point of the direct and indirect lines there is the formation of bonding and antibonding molecular states, indicated by the anticrossing. The ACs have a magnitude or AC energy gap (ΔE_{AC}), defined as the energy difference between the upper and the lower branches. This reflects the overlap of the charge-carrier wavefunctions in the interdot region given by the degree of tunnel coupling, which is in turn determined by the properties of the barrier between the dots.

The system can be described by a simple matrix Hamiltonian by considering the two possible states for the hole and the electron trapped in the bottom dot. In the atomic-like basis state, $\left(\begin{smallmatrix}1&0\\1&0\end{smallmatrix}\right)$ and $\left(\begin{smallmatrix}1&0\\0&1\end{smallmatrix}\right)$, the Hamiltonian reads

$$\hat{\mathrm{H}}^{X^0} = \begin{pmatrix} E_0 & -t_{X^0} \\ -t_{X^0} & E_0 - edF \end{pmatrix}, \tag{2.37}$$

with E_0 the exciton energy, t_{X^0} the tunnelling rate and $-edF$ takes into account the strong electric field dependence of the indirect excitons with a barrier d.
At large F the hole is away from resonance and the tunnel coupling is the minimum. This is the Heitler-London limit, used for analysing the states of the diatomic molecules like H_2 [112], and the eigenvalues are the energies of the two basis. The resonance point corresponds to $F = 0$ and the eigenvalues of 2.37 are $E_0 - t_{X^0}$ and $E_0 + t_{X^0}$. The eigenstates evolve to molecular orbitals, respectively, the symmetric (bonding) and antisymmetric (anti-bonding) combination of the two basis states, where we have assumed that the bonding orbital has lowest energy ($t_{X^0} > 0$).

Besides the X^0 anticrossings, more complex AC patterns have been observed when more particles are involved in the optical transitions. Singly and doubly charged excitons in a single QDM are characterised by X-shaped patterns [37, 95, 98], as will be explained more in detail in section 4.4 for the X^+. The fine structure observed arises from combinations of quantum mechanical tunnelling, Coulomb and exchange interaction and the Pauli exclusion principle (see section 2.5.5).

2.5.4. Controllable coupling of electrons or holes

As shown in the work of Bracker *et al.* [33], both electron and hole tunnelings can be controlled by intentionally growing QDMs with different truncation heights for each dot, by means of the *indium flush* method. When the taller dot is on top, electron energy levels lie closer to the bottom of CB and a positive applied electric field brings them into resonance. Similarly, when the taller dot is on the bottom a positive applied electric field brings the hole levels into resonance [see Fig. 2.11(b)].

In Ref. [33] two configurations were considered, each has one dot truncated to 2.5 nm and one dot truncated to 4 nm but the order of the dots is reversed in the two cases and the separation between them is 4 nm. Figures 2.13(a) and 2.13(b) show the calculated relative energy levels of the X^0 states as a function of applied electric field when the

taller dot is at the top or the bottom, respectively.

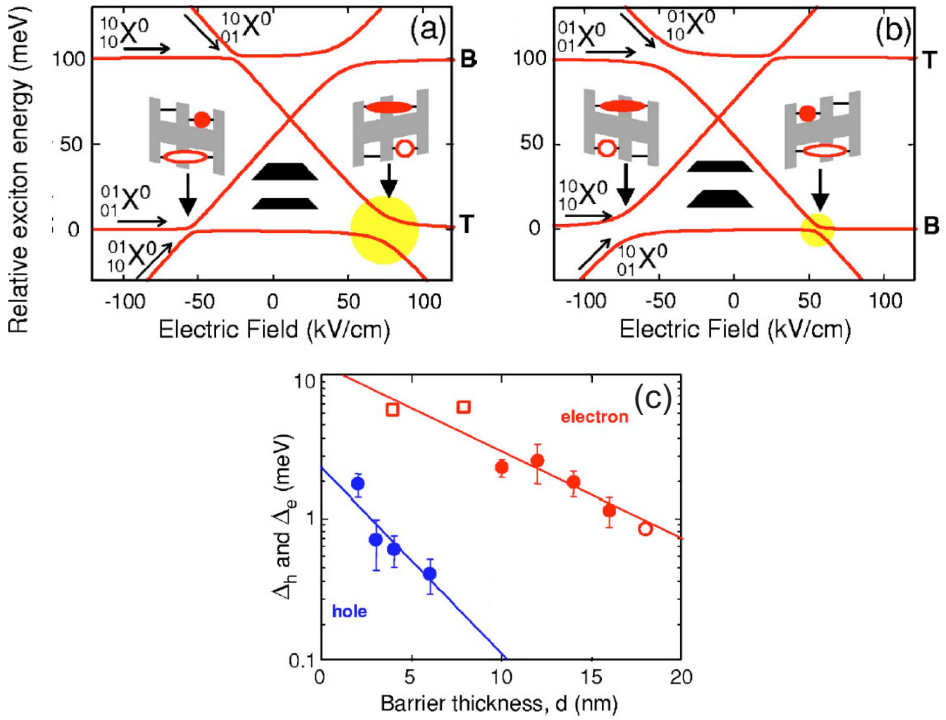

Figure 2.13.: Calculated energy levels for two InGaAs/GaAs QDMs with 4 nm barrier: (a) 4 nm dot above 2.5 nm dot and (b) 2.5 nm dot above 4 nm dot. (c) Measured AC energy gaps for electrons and holes as a function of the barrier thickness. Figure readapted from Ref. [33].

Each panel has four ACs, two for electron and two for hole tunnelings with the hole or the electron confined in either the top or bottom dot, respectively. Following the behaviour with electric field, small AC energy gaps are visible at negative electric fields, when the hole levels come into resonance, and larger AC energy gaps at positive electric fields, when the electron levels are in resonance [see Fig. 2.13(a)]. This is due to the lighter effective mass of electrons than heavy holes, leading to higher rates of tunnelling for electrons. In Fig. 2.13(b) the situation is reversed.
In conclusion, the charge carrier that tunnels can be selected by choosing the relative heights of the two dots and the substrate doping. In fact, for an n-doped (p-doped) substrate, negative (positive) applied electric fields flood the QDM with electrons. Additionally, only the lower half of the calculated energy levels in Figs. 2.13(a) and 2.13(b) is accessible, due to the energy difference for the two possible spatial locations of the particle that does not tunnel. Figure 2.13(c) shows the measured AC energy gaps energies for electrons and holes in samples with a variety of barrier thicknesses. The tunnelling energies[3] were extracted from PL spectra of the singly charged exciton, in order to get the information about the single electron and hole. As expected, the tunnelling energies for electrons are nearly an order of magnitude larger than those for

[3]The relation between the AC energy gap (ΔE_{AC}) and the tunnelling energy (t) for the single hole/electron is $\Delta E_{\mathrm{AC}} = 2|t|$.

holes. Other experiments performed on non partially capped and annealed InAs QDMs have extrapolated a slope for the tunnelling energies about twice the values reported above [113]. This is due to different amount of indium in the dot region and different dot shape.

2.5.5. Singlet-triplet states in positive trions

This section deals with the spin properties of X^+ in InGaAs/GaAs QDM and gives a theoretical introduction following the work of Doty *et al.* [111], in order to understand section 4.4.

The spin character of the X^+ is determined by both electron-hole and hole-hole exchange interactions [98], since there are two holes and one electron in the optically excited state. Similarly to the single dot case, the recombining electrons and holes have opposite spin projections to conserve angular momentum. Moreover, an electron and hole confined in the same dot experience an electron-hole exchange interaction J_{eh}, which splits X_b and X_d states, as explained in section 2.4.2. When the electron and hole are in separate dots, J_{eh} is drastically reduced, since it depends on the overlap of electron and hole wavefunctions.

Concerning the interactions between two holes, there are three possible spatial distributions: both holes in the bottom dot, one hole in each of the top and bottom dots, and both holes in the top dot. When both holes are in the same dot, they are in a spin singlet configuration, due to the Pauli principle. When the holes are located in separate dots, singlet and triplet configurations of the spins are possible.
In general, there are six possible spin configurations for X^+: $\left(\begin{smallmatrix}\uparrow & 0\\ \Downarrow\Uparrow & 0\end{smallmatrix}\right)_S$, $\left(\begin{smallmatrix}\uparrow & 0\\ \Downarrow & \Uparrow\end{smallmatrix}\right)_S$, $\left(\begin{smallmatrix}\uparrow & 0\\ \Downarrow & \Uparrow\end{smallmatrix}\right)_T$, $\left(\begin{smallmatrix}\uparrow & 0\\ \Downarrow & \Downarrow\end{smallmatrix}\right)_T$, $\left(\begin{smallmatrix}\uparrow & 0\\ \Uparrow & \Uparrow\end{smallmatrix}\right)_T$ and $\left(\begin{smallmatrix}\uparrow & 0\\ 0 & \Downarrow\Uparrow\end{smallmatrix}\right)_S$, where $\uparrow$ represents the spin of the electron, assumed up in the bottom dot, and $\Uparrow$ and $\Downarrow$ are the hole pseudospin basis with dominant HH component, due to confinement and the strain effect on the VBs (see section 2.3). The last singlet-spin configuration is an excited state that can be neglected, because the respective energy values are far from the region of interest (see appendix A.1). The $\left(\begin{smallmatrix}\uparrow & 0\\ \Downarrow & \Uparrow\end{smallmatrix}\right)_S$ is the antisymmetric hole spin singlet $\left[\frac{1}{\sqrt{2}}(|\Downarrow_1\Uparrow_2\rangle - |\Uparrow_1\Downarrow_2\rangle)\right]$ and $\left(\begin{smallmatrix}\uparrow & 0\\ \Downarrow & \Uparrow\end{smallmatrix}\right)_T$ the symmetric hole spin triplet with net angular momentum zero $\left[\frac{1}{\sqrt{2}}(|\Downarrow_1\Uparrow_2\rangle + |\Uparrow_1\Downarrow_2\rangle)\right]$.

Because tunnelling conserves spin, only the $\left(\begin{smallmatrix}\uparrow & 0\\ \Downarrow & \Uparrow\end{smallmatrix}\right)_S$ single state can tunnel couple with $\left(\begin{smallmatrix}\uparrow & 0\\ \Downarrow\Uparrow & 0\end{smallmatrix}\right)_S$, which must be in a spin singlet because the holes are in the same dot. The triplet state $\left(\begin{smallmatrix}\uparrow & 0\\ \Downarrow & \Uparrow\end{smallmatrix}\right)_T$ passes through the AC region with no coupling [see Fig. 4.25(d) in section 4.4.3]. The two additional triplet lines $\left(\begin{smallmatrix}\uparrow & 0\\ \Downarrow & \Downarrow\end{smallmatrix}\right)_T$ and $\left(\begin{smallmatrix}\uparrow & 0\\ \Uparrow & \Uparrow\end{smallmatrix}\right)_T$ have parallel hole spins and are separated in energy by J_{eh}.
The AC energy gap is determined by both the tunnelling matrix element and the electron-hole exchange [98]: $\Delta E_{AC} = 2\sqrt{2|t|^2 + (J_{eh})^2}$.

Another effect of J_{eh} is the lifting of the energy degeneracy between $\left(\begin{smallmatrix}\uparrow & 0\\ \Downarrow & \Uparrow\end{smallmatrix}\right)$ and $\left(\begin{smallmatrix}\uparrow & 0\\ \Uparrow & \Downarrow\end{smallmatrix}\right)$, which are combined for the formation of $\left(\begin{smallmatrix}\uparrow & 0\\ \Downarrow & \Uparrow\end{smallmatrix}\right)_S$ singlet and $\left(\begin{smallmatrix}\uparrow & 0\\ \Downarrow & \Uparrow\end{smallmatrix}\right)_T$ triplet states. As a result, a mixing between $\left(\begin{smallmatrix}\uparrow & 0\\ \Downarrow & \Uparrow\end{smallmatrix}\right)_S$ and $\left(\begin{smallmatrix}\uparrow & 0\\ \Downarrow & \Uparrow\end{smallmatrix}\right)_T$ occurs, leading to the "wiggling" of the triplet-like state as it passes through the AC region [101]. This "wiggled" line will be

shown in the measured PL spectral map of section 4.4. Following the triplet-like state continuously, it results that the mixing swaps the spins of the two holes in separate dots. Similar mixing was induced by the hyperfine interaction for inducing a spin flip of electrons in electrostatically defined QDs [27].

2.5.6. Advantages of QDMs

QDMs have potential application as quantum gates in quantum information processing [27–29], mainly due to the possibility of initialising and controlling entanglement between solid-state qubits [38–40, 100, 114]. For example, a significant reduction of the optical FSSs in coupled double QDs with high tunnelling rates, without any decrease in the optical oscillator strength, has been predicted by Ramirez *et al.* [115]. This would make strongly coupled vertical QDM better sources of entangled photon pairs than single dots (see section 4.2.4).

An important step towards the realisation of a quantum network was done by Kim *et al.* in year 2011 [38]. They demonstrated ultrafast optical control of a two-qubit system consisting of two-electron spins, each on separate tunnel-coupled QDs. For this study, two vertically stacked self-assembled InGaAs QDs were grown separated by 9 nm tunnel barrier of GaAs/$Al_{0.3}Ga_{0.7}$As/GaAs (3/3/3 nm) such that the electrons can coherently tunnel between the dots, as shown in Fig. 2.14.

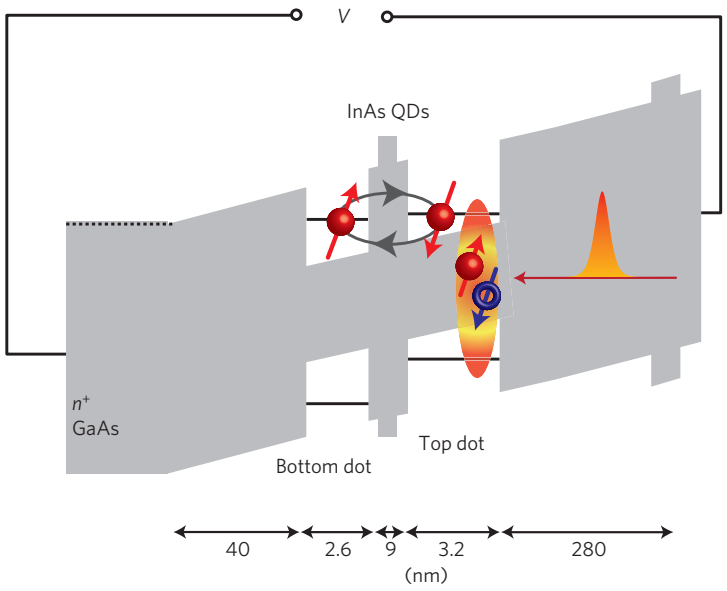

Figure 2.14.: Schematic of the device with two InGaAs/GaAs QDs separated by a thin GaAs/AlGaAs barrier. The electrons are charged in each dot and the spins are coupled by coherent tunnelling. Laser fields are used to initialise, measure or rotate the spins through a real or virtual exciton resonantly excited in the top dot. Figure from Ref. [38].

The two QDs have different thicknesses such that the emission energies are different and can be excited with a resonant laser frequency. In order to apply electric field bias and control the tunnelling, the QDs are incorporated into a Schottky diode [33, 35].

As a result, the two-electron spin state is initialised through optical pumping. The magnitude of the exchange energy determines the interaction strength between the dots, which in turn defines the speed of the entanglement control. They found an exchange energy of 30 GHz, which enables an order of magnitude faster gate speeds, if compared to the 2 GHz obtained in electrically defined QDs [27]. In particular, they demonstrated single-qubit gates using short laser pulses, and two-qubit gates using longer laser pulses.

Another experiment with QDM has been recently performed in order to limit the dephasing due to the hyperfine interaction between the electronic and the nuclear spins in a QD [40]. The idea was to use two vertically tunnel-coupled QDs embedded in a diode, with a single electron in each dot. By seeking the so-called "sweet spot" in the bias parameters, where the qubit subspace spanned by the singlet state and the triplet state with spin z projection $m_s = 0$ (see section 2.5.5) has no first-order dependence on the magnetic field as well as electric-field fluctuations, it was possible to prolong the coherence time T_2^* by two orders of magnitude up to 200 ns. This can be considered as the solid-state analog of the coupling via the optical Raman between two clock states [116].

3. Experimental methods

The chapter gives an overview over the experimental methods and materials, which were used in this work. First, the MBE technique for optimising the growth of QD- and QDM-based devices is presented. Then, a crucial tool for a first characterisation of the samples, the atomic force microscopy (AFM), is introduced. The ferroelectric crystal used for transferring stress to the QDs is also described in detail. The final sections focus on the processing steps required to fabricate strain-tunable devices and the optical setup adopted.

3.1. Molecular beam epitaxy (MBE)

MBE is a physical growth process in an ultra-high vacuum (UHV) environment, where high purity single crystal films are deposited by the interaction of atomic or molecular beams of thermal energy on a heated crystalline substrate or by, using the words of The New York Times, "spray painting...with atoms" [117]. In fact, "epitaxy" comes from the Greek *epi* (above) and *taxis* (in an ordered manner).
Since its introduction in the 1970s by Alfred Y. Cho [118] this technique has been used for the preparation of new class of devices, such as semiconductor lasers and LEDs [119]. The low growth temperature and growth rate allow a precise control of the composition and doping profiles to one monolayer (ML) and make it possible to realise atomically abrupt interfaces. This together with the improvements in material purity has in turn made the investigation of the physics of low dimensional systems possible, leading to the observation of correlated electron effects such as the fractional quantum hall effect [120].

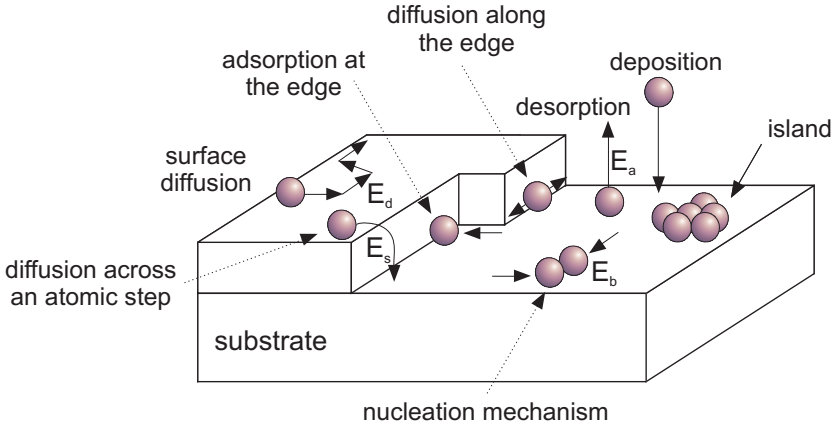

Figure 3.1.: Behaviour of adatoms in the surface deposition process. Figure readapted from Ref. [121].

During the MBE process three different phases are involved: the crystalline substrate, the gas of the molecular beams and the near-surface transition layer, where the ballistic fluxes interact with the hot substrate. This phase is described by different kinetic processes and each event has a characteristic time given by the activation energy E_a and a length scale. As shown in Fig. 3.1, the typical kinetic processes are adsorption and desorption, condensation and dissociation and migration on the flat surface. The activation energies and the resulting dominant process can be studied by a thermodynamic description of the energies of the thin film and vapour phases [122]. The atoms can reach a step (boundary between two regions of the surface differing by one interplanar spacing) or a kink (corner position) and be incorporated, or form a cluster with other adatoms on the crystalline surface. The adatoms have higher probability of incorporation at steps because there is a higher number of dangling (unsaturated) bonds at step edges with respect to terraces. The surface diffusion depends on several parameters as the substrate temperature (T_{sub}), fluxes, atomic species, surface reconstruction, and substrate misorientation. For example, the diffusion length of GaAs on the (001) surface was estimated to be $\sim$1 μm along the [110] direction at 560°C [123].

In general, three modes of crystal growth on flat surfaces can be distinguished, illustrated schematically in Fig. 3.2.

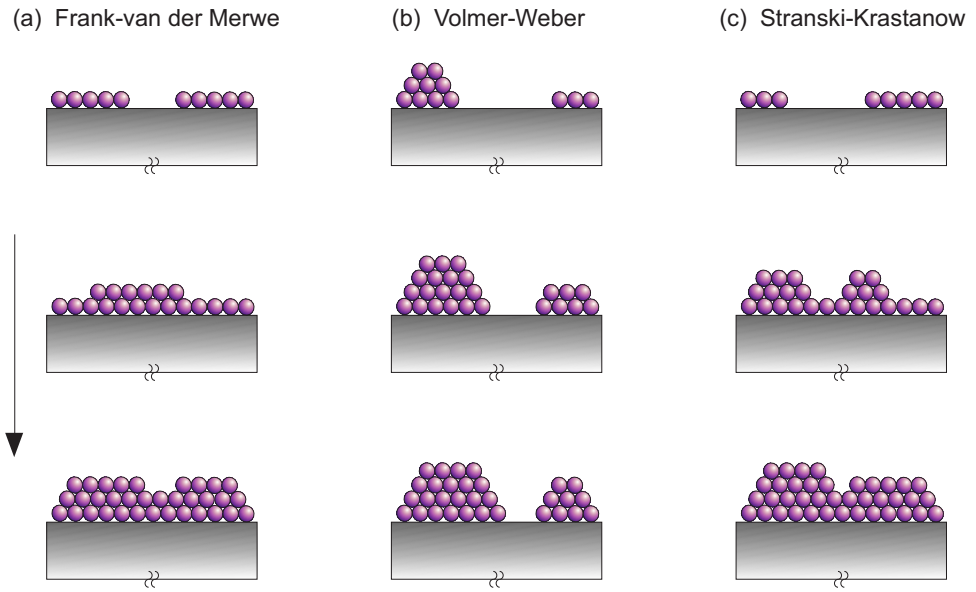

Figure 3.2.: Schematic of the crystal growth modes: a) Frank-van der Merwe (FvdM), b) Volmer-Weber (VW), and c) Stranski-Krastanow (SK).

The layer-by-layer growth, or Frank-van der Merwe (FvdM) [124], occurs when the epilayer free energy (γ_{epi}) plus the free energy of the substrate-epilayer interface (γ_i) is smaller than the substrate free energy (γ_{sub}). Therefore, it is energetically favourable for the material to cover the surface. When $\gamma_{epi} + \gamma_i > \gamma_{sub}$ the material forms small clusters, in order to minimise the surface energy. This island growth is called Volmer-Weber (VW) [125]. The intermediate case, or Stranski-Krastanow (SK) [126], is defined by $\gamma_{epi} + \gamma_i(t) < \gamma_{sub}$, when the thickness t is small and $\gamma_{epi} + \gamma_i(t) > \gamma_{sub}$, when t is large. For example, when the epilayer has a different lattice parameter to the substrate

(e.g., 2−10%), under certain conditions island growth becomes favourable after few MLs of growth. This thin layer is called a wetting layer (WL) and the islands are called QDs, due to the fact that they are small enough to provide carrier confinement in all three dimensions (see section 2.4.1).

The samples studied in this work have been realised with a MBE Omicron 4-inch. A schematic of the MBE chamber is shown in Fig. 3.3.

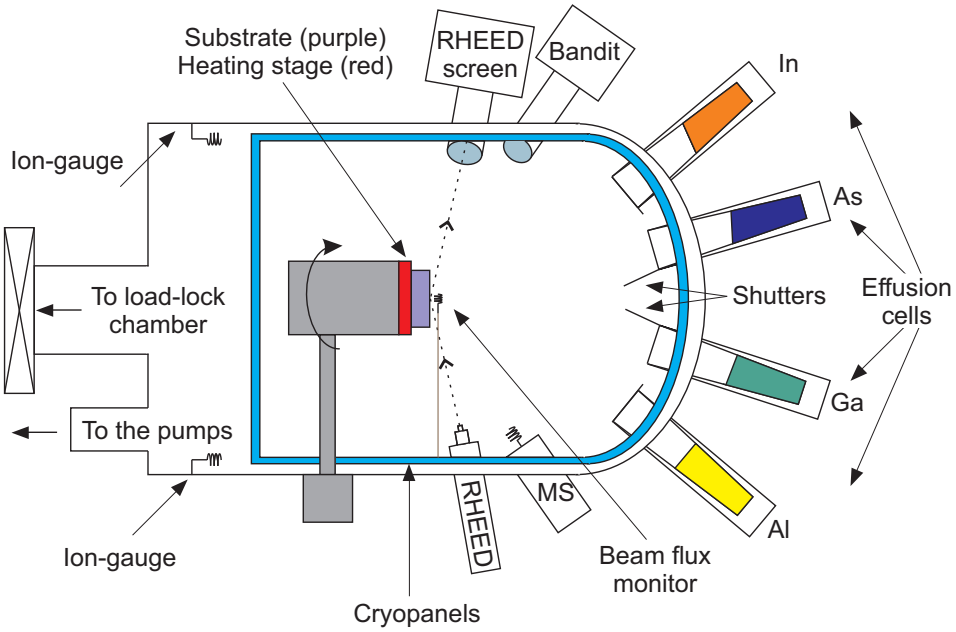

Figure 3.3.: Schematic of the molecular beam epitaxy (MBE).

The system consists of a stainless-steel growth chamber of one-meter diameter. Ion-getter, cryogenic and Titanium sublimation pumps ensure UHV conditions inside the chamber of the order of 10^{-11} mbar, with the residual gas being essentially H_2. The substrate heater, which can reach 1200°C, is capable of continuous azimuthal rotation around its axis. The 2-inch GaAs wafer is clamped at the edges on a molybdenum holder. The flux stability is achieved by computer control of the temperatures of effusion cells containing Gallium, Aluminium, Indium and Arsenic. The latter can be sublimated from a valved cracker cell as tetramers As_4 or dimers As_2. The sources are displaced around the substrate in such a way to make the composition and the thickness of the grown crystal as uniform as possible, with rotation of the substrate. Other two materials, very important for the fabrication of devices (see sections 4.2.1 and 4.4.1), are Silicon and Carbon, that can be grown using sublimation sources with solid filaments. Shutters operating typically at 0.1 s allow precise control over layer thicknesses to within a fraction of a ML. Moreover, there are three ion-gauges on the system: One is attached on a movable arm, so that it can be moved underneath the substrate for measuring directly the beam flux incident on the wafer, two are mounted on the wall of the chamber for the background pressure. A liquid N_2 cryopanel surrounds completely the growth environment and is essential for pumping the residual gas and reducing the cross-talk between the different cells.

The estimate of the absolute GaAs substrate temperature is obtained by the kSA band-edge thermometry system, a sensor using the temperature-dependent optical absorption edge of GaAs. This is more precise than the thermocouple measurement, where the filament is not in contact with the substrate. Moreover, a mass spectrometer (MS) permits the masses of the elements in the chamber to be identified.
Connected to the growth chamber via a UHV transfer chamber, there is a load-lock chamber for introducing the samples from the air, a preparation chamber, where the water and hydrocarbons are degassed from the substrates prior the growth, and a buffer module for storing them (not shown). All the chambers are separated from each other by gate valves. A magnetic transfer mechanism in combination with trolleys allows the introduction of the substrate into the growth chamber keeping the vacuum conditions.

A very important tool, used for checking the structure and morphology of the crystalline surface during growth, is the Reflection High Energy Electron Diffraction (RHEED). This technique employs a high energy ($\sim$10 KeV) electron beam, directed on the sample surface at grazing incidence ($1° - 3°$). The diffraction pattern imaged on a phosphor screen on the opposite side of the chamber is the result of the diffraction of the electron beam from the first few atomic layers. This geometry avoids any interference of the RHEED apparatus with the molecular beams.
In the ideal case where only the crystal surface contributes to the diffraction intensity, the reciprocal lattice is given by parallel infinite rods, because it is the 3D projection of a 2D lattice. As shown in Fig. 3.4, the diffraction pattern in the Ewald construction consists of a series of spots placed on a half circle (Laue's zone, L) and it is obtained by the intersection of the Ewald sphere (constant energy surface of the scattered beam) with the rods of the reciprocal lattice.

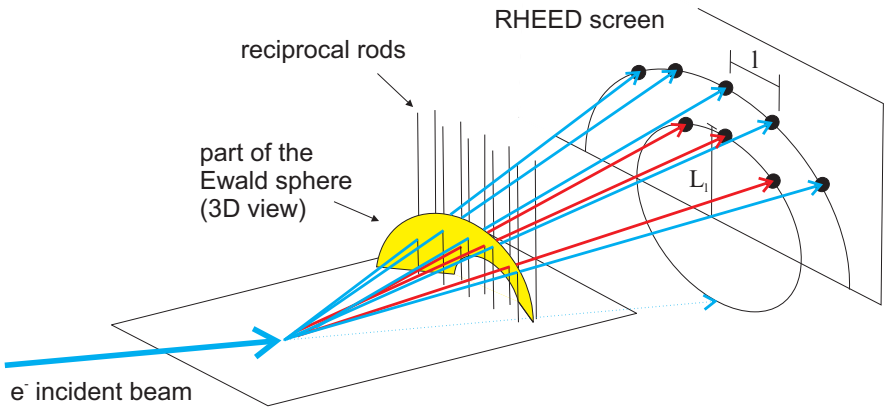

Figure 3.4.: Intersection of the Ewald sphere with the rods of the reciprocal lattice (3D view). Figure readapted from Ref. [127].

Due to finite thickness of the Ewald sphere related to the divergence of the electron beam, and to thermal vibrations and lattice imperfections increasing the rod's size, the real RHEED image consists of a series of streaks with modulated intensity, rather than points. For example, the RHEED pattern from a SK growth (see section 3.1.1) results in spotty features.
The RHEED oscillations during the MBE deposition [128] are a clear indication of the

layer-by-layer growth, as shown in Fig. 3.5.

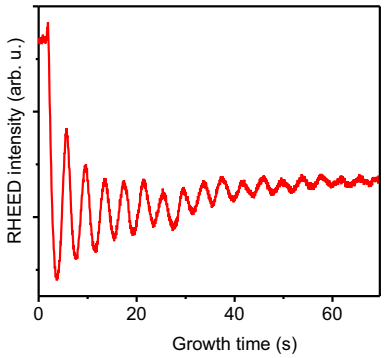

Figure 3.5.: RHEED intensity during the GaAs growth at 0.3 μm/h.

Before the growth of GaAs on GaAs (001) substrates, the surface has large flat terraces and the reflectivity of the specular beams is high. This corresponds to a maximum of the intensity for the specular RHEED spots and minimum diffused intensity. The beginning of the growth gives rise to random nucleation of 2D islands and reduction of the surface reflectivity. The islands eventually merge with each other forming a complete layer (ML). The RHEED intensity is characterised by maxima and minima at half layer coverage and the period of the oscillations is a measure of the time needed to deposit a ML or the growth rate. Before the first layer is completed, new islands start to grow on the second layer damping the oscillations.

3.1.1. Growth of optically active QDs

The QDs employed in this thesis are mainly grown by SK mode. In the case of InAs and GaAs the lattice mismatch is about 7%. When In and As[1] are deposited on GaAs (001) substrates, the InAs will first grow pseudomorphically by adopting the same in-plane lattice constant as the substrate and forming the WL. The elastic energy accumulated in this process is partially relieved after the deposition of the critical thickness θ_{crit} ($\sim$1.6 ML of InAs) by a lateral relaxation of the atomic planes and the nucleation of self-assembled 3D islands, as shown in Fig. 3.6.

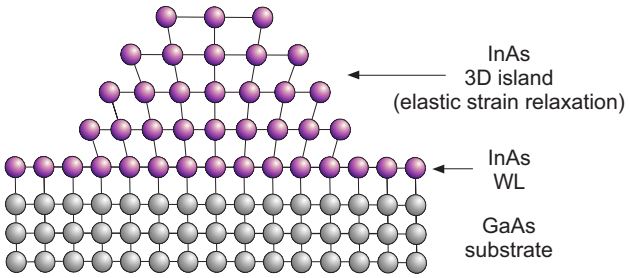

Figure 3.6.: Schematic representation of the lattice distortion in a 3D island (InAs) grown on substrate (GaAs) by SK mode.

[1]The valved cracker arsenic source is operated in this work in As_4 mode [129].

These dots have typical dimensions in the range from 10 to 50 nm in diameter and from 3 to 17 nm in height. The transition from 2D to 3D growth manifests as a rapid increase in the RHEED intensity. After θ_{crit}, the pattern changes from streaky to spotty with higher intensity in the spots. The crystal facet structure of the island can be analysed by the so-called chevron images [130].

In order to control the QD height and narrow the dot size distribution, an *indium flush* growth method [108–110] was used and the dots obtained are called partially capped and annealed (PCA). After the growth of the dots at $T_{sub} = 500°C$, a thin GaAs capping layer ($\sim$2.5 nm) is deposited at the same temperature. The "wetting" of the dot is limited because of the strain relaxation of the InAs at the top of the dot and GaAs will grow preferentially on the WL. The subsequent annealing step at 570°C for 180 s removes the InAs from the exposed portion of the pyramidal dots. This truncation in the z direction results in pancake-shaped dot of defined thickness. As a result, there is a modification of the composition profile, due to the intermixing of the InAs with the surrounding GaAs [131]. Finally, the QDs are capped with GaAs so that they can luminesce and are called InGaAs QDs. The emission wavelength is centred $\sim$910 nm, matching the high efficiency region of the silicon detectors (see section 3.5) with a good signal-to-noise ratio.

If the lattice parameters of the QD and the surrounding matrix are matched (e.g., GaAs/AlGaAs QDs), the SK mode is not anymore favourable and the 3D islands can be obtained either by VW mode [132] or by infilling nanoholes [133–135], as described more in detail in section 4.1.

3.2. Atomic force microscopy (AFM)

AFM microscopy is a technique for imaging, measuring and manipulating matter at the nanoscale by measuring or applying a force between a probe and the sample [136]. AFM is one kind of scanning probe microscopy developed in 1986 by Binnig, Quate and Gerber and is used here to measure the topography of the sample surface.
When a cantilever with a sharp tip approaches slowly towards the surface, the cantilever bends following Hooke's law, because of the Van der Waals attraction between the atoms at the tip and the surface. These forces can be described by Lennard-Jones potentials. In this work, the cantilever has been operated in "tapping mode", this means driving it near its resonant frequency by a piezoelectric crystal. The tip-surface interaction forces damp the amplitude of vibration deflecting the cantilever vertically and laterally and the optical lever reflects a laser beam on a four-segment photo-detector. The differences between the signals on the segments indicate the position of the laser spot on the detector and thus the angular deflections of the cantilever. The AFM not only measures the force on the sample but also regulates it via a feedback loop, keeping the amplitude of oscillation of the cantilever constant by adjusting the voltage applied to the scanner.

The apparatus used was a Digital Instruments Veeco Multi-mode Nanoscope IV, and the software to run it was Nanoscope version 7.30. The maximum scan size is 125 μm. The resolution in the vertical direction is 0.1 nm whereas the lateral resolution is affected more by the tip shape (order of nanometre). The tips used here had a

$(3 - 6)$ μm tall pyramid with $(15 - 40)$ nm end radius, a nominal curvature radius $\sim$2 nm, and half cone angle $< 10°$ at 200 nm from the apex.

If no extra pre-patterning is applied to the substrate surface, a typical AFM image of InAs QDs formed randomly on the surface by SK mode is shown in Fig. 3.7.

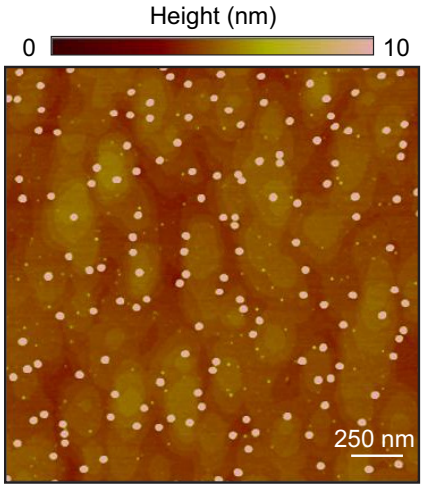

Figure 3.7.: Atomic force microscope (AFM) image (2 μm $\times$ 2 μm) of a layer of InAs/GaAs self-assembled QDs. Each bright spot corresponds to a dot with typical lateral diameters of $(25 - 35)$ nm and a height of $(8 - 15)$ nm.

3.3. Ferroelectric crystal (PMN-PT)

Strain can be used to modify the electronic properties of semiconductors [84, 137]. In order to induce stress in the QD layer, $[Pb(Mg_{1/3}Nb_{2/3})O_3]_{0.72}$-$[PbTiO_3]_{0.28}$ crystals (PMN-PT) have been exploited as substrates onto which GaAs-based thin nanomembranes containing QDs are integrated (see section 3.4).

The PMN-PT is a rhombohedral crystal, which shows extraordinary electrostrictive properties given by the electrical domains present in the material. In fact, below the Curie temperature, the intrinsic electric dipole moments make the PMN-PT a ferroelectric relaxor. If no external electric field (F) is applied to the single crystal, these dipole moments are randomly aligned. When F is larger than the coercive field (F_c), the dipoles align along the direction of F leading to an expansion of the crystal in that direction and ultrahigh strain ($> 0.5\%$) can be generated, with little hysteresis [138]. Because of a very high residual polarisation of the crystal, the domains remain stable even after removal of the field.

Since the measurements in this work were performed between 5 and 10 K, it was important to ensure that the domains are well oriented after the cooling process. This was realised by positively poling the crystal at room temperature by applying $F \sim$10 kV/cm between the top and the bottom surfaces of the crystal, and by keeping this field constant during the cooling process in order to maintain the poled state. After the poling, the voltage applied induces a nominally isotropic strain $\varepsilon_{//}$ perpendicular to F, produced by the polar end of the domains which contract the top and bottom surfaces.

Due to the rigidity of the crystal also the side surfaces are anisotropically strained by $\varepsilon_{\perp}$, with $\varepsilon_{//} \approx -0.7\ \varepsilon_{\perp}$ [139]. Figure 3.8 shows the relationship between $\varepsilon_{//}$ and F at room temperature.

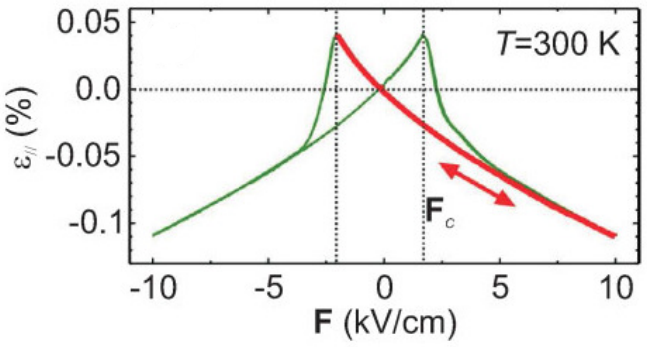

Figure 3.8.: In-plane strain ($\varepsilon_{//}$) as a function of the applied electric field (F) recorded along the [100] edge of a 0.72PMN-0.28PT(100) substrate at 300 K. Figure from Ref. [140].

Compressive strains $\varepsilon_{//} \approx -0.11\%$ can be achieved for an out-of-plane electric field of 10 kV/cm [140]. If an electric field of values $-F_c < F < 0$ is applied, the direction of the strains is inverted, since the ferroelectric crystal switches the orientation of its polarisation at the coercive field $|F| = F_c$. It was shown that at cryogenic temperatures F_c is larger than 20 kV/cm [141], allowing the application of both compressive and tensile stresses. Since there is no difference for positive and negative electric fields if $|F| > |F_c|$, the convention that positive electric field corresponds to compressive in-plane strain is used (see red curve in Fig. 3.8).

3.4. Device fabrication

Different devices have been realised in the recent years in order to Stark shift (change in energy with electric field) the QD emission [81] for controlling the charge and the energy of the excitonic species [142], or for inducing stress in the QD layer [77, 143].
The possibility to apply strain to QDs (see section 4.1.2) and combined electric and strain fields to QDs (see section 4.2) and QDMs (see section 4.4), embedded in n-i-p or n-i-Schottky diodes grown by MBE, was part of the investigation of this work. The optimised device fabrication is described in Fig. 3.9(a).
A 100 nm-thick $Al_{0.75}Ga_{0.25}As$ sacrificial layer was grown underneath the diode structure. Metal pads were defined on the as-grown sample surface by means of photolithography, thermal evaporation of 3 nm Cr followed by 100 nm Au and lift-off. A sulphuric acid solution (H_2SO_4:H_2O_2:H_2O) was used to etch the uncovered area, down past the sacrificial layer. The latter can be easily removed by HF solution, leaving intact the overlying membranes that are now loosely bound to the substrate. Finally, the GaAs nanomembranes were transferred via a flip-chip step onto the top surface of gold-coated 200- or 300-μm-thick PMN-PT (see section 3.3) by thermo-compression bonding [144, 145]. This step consists of a combination of pressure (few MPa via a weight)

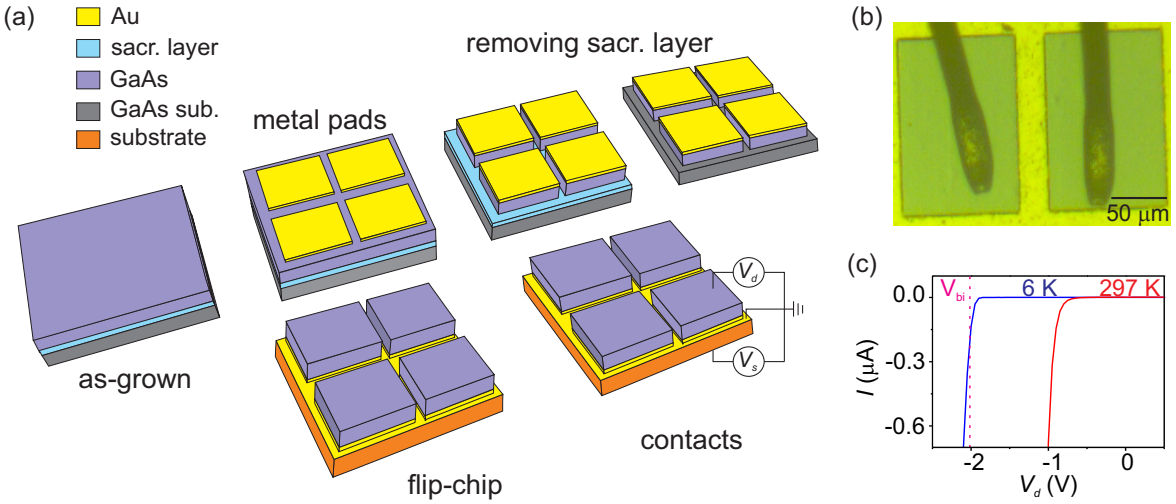

Figure 3.9.: (a) Sketch of the device fabrication from the MBE as-grown sample to the wire-bonding. The substrate in this work is the PMN-PT. (b) Optical microscopy image of two devices. The green (yellow) areas are the n-doped layer of the membrane-diodes (gold coated PMN-PT). (c) Current-voltage (I-V) characteristic of a diode at room (297 K) and low (6 K) temperatures from the sample used in section 4.4.

and heat (300°C via a hot plate) applied in order to bond the Au layers, which act as bottom mirror, ground electrical contacts and provide a good strain transfer between the PMN-PT substrate and the GaAs membranes. To ensure that the top and bottom surfaces are electrically isolated, the edges of the ferroelectric crystal were polished by sandpaper. Aluminium wires 25-μm-thick were wedge-bonded to the Au-coated PMN-PT and to the n-doped GaAs, in order to apply the biases to the piezo (V_p) and to the diode (V_d), respectively. The top view of the membranes sticking on the top of the PMN-PT after wire-bonding is shown in the optical microscopy image of Fig. 3.9(b). The diodes were always operated in reverse bias but it was also demonstrated that they can work in forward bias by injecting carriers electrically [145]. The current-voltage (I-V) characteristic at low temperature with ideal built-in voltage (V_{bi}) of 2.05 V and leakage current less than 1 nA for $V_d > 0$ is represented in Fig. 3.9(c).

3.5. Micro-photoluminescence setup

Standard low-temperature (4−10 K) micro-PL (μ-PL) spectroscopy was used for the optical characterisation of the QD- and QDM-based devices. The QD structures are optically excited by a 532 nm continuous-wave frequency doubled Nd:YVO4 laser, far above the bandgap of GaAs. An electron-hole pair can then recombine and emit a single photon with a total energy equal to the bandgap energy plus the confinement energy of the electron and the hole (see section 2.4.2). The signal was collected by the same microscope objective used for the excitation (confocal setup) and analysed by a single (double) spectrometer featuring ∼30 μeV (∼15 μeV) spectral resolution, equipped with a Si-charge-coupled-device (CCD) camera cooled by liquid nitrogen. This detector has

good sensitivity at 800−900 nm. For emissions at longer wavelengths an InGaAs array was used. Figure 3.10(a) shows a diagram of the PL setup.

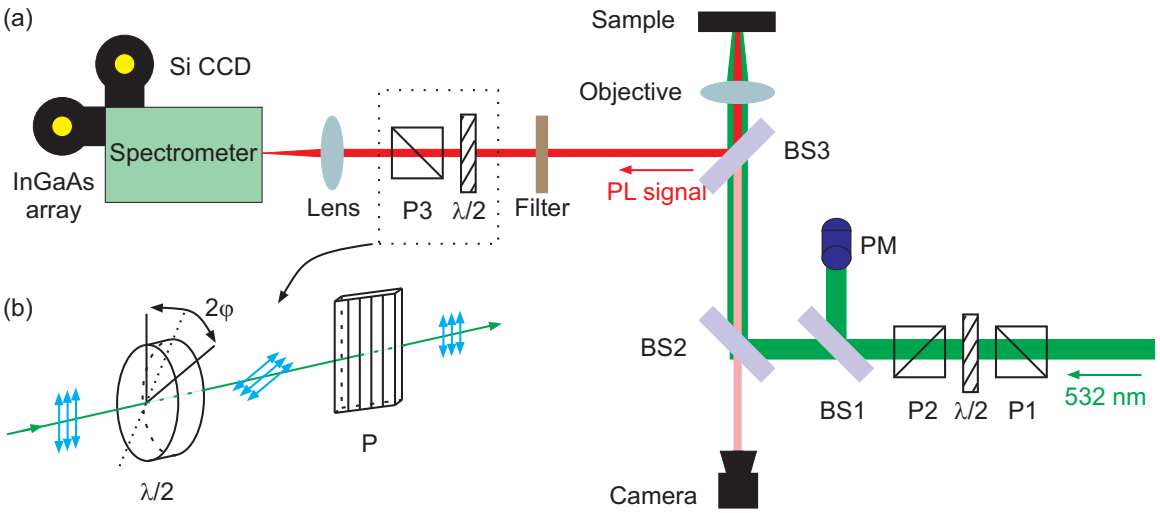

Figure 3.10.: Sketch of the (a) PL setup and (b) polarisation-resolved measurement.

The laser beam passes through a power attenuator consisting of a 532 nm monochromatic $\lambda/2$ waveplate, positioned between two polarisers P1 and P2. The first polariser cleans the polarisation of the incoming laser beam. By setting the angle of the $\lambda/2$ waveplate to a certain value the laser power can be controlled. A beamsplitter BS1 is used to branch off a small part of the laser beam towards a power meter (PM) and measure the effective excitation power on the sample (typically hundreds of nW). The laser beam is focused onto the sample by means of a 50× microscope objective (numerical aperture = 0.42) with a spot size of ∼1.0 μm. The objective is mounted on a single axis piezoelectric actuator in order to precisely focus the laser on the sample surface. The sample is positioned on the cold finger of a He-flow cryostat, which allows measurements to be performed at variable temperatures (300−4 K), and can be translated in the xy plane. The optical access to the cryostat is provided by a quartz window. BS2 protects the camera reducing the back-reflected light from the laser beam and allowing the visualisation of the sample. BS3 was chosen in such a way that the reflectivity was very high in the spectral region where the sample emits. A long pass filter, transparent for wavelengths above 690 nm, is used to suppress the excitation laser reflected by the sample, since the PL energy is significantly different from the excitation energy. Before focusing via a lens into the spectrometer, the degree of linear polarisation of the emitted light is analysed by inserting in the optical path a linear-polarisation-analyser [see Fig. 3.10(b)]. This is composed of a rotatable achromatic $\lambda/2$ wave plate electrically triggered and a fixed linear polariser (P3). The plane of the polarised light is rotated by 2ϕ and the polariser selects only photons with a polarisation parallel to the extraordinary axis, while those with orthogonal polarisation are rejected. The waveplate is mounted on a computer controlled rotation stage, which allows the rotation angle to be tuned with an accuracy of 0.1°. In some of the strain measurements performed in this work (see section 4.2) the excitation beam was superimposed with the light of a linearly polarised Ti:Sapphire laser, whose wavelength was tuned around 850 nm.

4. Results

In this chapter the main results obtained are discussed. The realisation of high optical quality, density and wavelength tunable GaAs/AlGaAs QDs for hybrid semiconductor atomic interfaces is demonstrated in section 4.1 (Refs. [146–148]). The second part focuses on InGaAs/GaAs QD-based devices, where both electric and strain fields are used to counteract the structural asymmetry of the dots and create entangled photon pairs by bringing the X states into degeneracy (section 4.2, Refs. [149–151]). Section 4.3 demonstrates the lateral control of InGaAs/GaAs QD pairs by overgrowing nanoholes with thin GaAs buffer layers (Refs. [152, 153]). Finally, the possibility to use a strain field to vary the coupling strength in a single vertical InGaAs/GaAs QDM is shown (section 4.4, Ref. [154]).

4.1. Novel GaAs/AlGaAs QDs for hybrid semiconductor-atomic interfaces

GaAs/AlGaAs QDs are strain free and attractive for applications in quantum cryptography and quantum computation. They can be created either by QW thickness fluctuations [155, 156], low temperature droplet epitaxy [132, 157, 158], or by infilling nanoholes created either by *ex situ* patterning [133, 159], in situ selective $AsBr_3$ etching [134, 160], or *in situ* droplet etching [146, 147, 161]. In contrast to InGaAs QDs, the larger lateral extent area of the exciton leads to higher emission probability [162] and shorter radiative lifetime [71].
Strain-free GaAs QDs have been used for the generation and manipulation of on-demand entangled photons by Ghali *et al.* [163]. Furthermore, a big step towards the realisation of a QD-based quantum memory and quantum repeater [164] was done by Akopian *et al.* [23] by using a hybrid atom-semiconductor QD. Here, when the GaAs/AlGaAs QD emission is tuned to the middle of the D_2 hyperfine absorption lines of ^{87}Rb, the velocity group of light is slowed down. Since only the emission within the 28 μeV spacing of the two D_2 lines is retarded, it is important to realise QDs with high optical quality and limited spectral diffusion and to control precisely the emission energy.

This section describes the optimisation of GaAs/AlGaAs QDs obtained by infilling self-assembled nanoholes fabricated by Ga-droplet etching of GaAs (001) substrates. It is demonstrated control over the dot density to very low values by varying the Ga flux used to create the nanoholes, and independent control over the dot emission energy. Narrow excitonic emission lines as sharp as 3.8 μeV are shown with ensemble homogeneity better than 11 meV. A tuning range larger than 10.5 meV is obtained by applying anisotropic biaxial strain of the order of 0.15%.

4.1.1. Nanoholes and GaAs/AlGaAs QDs formation

GaAs/AlGaAs QDs were obtained by infilling nanoholes created by droplet etching. After a thick GaAs buffer growth, several MLs of gallium were deposited at a rate between 0.05 and 1 ML/s at T_{sub} = 520°C. The arsenic was repeatedly pulsed [165] or closed whilst gallium was continuously supplied to the substrate. The substrate was then annealed for 300 s under an As flux [166]. The change of the surface reconstruction from As rich (2×4) to Ga rich (4×2), during excess gallium deposition, together with the appearance of spots in the RHEED pattern indicated the formation of Ga droplets [167]. These spots fade, eventually disappearing, as the droplets etch into the substrate.

Fig. 4.1(a) shows AFM images of nanoholes fabricated using 3 ML of gallium deposited at different rates.

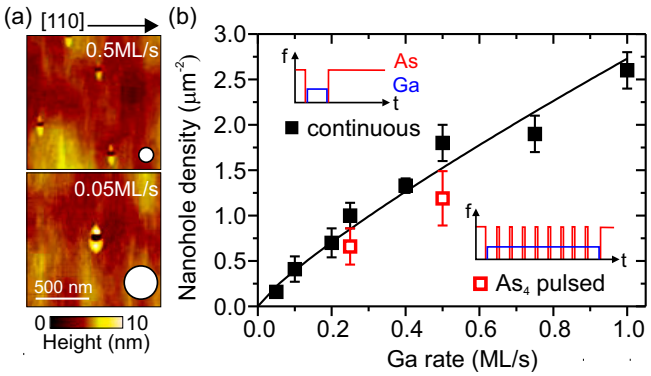

Figure 4.1.: (a) AFM images of nanoholes fabricated using 3 ML Ga at different rates. The white circles depict the calculated initial Ga droplet size. (b) Nanohole density as a function of the Ga rate, for 3 ML excess Ga deposited continuously (black solid symbols, error bars indicating density variation across a single sample), or for ∼4 ML excess Ga with As_4 supplied pulsed (red open symbols, error bars indicate the density spread over >10 samples). The solid line is the fit of the measured data. Figure readapted from Ref. [146].

The nanoholes are elongated along the [110] direction, surrounded by elevated GaAs mounds elongated along the [1-10] direction. The nanohole density after 3 ML excess Ga deposition can be varied nearly linearly in the range $(0.2 - 2.5)\times10^8$ cm^{-2} [solid symbols in Fig. 4.1(b)] by changing the Ga rate. The solid curve corresponds to a fit obtained from conventional nucleation theory [168], $n \propto F^{i^*/(i^*+2.5)}$, which relates density with flux and implies a critical nucleus size i^* ∼13 atoms at T_{sub} = 520°C. The nanohole density for a given Ga rate is slightly reduced by pulsing the As supply [open symbols in Fig. 4.1(b)] but both the pulsed and the continuous deposition methods create nanoholes with very similar size and shape. The droplet size can be increased either by decreasing the Ga deposition rate or by increasing the Ga deposition amount. However, the hole depth and width eventually saturate at some value, due to droplet recrystallisation, which limits the amount of droplet etching that can occur. The average droplet radius can be estimated from simple considerations once the nanohole density is known [152], as shown by the white circles in Fig. 4.1(a). The magnitude of

the hole depth, width and mounds is much smaller than that of the original droplet. This implies that the majority of the droplet spreads out and recrystallises on the planar regions between the nanoholes during the annealing stage, as observed by arsenic RHEED oscillations [169].

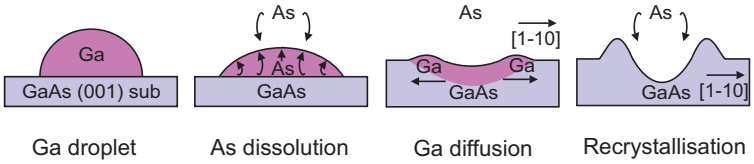

Figure 4.2.: Sketch of the different stages during the Ga droplet etching of GaAs (001) substrate. Figure readapted from Ref. [153].

The etching occurs via As dissolution of the GaAs substrate under the gallium droplet, driven by the concentration gradient at the interface [170]. The rate of dissolution is higher in the [110] direction, leading to the observed elongation of the holes. This is due to the greater reactivity of As atoms in the presence of an oxidising agent [171], and to the different As bonding configuration of the A-type (parallel to the [1-10] direction) and B-type (parallel to the [110] direction) facets [172]. Moreover, Ga diffusion is faster along the [1-10] direction compared to the [110] direction at this T_{sub} [173]. At the same time an excess As flux is being supplied onto the GaAs surface, which can start to recrystallise the excess Ga [174]. The resulting nanohole size is the result of the competition between the dissolution, diffusion and recrystallisation processes until all the excess gallium has been converted to GaAs, as sketched in Fig. 4.2. A similar etching procedure was performed at $T_{sub} = 500°C$ to control the nucleation of InGaAs/GaAs QD pairs (see section 4.3).

The GaAs/AlGaAs formation is described in Figs. 4.3(a) and 4.3(b).

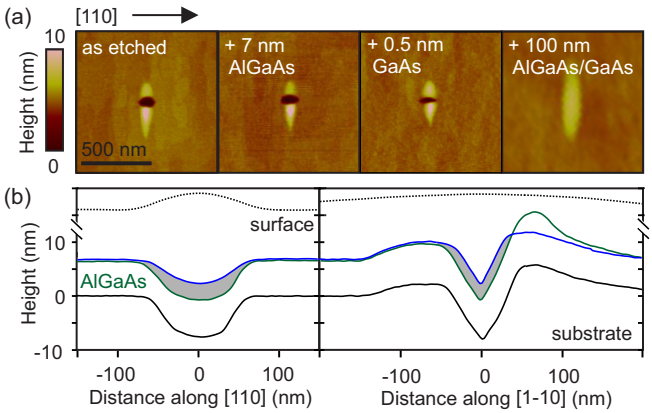

Figure 4.3.: (a) AFM images (1 μm $\times$ 1 μm) of a nanohole at different stages of QD growth. (b) Average AFM linescans (average of over 10 holes) showing the nanohole profile: as-etched (black), after overgrowth of 7 nm $Al_{0.45}Ga_{0.55}As$ (green), 0.5 nm GaAs (blue), and after capping by 80 nm $Al_{0.37}Ga_{0.63}As$ and 20 nm GaAs (black dotted). The shaded region shows the volume of a nominally 0.5 nm GaAs QD. Figure readapted from Ref. [146] (AFM data taken by P. Atkinson).

After the etching of the nanohole, a 7 nm $Al_{0.45}Ga_{0.55}As$ barrier was grown. The hole shape is unchanged by the growth of the bottom AlGaAs barrier, due to the short migration length of Al on the surface [175]. However, after only 0.5 nm GaAs deposition (rate of 0.25 ML/s) followed by a 2 minutes growth interrupt, to allow GaAs migration towards the bottom of the nanoholes, there is a clear change in the hole profile. The hole has significantly infilled and has narrowed in the [1-10] direction, due to the higher sticking coefficient of Ga on the B-type (As-terminated) step edges on the sidewalls parallel to the [110] direction. The inverted GaAs/AlGaAs QD, which is thus formed in the nanohole, was capped with 80 nm $Al_{0.37}Ga_{0.63}As$ and 20 nm GaAs. After this capping, the dot location is still visible by a 2-nm-high mound with width in the [110] direction similar to the original nanohole width. The shaded area in Fig. 4.3(b) shows the QD volume.

4.1.2. Optical quality and wavelength tuning

Using the setup reported in section 3.5, bright QD emission spectrally well separated from the QW luminescence (0.21 eV for 1 nm GaAs filling) can be observed [see Fig. 4.4(a)]. Some interface fluctuation QDs can also be seen in the low energy tail of the QW.

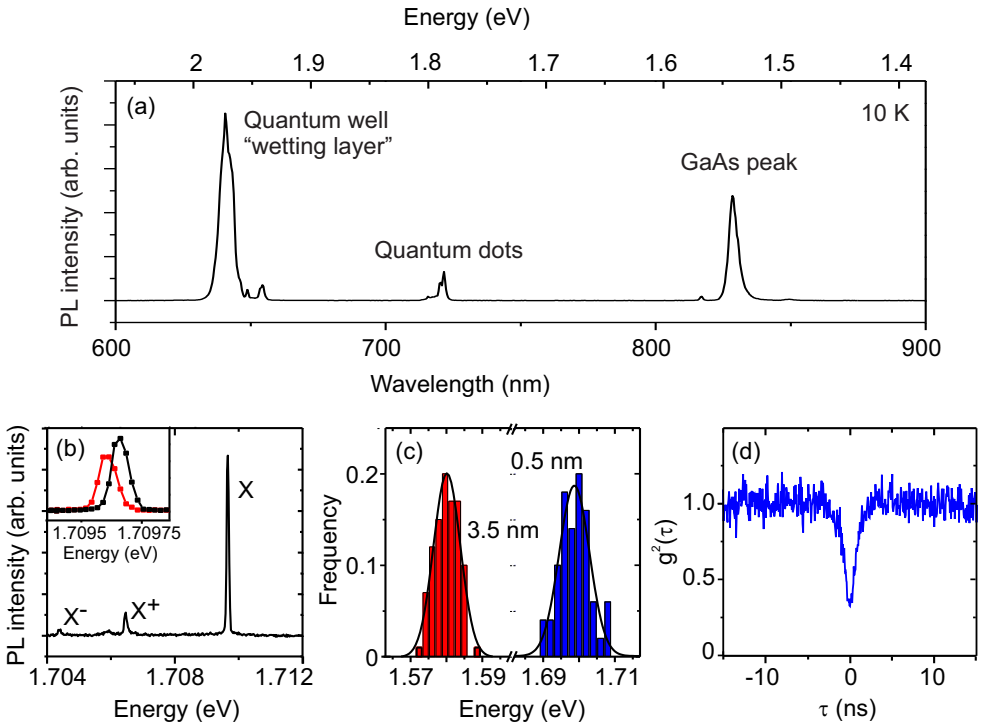

Figure 4.4.: (a) Ensemble PL of a nominally 1-nm-thick GaAs/AlGaAs QD. (b) Single-dot spectrum showing neutral and charged exciton lines. The inset shows orthogonally polarised X emission. (c) Frequency histograms of X energy of 100 (50) dots nominally 3.5 nm (0.5 nm) thick. (d) Normalised second-order correlation function $g^{(2)}(\tau)$ for X emission of a single GaAs/AlGaAs QD nominally 3 nm thick under non-resonant continuous wave excitation. Figures (a-c) from Ref. [146] and (d) from Ref. [147].

The optical quality of the single QDs located in the holes is investigated by μ-PL, as shown in Fig. 4.4(b). The dominant species at low excitation intensity is the X, as identified from its polarisation dependence with a FSS of 50 μeV [see the inset of Fig. 4.4(b)]. The charged excitons are weakly seen on the majority of dots and assigned following the calculations by Wang *et al.* [160]. The FSS varied from 20 μeV to 100 μeV with a tendency to lower FSS for taller dots, in agreement with other reports on dots grown by infilling similarly asymmetric nanoholes [176,177]. Fig. 4.4(c) shows the energy distribution of QD ensembles with nominally 3.5 nm and 0.5 nm infilling. The ensemble full width at half maximum (FWHM) is 9 meV (10 meV) for the lower (higher) energy ensemble. These values are four times narrower than that obtained for ensembles of self-assembled SK grown InAs/GaAs QDs, and three times wider than the narrowest QD ensemble reported, obtained by growing InGaAs/GaAs QDs in *ex situ* patterned nanoholes on (111)B GaAs substrates [178].
By equating the dot emission with the calculated emission of a QW with the same thickness as the dot height [the smallest dimension as can be seen in Fig. 4.3(a)], the energy spread can be converted into a spread of dot heights. The nominal 3.5 nm QW leads to dots (8.3 $\pm$ 0.7) nm high and the 0.5 nm QW yields dots of height (3.7 $\pm$ 0.2) nm. Since the depth of the original nanoholes is $\sim$8 nm [see Fig. 4.3(b)], the nominally 3.5 nm QDs correspond to the nanoholes that are completely infilled with GaAs. Therefore, in this case the height variation of the QDs reflects the spread in depths of the original nanoholes. The nominally 0.5 nm QDs correspond to the nanoholes only half-filled and the spread in dot height is only $\pm$1 ML, similar to the QW thickness fluctuation.

To demonstrate single-photon emission [179] from these QDs, photon correlation measurements [180] with Hanbury Brown and Twiss (HBT) setup were performed. A 50:50 non polarising beam splitter and two high efficiency single photon counting avalanche photodiodes (APDs) are used. The APDs were connected to the start and stop inputs of a time correlated single photon counting module (Pico-harp 300, PicoQuant GmbH) to yield the number of photon pairs as a function of the arrival time separation $\tau = t_{stop} - t_{start}$. This is proportional to the normalised second-order correlation function of exciton emission of a single QD, $g^{(2)}(\tau) = <I(t)I(t+\tau)>/<I(t)>^2$, where I are the light intensities incident on the respective detectors, as shown in Fig. 4.4(d) under non-resonant continuous wave excitation. The value at zero delay of 0.3 clearly indicates single photon emission from the QD and is limited by the finite time-resolution of the experimental setup.

In order to tune the QD emission to 780 nm [23], in resonance with the middle of the D_2 hyperfine absorption lines of ^{87}Rb, the effect of Ga deposition amount on the QD emission energy was investigated, as shown in Fig. 4.5(a). A wide range of 200 meV energy shift can be obtained by varying the GaAs filling from 0.25 nm to 3 nm. The PL of QD ensembles with different nominal GaAs thicknesses is obtained by summing μ-PL spectra taken at different points.
The dot emission energy [solid symbols in Fig. 4.5(b)] can be approximated by comparing it with the emission energy of a QW of equivalent thickness [open symbols in Fig. 4.5(b)]. It can be seen that the height of the dot is much greater than the nominal thickness of GaAs deposited, and that the rate of change in height slows down as more

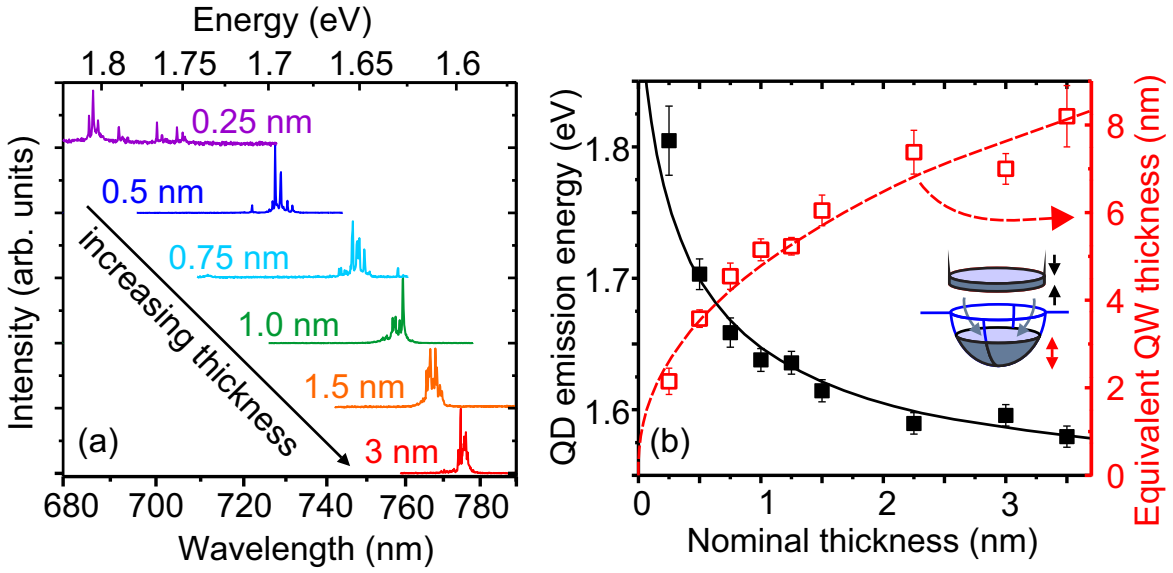

Figure 4.5.: (a) PL of GaAs/AlGaAs QD ensembles with different nominal GaAs thicknesses, spectra offset vertically for clarity. (b) Graph showing the QD emission energy (solid symbols) and the calculated QW thickness, where the QW has the same emission energy as the QD (open symbols), as a function of the nominal GaAs thickness. Figure from Ref. [146] (modelling from P. Atkinson).

GaAs is deposited, in good agreement with the AFM observations. The change in dot height with GaAs amount has been modelled by treating the nanohole as an ellipsoidal volume, with major and minor axes given by the [110] and [1-10] linescans of the initial hole shape, as depicted by the schematic diagram in Fig. 4.5(b). Assuming that all the GaAs deposited on the hole ends up at the hole bottom, the resulting volume is equated with the GaAs deposited over the hole. Once the hole is completely infilled, the rate of change of QD height reverts to the growth rate. The result is shown by the red dotted curve and converted to the energy of a QW of the same thickness as the QD height to give the black curve in Fig. 4.5(b). In this way, the infilling of the nanohole and subsequent dot emission energy can be well predicted if the shape of the original hole is known, without the need to make any assumptions about net migration towards the bottom of the hole.

GaAs/AlGaAs QDs with high optical quality, limited ensemble inhomogeneous broadening and density and wavelength tuneable in a wide range have been demonstrated. However, due to the size fluctuations of individual QDs, a more precise control over the emission energy is required for the hybrid semiconductor-atomic interfaces experiment [23]. This is realised by applying, for example, an external magnetic field parallel to the growth direction (Faraday configuration). Figure 4.6(a) shows the emission of a nominally 3-nm-thick GaAs/AlGaAs QD, where a cell with rubidium vapour at 81°C was placed in front of the detector. This picture was taken in collaboration with the group of Prof. V. Zwiller in Delft. The dashed lines correspond to the ^{87}Rb D_2 transitions. The long wavelength branch of the Zeeman-split emission, marked by solid white lines, is tuned through the D_2 transitions and is partially absorbed by the vapour when

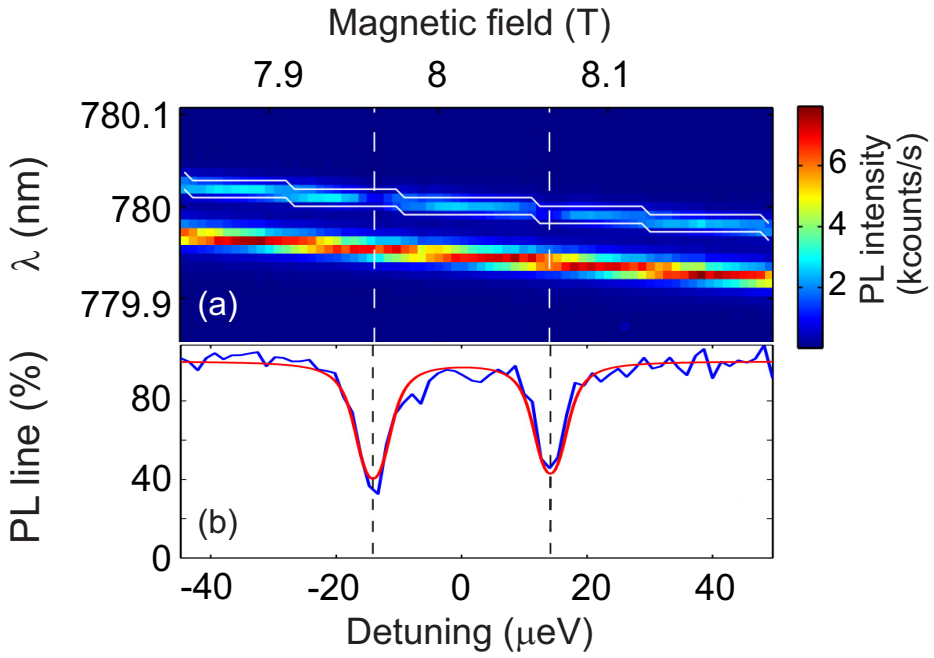

Figure 4.6.: (a) PL spectra of a QD exciton under increasing magnetic field. A cell with a rubidium vapour at 81°C was placed in front of the detector. Dashed lines correspond to the ^{87}Rb D_2 transitions. (b) Transmission of the long wavelength PL branch of the Zeeman-split X emission through the rubidium vapour: experimental data (blue) and fit (red). Figure readapted from Ref. [148].

in resonance, as shown by the transmission of the PL line with two well-resolved dips that correspond to the D_2 hyperfine structure [see Fig. 4.6(b)]. The fit reveals very narrow emission linewidth with FWHM of (3.8 ± 0.3) μeV [148]. This value defines the droplet GaAs/AlGaAs QDs obtained as the best reported in literature so far. The higher quality of the QDs, compared to those used in the work of Akopian *et al.* [23], is probably due to *in situ* etching of nanoholes by excess Ga introducing fewer defects into the GaAs surface than *in situ* etching by $AsBr_3$ [134].

For a better efficiency of the tuning technique, all the QDs of the ensemble should be brought into resonance with the Rb vapour. This is not possible using a magnetic field, due to the limited tunability range of (0.5 − 1) meV over 8 T. To achieve a larger tuning range, an on-chip tuning technique was adopted, taking advantage of the strain field induced in a nanomembrane by an underlying PMN-PT substrate (see section 3.3). Similar GaAs/AlGaAs QDs nominally 3 nm thick were grown separated from the substrate by an additional sacrificial $Al_{0.75}Ga_{0.25}As$ layer and a buffer layer, and the device was fabricated as explained in section 3.4. In this case, the sample was transferred onto the PMN-PT via a commercial glue (Cyanoacrylate).
The evolution of the PL spectrum of a few QDs as a function of the electric field F applied to the piezoelectric actuator, i.e., of the average in-plane strain $\bar{\varepsilon}_{//} = (\bar{\varepsilon}_{xx} + \bar{\varepsilon}_{yy})/2$ (see section 2.3), is shown in Fig. 4.7. To generate spectral maps, PL spectra are sequentially accumulated at various values of F and then assembled to plot PL intensities as a function of both energy/wavelength (x-axis) and $F/\bar{\varepsilon}_{//}$ (y-axis).

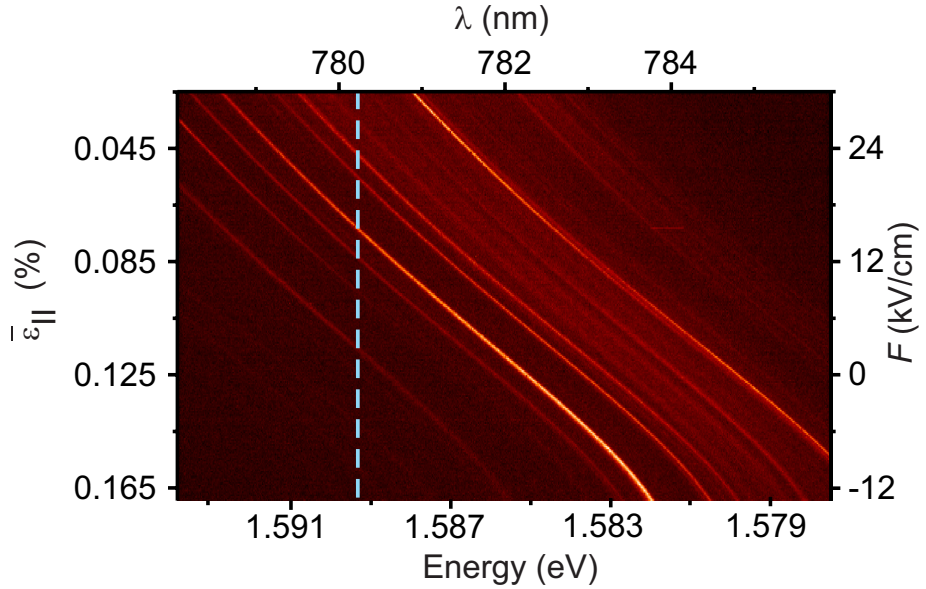

Figure 4.7.: Colour-coded μ-PL intensity map of the emission wavelengths of a few QDs as a function of average in-plane strain $\bar{\varepsilon}_{//}$. The vertical dashed line highlights the mean wavelength of the ^{87}Rb D_2 transitions. Figure readapted from Ref. [147].

As expected from previous studies [77, 85, 143], a compressive (tensile) biaxial strain results in an blueshift (redshift) of the QD emission energy, which is ascribed mainly to the change of the energy bandgap of the dot region (i.e., GaAs). Anisotropic in-plane strains inside the GaAs crystal lead to the mixing of LH and HH bands (see section 2.3), so that the two strain-split emissions originate from excitons involving holes from two mixed bands of LH and HH character. Moreover, the transfer process and the cooling step produce a pre-strain, which is important for quantifying the total amount of strain induced in the membrane [147]. A total tuning range of 10.5 meV ($\Delta\lambda = 5.2$ nm), which corresponds to a strain variation of 0.15%, is demonstrated. Since the ensemble emission linewidth is 11 meV and is centered at 778.5 nm, the available tuning range is sufficient to bring the emission wavelength of the majority of the QDs from the sample in coincidence with the middle of the ^{87}Rb D_2 lines [shown by a dashed line in Fig. 4.7].

In conclusion, high quality GaAs/AlGaAs QDs with linewidth down to 3.8 μeV, density $\sim (0.2 - 2.5)\times 10^8$ cm^{-2} and wavelength tuneable over a wide range of 200 meV by varying the Ga amount deposited in the nanoholes have been demonstrated. A fine tuning to the ^{87}Rb D_2 lines is obtained by means of magnetic and strain fields. The latter on-chip tuning technique permits the QD emission energy to be controllably varied over a spectral range exceeding 10 meV, comparable to the ensemble inhomogeneous broadening, increasing the yield of single photons which could be slowed down via a hybrid semiconductor-atomic interface.

4.2. InGaAs/GaAs QDs tuned for entanglement

The possibility to realise solid-state triggered entangled photon sources for quantum cryptography and quantum computation via the radiative decay of the XX to the crystal ground state was highlighted for the first time in year 2000 by Benson *et al.* (see section 2.4.2 for details). However, the exploitation of QDs in quantum networks [181], where the precise control over the emission properties is a fundamental requirement [164], is frustrated by the fluctuations in QD size, shape, strain and composition [6,13]. In particular, when the FSS (see section 2.4.2) is larger than the radiative linewidth of the transitions (of the order of 1 μeV), the fidelity of the entangled photon pairs is strongly reduced [14, 21, 22, 182].
Despite impressive progress in the fabrication of highly symmetric QDs [183] and in the post-growth control of their optical properties via external perturbations [22, 76–78, 80, 86], it remains extremely difficult to systematically drive the FSS to zero, mainly due to the coherent coupling of the two bright exciton states [46,68,71,80,86,184]. As a result, the high degree of entanglement needed for the implementation of QDs in real applications and in advanced quantum optics experiments [185] has been achieved only by few groups worldwide, by cherry-picking the very rare QDs featuring FSS ≈ 0 [8,22,186,187] or by using temporal [21] and spectral filtering [8, 22] techniques, which inevitably reduce the brightness of the source.

In this section, first a device design allowing the simultaneous combination of electric and strain fields on single InGaAs/GaAs QDs will be demonstrated. The separate effects produced by the two external perturbations on the relative binding energy of the excitonic complexes confined in the same QD are investigated. Then, independent control of the emission energies of two excitonic species, in particular of the X and XX, will be shown. Most importantly, via these two "knobs" it will be demonstrated that it is always possible to drive the excitons confined in arbitrary QDs towards a universal level crossing. Finally, the fact that virtually any QD embedded in these devices can be used for the generation of highly polarisation-entangled photons will be demonstrated with the highest degree of entanglement ever reported for QD-based entanglement resources.

4.2.1. Sample description

The sample was grown by solid source MBE (see section 3.1) on a semi-insulating GaAs (001) substrate and consists of a layer of InGaAs QDs embedded in the intrinsic region of a n-i-p diode. Following oxide desorption, a 300-nm-thick undoped GaAs buffer layer was grown at $T_{sub} = 570$°C. A 100-nm-thick sacrificial layer of $Al_{0.75}Ga_{0.25}As$ was deposited, followed by a 150-nm-thick n-doped (Si at 5×10^{18} cm^{-3}) GaAs layer, a 30-nm-thick n-doped (Si at 5×10^{18} cm^{-3}) $Al_{0.4}Ga_{0.6}As$ layer, a 70-nm-thick intrinsic $Al_{0.4}Ga_{0.6}As$ layer and a 10-nm-thick GaAs intrinsic layer containing in the centre a layer with low density InGaAs QDs. At the beginning of the n-doped GaAs layer, a δ-doping layer (Si at 1.2×10^{13} cm^{-2}) was introduced for a non-annealed n-type ohmic contact [188] in the subsequent device processing. The growth was completed with a 70-nm-thick intrinsic $Al_{0.4}Ga_{0.6}As$ layer, a 30-nm-thick p-doped (C at 5×10^{18} cm^{-3})

$Al_{0.4}Ga_{0.6}As$ layer, and a 71.5-nm-thick p-doped (C at 5×10^{18} cm^{-3}) GaAs layer with higher doping for the last 6 nm (C at 1×10^{19} cm^{-3}) in order to ensure a good ohmic contact. The GaAs/AlGaAs QW reduces carrier escape at high electric fields (F_d up to ∼250 kV/cm) across the diode (see section 2.4.3 for details).
The thickness of the nanomembrane and the position of the QD layer were optimised for the formation of a simple metal-semiconductor planar cavity [145]. The width of the cavity was chosen as 1.67λ from the standing wave conditions, where λ is the emission wavelength of the QD. This corresponds to a nanomembrane ∼430 nm thick for $\lambda = 890$ nm, considering the refraction indexes of GaAs and AlGaAs. The QDs were positioned at 1λ from the sacrificial layer, in order to maximise the coupling strength between emission source and respective mode intensity, i.e., the dipole emitter has to be located at the antinode of a standing wave.
The layer of InGaAs QDs was grown at 500°C. The QD height was controlled by the *indium flush* growth method (see section 3.1.1). The dots were capped with thin GaAs layers (2.5 nm) at the same temperature and then annealed at 570°C for 180 s, in order to remove the InAs from the exposed portion of the pyramids. The sample was rotated during the growth and the low density of InGaAs/GaAs QDs was obtained by taking advantage of the temperature gradient across the wafer during growth, as shown in the position-dependent PL map measured by moving the laser from the centre to the edge of the 2-inch sample (see Fig. 4.8).

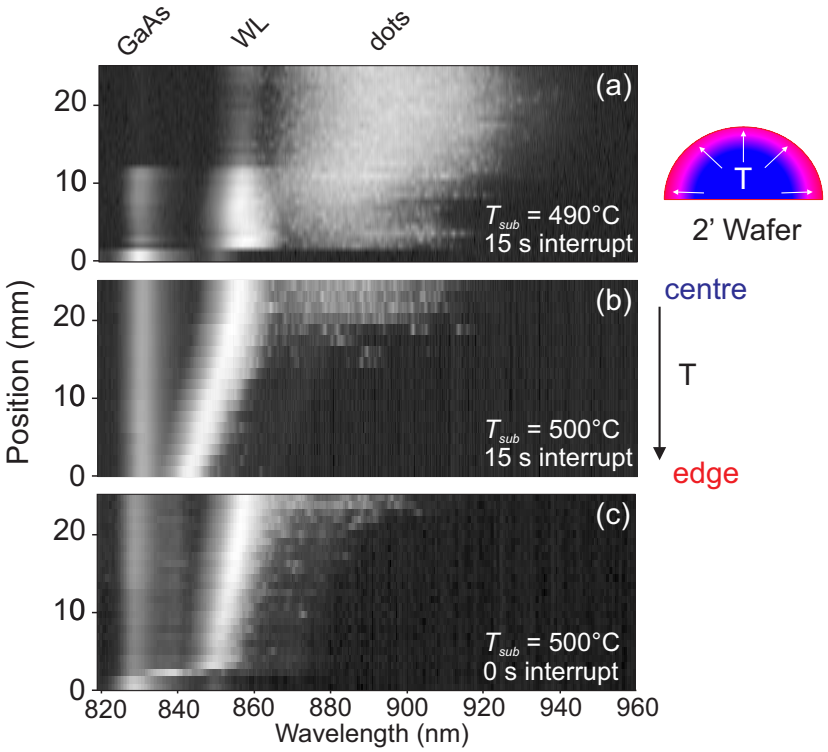

Figure 4.8.: Position-dependent PL map (from centre to edge of the sample) of InGaAs/GaAs QDs after 1.8 ML of InAs at T_{sub} = (a) 490°C, (b) 500°C, (c) 500°C followed by 15 s, 15 s, 0 s growth interrupt, respectively.

Three peaks are mainly visible: the GaAs peak ∼820 nm, the InAs WL and the wider

peak from the QD ensemble. When InAs over θ_{crit} is deposited at $T_{sub} = 490°C$ followed by 15 s growth interrupt [see Fig. 4.8(a)], almost no shift of the lines together with a constant dot density are measured along the sample. At $T_{sub} = 500°C$, there is a blueshift of the WL due to the Ga-In intermixing [131] and to the In desorption at this temperature [189], together with a reduction of the dot density towards the edge of the sample, as shown in Figs. 4.8(b) and 4.8(c). The precise sequence adopted for the work described in this section was InAs deposition at $T_{sub} = 500°C$ without growth interruption [see Fig. 4.8(c)], resulting in a smaller blueshift of the InAs WL and low density of dots up to the edge of the sample.

4.2.2. Independent control of exciton and biexciton energies

The n-i-p diodes/membranes containing InGaAs QDs are integrated onto PMN-PT by gold-thermocompression bonding, as described in section 3.4. A sketch of the device is shown in Fig. 4.9(a).

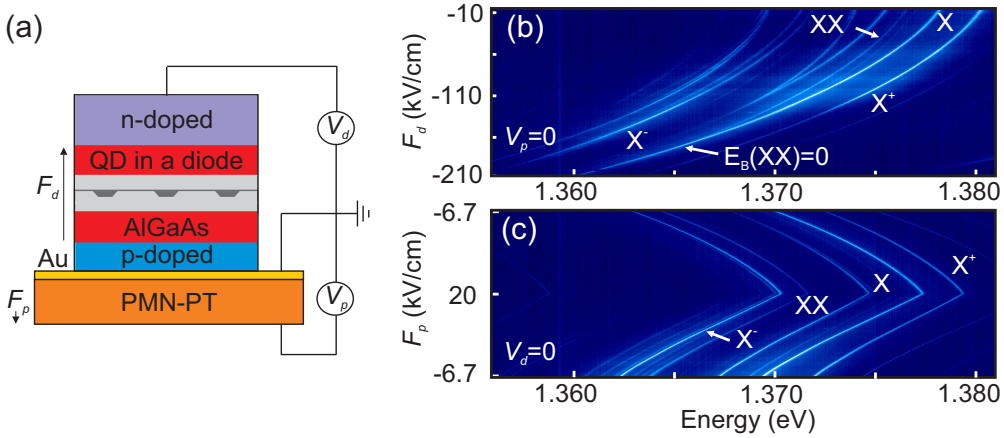

Figure 4.9.: (a) Sketch of the dual-knob device where membrane diodes are integrated on top of PMN-PT. (b,c) Colour-coded μ-PL maps of a single InGaAs/GaAs QD embedded in the device (b) as a function of the electric field across the QD (F_d) with $V_p = 0$ and (c) as a function of the electric field across the PMN-PT (F_p) with $V_d = 0$. A logarithmic scale is used for the intensity. Positive (negative) electric fields F_p correspond to in-plane compressive (tensile) stress. Figure readapted from Ref. [150] (PL data taken by R. Trotta).

The device provides two independent external perturbations (F_d and F_p) for engineering the energy levels of the quantum emitters on demand by applying, respectively, the voltages V_d and V_p. They usually vary in the ranges -350 V $< V_p <$ 900 V and -1.9 V $< V_d <$ 2 V. The electric field values are obtained from the relation $F_d = (V_{bi} - V_d)/L$, where $L = 150$ nm is the thickness of the intrinsic layer.
The typical spectrum of a single QD at $V_p = V_d = 0$ V is similar to the one reported in Fig. 2.7 with the four emission lines such as X, XX, X^- and X^+. In this case the QDs were excited with an 850 nm continuous wave laser (see section 3.5 for the PL setup). The trions X^- and X^+ were recognised by the absence of FSS and by investigating their energy shifts under application of stress. In fact, X^+ shifts similarly

to the XX whereas X^- follows a different law. The assignment was also confirmed by embedding the same type of QDs in charge tunable devices [n-i-Schottky diodes, in the same configuration displayed in Fig. 4.9(a)], where the appearance of the different complexes with increasing V_d identifies unambiguously their origin [11]. As shown in Fig. 4.9(b), large shift of the emission lines is obtained by applying V_d (F_d) to the n-doped side of the diode, due to the QCSE [81]. In this way, the energy separation between X and XX, which will be referred to as the relative biexciton binding energy $E_B(XX) = E_X - E_{XX}$, can be brought into energy coincidence even when their initial E_B is as large as 2 meV.
Simultaneously, anisotropic in-plane (compressive or tensile) biaxial strains $\varepsilon_{//}$ is induced in the QD layer by applying V_p (F_p) to the PMN-PT. Figure 4.9(c) shows the resulting reversible line shifts. The in-plane strain transferred to the GaAs nanomembranes varies by about 0.3−0.4%, when V_p is swept through the whole tuning range [145]. When the two fields are used to shift the emission in the same direction the QD emission lines can be shifted up to 30 meV and ∼3 meV tunability of E_B. Since the average value for $|E_B\ (XX)|$ over 35 QDs at $V_d = V_p = 0$ V is 1.43 meV, the device allows X-XX colour coincidence to be achieved in almost all the QDs in the ensemble.

Figures 4.9(b) and 4.9(c) show also that X, XX, X^- and X^+ shift at different rates with the two fields. In order to explain how the relative binding energies of the excitonic complexes react when different external fields are applied, it is important to start considering the system at $V_d = V_p = 0$ V. This is shown in Fig. 4.10(a) for four different QDs embedded in the device.
It is clear that the X^+ (X^-) is always on the high- (low-) energy side of the X. The absolute value of the relative binding energy of the X^- is usually larger than that of the X^+ and of the order of a few meV. This is due to the different direct Coulomb integrals (C_{ij}) between electrons ($i, j = e$) and holes ($i, j = h$) confined in this type of QDs, as already explained in section 2.4.2 (see the relation 2.31). Furthermore, the relative binding energy of the XX can be either positive or negative and does not show any correlation with the energy of the X transition [13].

Figures 4.10(b)-(d) show the relative binding energies of the excitonic species for a specific QD when the voltages are varied. A quadratic (linear) change with the magnitude of the electric (strain) field is observed, while they always display a linear behaviour when plotted against the exciton emission energy (E_X). The rate of change is given by $\gamma = \Delta E_B/\Delta E_X$ with $\bar{\gamma}$ the average value. By analysing different QDs embedded in different devices, it is found that strain (S) and electric (F) fields affect E_B of different excitonic complexes in a different manner, since $(\bar{\gamma})^F > (\bar{\gamma})^S$, $(\bar{\gamma}_{XX})^S \sim (\bar{\gamma}_{X^+})^S > (\bar{\gamma}_{X^-})^S$ and $(\bar{\gamma}_{XX})^F > (\bar{\gamma}_{X^-})^F > (\bar{\gamma}_{X^+})^F$, as shown in the insets of Figs. 4.10(b)-(d). Then, it is clear that there is a field-dependent modification of the interaction energies among electrons and holes confined into the same QDs.
Considering only direct Coulomb interactions, from the relation 2.31 (see section 2.4.2) the following variations of the relative binding energies are obtained:

$$\Delta E_B(X^-) = -\Delta C_{ee} + \Delta|C_{eh}|, \tag{4.1a}$$

$$\Delta E_B(X^+) = -\Delta C_{hh} + \Delta|C_{eh}|, \tag{4.1b}$$

$$\Delta E_B(XX) = \Delta E_B(X^+) + \Delta E_B(X^-). \tag{4.1c}$$

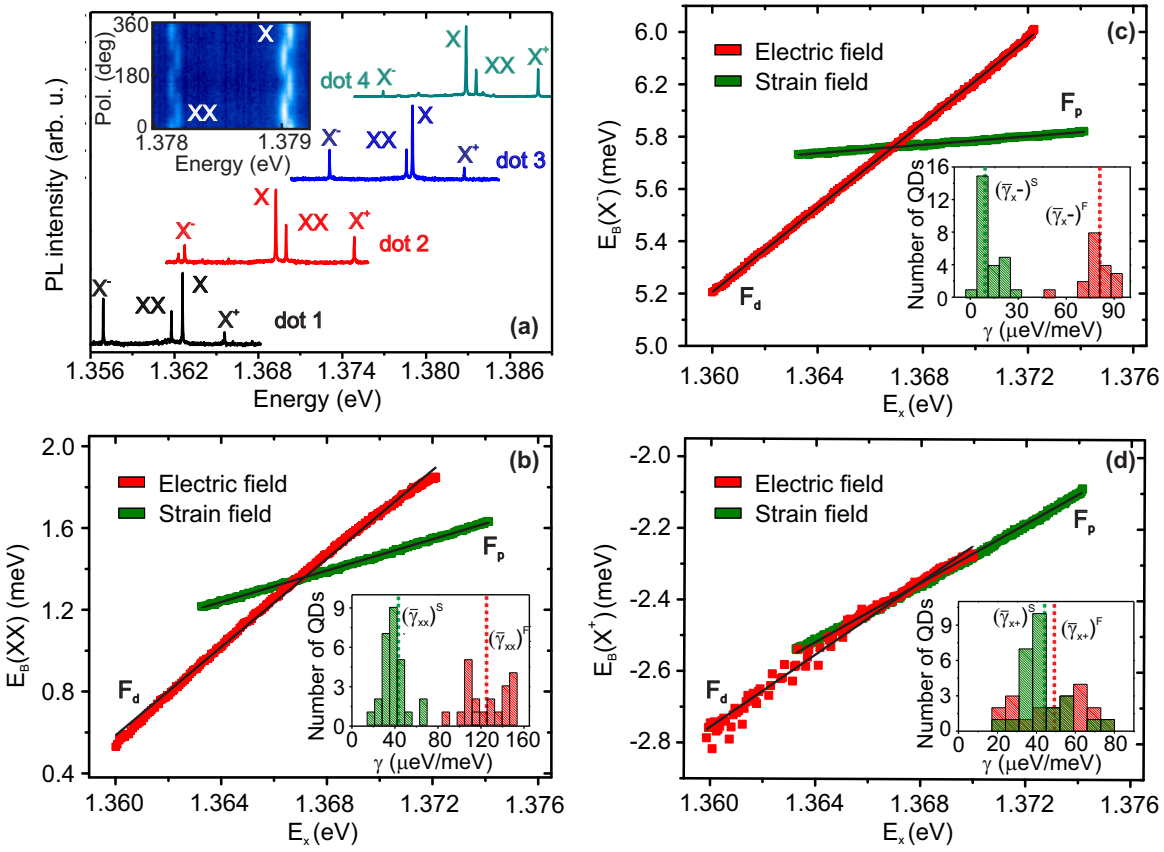

Figure 4.10.: (a) μ-PL spectra of four InGaAs/GaAs QDs at $V_p = V_d = 0$ V. In the inset, a typical polarisation resolved μ-PL map of X and XX is displayed. (b)-(d) Relative binding energies (E_B) of the (b) XX, (c) X^- and (d) X^+ as a function of the energy of the exciton transition (E_X) for a single QD. Red (green) squares refer to the data obtained when F_d (F_p) is varied at $F_p = 0$ ($F_d = 0$). Black lines are linear fits to the experimental data. In the inset of each panel, a histogram of γ for all the measured QDs, which represents the field-induced changes of the E_B normalised by the change in E_X, is also reported. The dashed lines indicate the averaged values. Figure from Ref. [150].

Equation 4.1(c) is reproduced qualitatively by the experiment, where $\bar{\gamma}_{XX} \sim \bar{\gamma}_{X^-} + \bar{\gamma}_{X^+}$. Concerning the trion transitions, by subtracting equations 4.1(a) and 4.1(b), the quantity $\delta = \Delta C_{hh} - \Delta C_{ee}$ can be analysed. It is found that δ has a different sign when strain or electric fields are applied to the same QD. In particular, when the X emission energy is blue-shifted, $(\Delta C_{ee})^F < (\Delta C_{hh})^F$ and $(\Delta C_{ee})^S > (\Delta C_{hh})^S$. This can be explained as both fields have a larger effect on the absolute value of the Coulomb integrals between electrons than between holes, due to the increased confinement potential of electrons by in-plane compressive biaxial strain [143] and increased vicinity of electrons by electric field. However, the change in electron-electron repulsion under strain and electric field have opposite signs because ΔC_{ee} is negative for increasing E_X.

The two external perturbations can also work "against" each other, in the so-called "subtractive mode", as shown in Fig. 4.11.

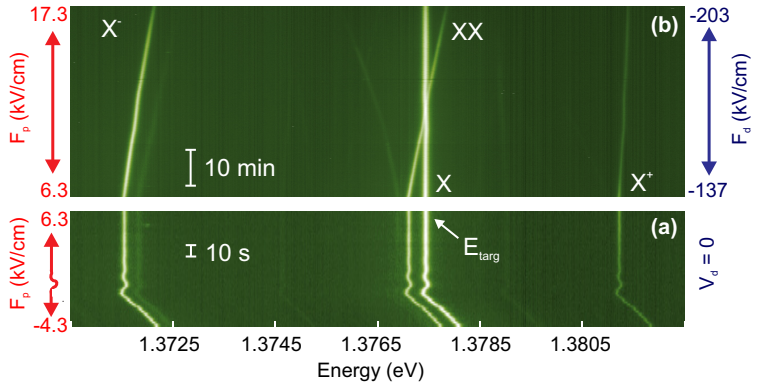

Figure 4.11.: (a) Colour-coded μ-PL map of a single InGaAs/GaAs QD. (a) The X is first tuned to the target energy of $E_{targ} = 1.3774$ eV and then locked at this value via a computer-controlled active feedback on F_p. During the experiment, $V_d = 0$ V. (b) Then, the magnitude of F_d is ramped up while the exciton transition is locked at E_{targ} via F_p, as explained in the main text. Figure from Ref. [150].

First strain is used via a computer-controlled voltage V_p to shift and frequency-lock, with meV precision [145], the X transition to a user-defined target energy (E_{targ}) [see Fig. 4.11(a)]. The time evolution of the μ-PL signal of a QD is shown as the applied fields are varied. Because of fast feedback parameters, some oscillations can be noticed in the time-trace before E_x finally reaches a stable value. Then, V_d is changed linearly to increase the magnitude of F_d while the X is kept fixed at E_{targ} via increasingly compressive strain, as shown in Fig. 4.11(b). In this way, instead of a quantum confined Stark shift of all the emission lines, here only the spectral position of the other excitonic complexes is changed without affecting the energy of the X. This is due to the different values of $(\gamma)^F$ and $(\gamma)^S$, which are a direct consequence of the different effects strain and electric field have on the electron and hole wavefunctions. Assuming that $(\gamma)^S$ and $(\gamma)^F$ do not depend appreciably on the value of F_d and F_p, respectively, it is observed that under the simultaneous application of strain and electric field the trions and biexciton energies shift at a rate $(dE/dt)^{F-S} = [(\gamma)^F - (\gamma)^S] \cdot (dE_X/dt)^S$, being $(dE_X/dt)^S = -(dE_X/dt)^F$ ($\sim$3 μeV/s in the experiment). Remarkably, the XX changes gradually from a binding to an antibinding configuration for a fixed and predefined exciton energy

(E_{targ}). In this way, it is possible to control independently the X and XX emission energies for a single QD and reconfigure the quantum interactions among charge carriers confined in QDs in a manner inaccessible with single perturbations used alone.

4.2.3. Electroelastic fields: erasing the fine structure splitting

The simultaneous application of two independent external fields allows a fundamental problem plaguing QDs (the presence of a coherent coupling of excitons) to be solved. When an external field is varied, the energetic levels of the two bright exciton states in a QD undergo an avoided crossing [80, 86, 184], similarly to the coupling in a QDM (see section 2.5.3). This is shown schematically in Fig. 4.12(a).

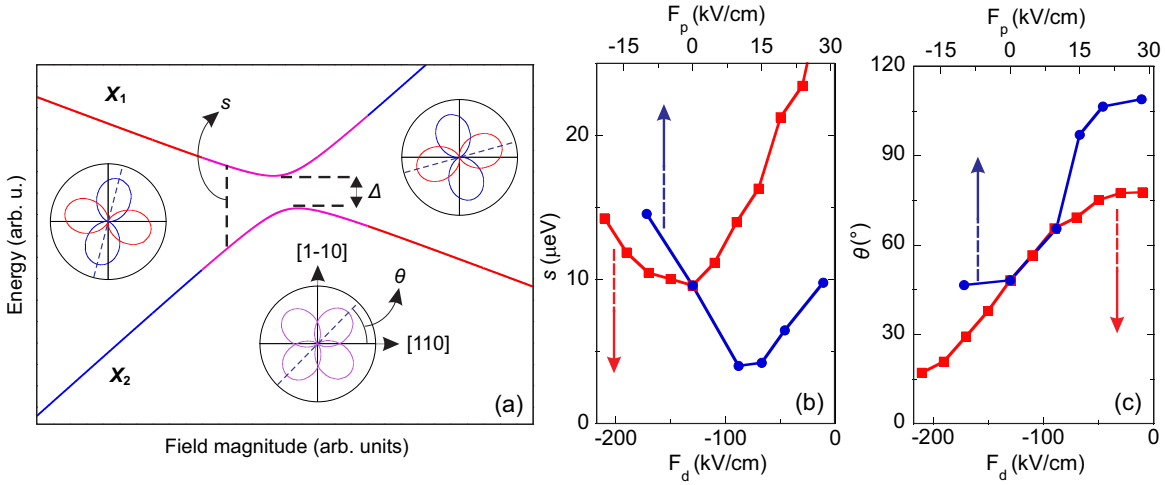

Figure 4.12.: (a) Sketch of the energetic levels of the two bright exciton states (X_1 and X_2) under the influence of a generic external field. The insets show a sketch of the angular distribution in the (001) plane of the light emitted by the two X. (b, c) Measured behaviour (symbols connected by lines) of the FSS (s) and polarisation angle (θ), respectively, for a QD as a function of F_p and F_d, top and bottom axis, respectively. In (b) and (c), the data as a function of F_p (F_d) are obtained with $V_d = 0$ V ($V_p = 0$ V). Figure from Ref. [149] (PL data taken by R. Trotta).

The minimum energetic distance between the two bright exciton states (X_1 and X_2) is the FSS (s) and θ is the polarisation angle of the low energy transition with respect to the [110] crystal direction. The coupling strength is given by the minimum s value (Δ) and the colours highlight the character of the states. The two components are assumed to have the same oscillator strength and to be oriented at 90° with respect to each other [see the insets of Fig. 4.12(a)]. The FSS and the θ of the excitonic emission are evaluated with sub-μeV resolution [80]. The spectra were measured at different angles ϕ of the $\lambda/2$ waveplate with respect to the [110] crystal direction (see section 3.5) and the energy difference between the exciton and biexciton transitions, $E_X(\phi) - E_{XX}(\phi) = 2|s|$, was extracted. This procedure permits small energy shifts induced by the rotation of the polarisation optics to be eliminated. The effects produced by the two fields (F_p and F_d) on s and θ are shown in Figs. 4.12(b) and 4.12(c) with

$V_d = 0$ V and $V_p = 0$ V, respectively. Although both trends follow the anticrossing pattern sketched in Fig. 4.12(a), it is clear that the coupling is influenced also by the strength and symmetry of the external perturbations.

It will be shown now that it is always possible to restore the exciton degeneracy by the simultaneous application of large strain and electric fields. The behaviour of the FSS for another QD is reported in Fig. 4.13(a) as a function of F_d for different values of F_p.

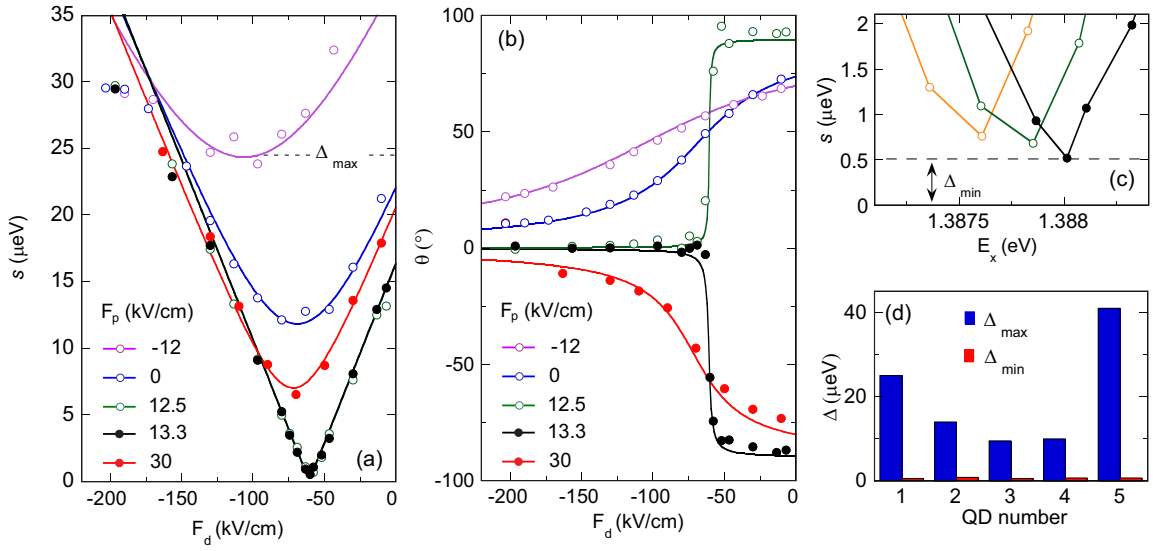

Figure 4.13.: Behaviour of (a) s and (b) θ as a function of F_d. The different curves correspond to different values of F_p. Δ_{max} indicates the maximum value of Δ observed for this specific QD. The solid lines are fits to the experimental data obtained using equations (4.3) and (4.4). (c) s as a function of E_x in the region of small FSS (circles connected by lines). The colours correspond to the F_p values shown in Fig. 4.13(a). The data taken at $F_p = 12$ kV/cm, not displayed in Fig. 4.13(a) for clarity's sake, are also reported (orange points connected by lines). Δ_{min} denotes the value of the minimum Δ. (d) Histogram of Δ_{max} and Δ_{min} for the different measured QDs. Figure readapted from Ref. [149] (PL data taken by R. Trotta).

The value of Δ increases up to a maximum value of Δ_{max} ~25 μeV for tensile strain ($F_p < 0$), while under compressive strain ($F_p > 0$) first it decreases to a minimum value (Δ_{min}) at $F_p = 13$ kV/cm, where FSS ≈ 0, and then increases again. Empty (full) circles show the experimental data for F_p smaller (larger) than 13 kV/cm. The confirmation that the critical point $s = 0$ has been crossed is given by looking at the polarisation angle θ as a function of F_d and F_p, as shown in Fig. 4.13(b). After the critical point, where $\Delta = \Delta_{min}$, the direction of rotation is inverted from anticlockwise to clockwise and the step-like function curve changes from positive to negative values. As seen more clearly in Fig. 4.13(c), FSS smaller than 1 μeV, comparable with the experimental spectral resolution (~0.5 μeV), can be obtained for different exciton emission energies. The finite spectral resolution of the experimental apparatus prevents $s = 0$ to be proved but Fig. 4.13(d) clearly indicates that electroelastic fields enable the FSS of most of

the QDs in the sample to be erased, despite the different properties of the quantum emitters. In fact, the same behaviour is systematically observed for other QDs chosen randomly in our device and even a FSS of 40 μeV (maximum value for InGaAs/GaAs QDs [80, 86]) can be tuned to values below 0.6 μeV.

A theoretical model is important for checking if $s = 0$ under the influence of strain and electric fields is possible. This will highlight the existence of an universal behaviour of the FSS independent of the specific QD parameters.
In ideal QDs with C_{2v} symmetry there is a FSS originating from the breaking of the D_{2d} symmetry [68]. Due to additional disorder, real QDs have only C_1 symmetry and the θ of the bright excitons further differs [68,184]. The effective two-level Hamiltonian for the bright excitons under the combined effect of a vertical electric field (F) applied along the [001] direction and an anisotropic biaxial stress [147] of magnitude $p = p_1 - p_2$, where p_1 and p_2 are the magnitudes of two perpendicular stresses applied along arbitrary directions in the (001) plane, takes the form:

$$H = [\eta + \alpha p + \beta F]\sigma_z + [k + \gamma p]\sigma_x, \tag{4.2}$$

where η and k account for the QD structural asymmetry, α and γ are related to the elastic compliance constants renormalised by the VB deformation potentials, β is proportional to the difference of the exciton dipole moments, and $\sigma_{z,x}$ are the usual Pauli matrices. It is important to note that higher order terms in p and F have been neglected. After diagonalisation, the following values of s and θ are obtained:

$$s = [(\eta + \alpha p + \beta F)^2 + (k + \gamma p)^2]^{1/2}, \tag{4.3}$$

$$\tan\theta_{\pm} = \frac{k + \gamma p}{\eta + \alpha p + \beta F \pm s}. \tag{4.4}$$

As shown by the lines in Figs. 4.13(a) and 4.13(b), there is an excellent agreement with the experimental data. Similar good agreement has been reported in the work of Gong *et al.* [190], between a continuum theory under a single perturbing field and atomistic calculations. Most importantly, the theory predicts $s = 0$ when the magnitude of p and F are:

$$p_{critic} = -\frac{k}{\gamma}, F_{critic} = \frac{\alpha k}{\gamma\beta} - \frac{\eta}{\beta}. \tag{4.5}$$

After this point, there is an inversion in the handedness of θ, which can be considered the experimental signature of the crossing of the $s = 0$ critical point. The large tuning range achieved with this device permits to access the values of p_{critic} and F_{critic} and to tune systematically all the QDs measured to $s = 0$.

By combining the theoretical analysis with the experimental data it becomes clear that having two independent and broad-range "tuning knobs" in the device is of crucial importance. When the eigenstates are oriented along the [110] direction (close to the [100]) or the perpendicular direction, the application of F_d (F_p) leads to $s = 0$. Since electric and strain fields act as effective deformations along, respectively, the [110] and close to the [100] directions, this implies that the exciton degeneracy can be restored if one external perturbation (e.g., F_d) is used to align the polarisation axis of the exciton emission along the axes of the second perturbation (e.g., F_p). The latter is then able to

compensate completely for the difference of the confining potentials of the two bright X eigenstates, i.e., is able to tune the FSS to zero and to invert the polarisation direction of the exciton emission. This explains also why there is an anticrossing of the two X states as a single external field is varied [80,86,184,190], where the probability to find a QD whose polarisation axis is aligned along the axis of the "tuning knob" is extremely low.

4.2.4. Realisation of highly entangled photons

In the previous section, it has been demonstrated that it is always possible to suppress the coherent coupling of the bright exciton states with a combined effect of electric and strain fields. By using this full control over the FSS and θ it can be shown how to obtain high-fidelity entangled photons in any QD from the XX-X cascade (see section 2.4.2). This work was done in collaboration with the group of Prof. A. Rastelli in Linz.

At first, strain (F_p) is used to precisely align θ along the "effective" axis of application of the electric field (F_d), as explained in section 4.2.3. This is achieved at the critical value F_p^*= 17.3 kV/cm for the particular QD reported in Fig. 4.14, as shown by the red circles in the inset of Fig. 4.14(b).

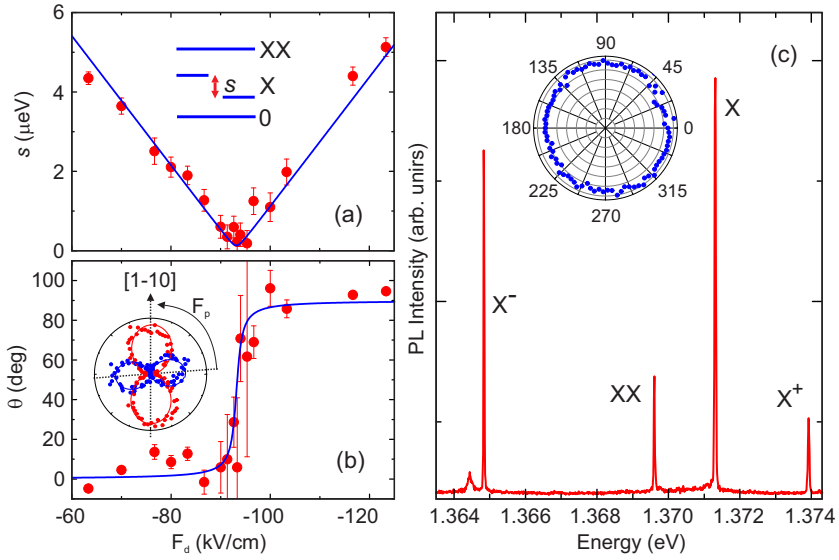

Figure 4.14.: Behaviour of the (a) s and (b) θ as a function of F_d for a QD whose polarisation direction has been previously aligned via F_p along the effective direction of application of the electric field. The blue line is obtained by the theoretical model in section 4.2.3. The inset of (b) shows the dependence (in polar coordinates) of ΔE as a function of the θ, at (F_d, F_p) = (−30 kV/cm, 0 kV/cm) and (F_d, F_p) = (−30 kV/cm, 17.3 kV/cm) (blue and red circles, respectively), as explained in the main text. (c) μ-PL spectrum of a representative QD at $s = 0$. The inset shows the intensity of the X emission as a function of the θ. 0° correspond to the [110] direction of the GaAs crystal. Figure from Ref. [151].

The FSS is obtained from the length of the petals following the procedure explained

in section 4.2.3. As a result, the FSS increases from 8 μeV to 11 μeV. The effect of the electric field (F_d) applied along the [110] or [1-10] directions [149] on s and θ is shown in Figs. 4.14(a) and 4.14(b), respectively. The FSS reaches the minimum value of $s = (0.2 \pm 0.3)$ μeV at the critical value $F_d^* = -93$ kV/cm and then it increases (linearly) again. On the other hand, θ remains constant and aligned along the [110] direction until an abrupt anti-clockwise rotation of 90° at F_d^*, when the minimum FSS occurs. This shows that the electric field was capable to compensate completely for in-plane asymmetries in the QD confinement potential, and can thus drive the FSS through zero. The **k·p** model developed in section 4.2.3 highlights the perfect agreement between the theoretical predictions and the experimental results [see the blue solid lines in Figs. 4.14(a) and 4.14(b)].
The μ-PL spectrum of a typical QD acquired at $s = 0$ is shown in Fig. 4.14(c), where the excitonic species have been already introduced in section 2.4.2. The source is unpolarised (within 4%) since the intensity of the X emission as a function of the angle the linear polarisation analyser forms with the [110] direction of the GaAs crystal has circular symmetry [see the inset of Fig. 4.14(d)].

Finally, the realisation of polarisation entangled photons from the radiative cascade XX-X-ground state can be demonstrated, following the proposal highlighted by Benson *et al.* (see section 2.4.2).
The maximally entangled Bell state (see equation 2.34) can be equivalently rewritten as $\psi = \frac{1}{\sqrt{2}}(|H_{XX}H_X\rangle + |V_{XX}V_X\rangle)$ or $\psi = \frac{1}{\sqrt{2}}(|D_{XX}D_X\rangle + |A_{XX}A_X\rangle)$, where $H(V)$ and $D(A)$ indicate horizontally (vertically)-polarised and diagonally (antidiagonally)-polarised photons, respectively. The first clear signature of entangled photons is shown in Figs. 4.15(a)-(f), where cross-correlation measurements between XX and X are reported for (a,d) circular, (b,e) linear and (c,f) diagonal polarisation basis for one of the investigated QDs. As predicted for photon pairs emitted in the maximally entangled Bell state ψ [191], strong bunching is observed when recording coincidence counts with the polarisations $H_{XX}H_X$ (or $V_{XX}V_X$), $D_{XX}D_X$ (or $A_{XX}A_X$) and $R_{XX}L_X$ (or $L_{XX}R_X$). On the other hand, the bunching peaks disappear for $H_{XX}V_X$ (or $V_{XX}H_X$), $D_{XX}A_X$ (or $A_{XX}D_X$) and $R_{XX}R_X$ (or $L_{XX}L_X$). As shown in Figs. 4.15(g)-(i), the degree of correlation (or correlation visibility) C_{AB} for entangled photons, defined as the difference between co-polarised and cross-polarised correlations divided by their sum, diverge from the ideal unitary values. More precisely, $C_{HV} = 0.72 \pm 0.05$, $|C_{RL}| = 0.82 \pm 0.02$, $C_{DA} = 0.72 \pm 0.05$. The fidelity, which provides a measure of how well the entanglement between these two states is preserved, can be calculated by following the formula reported in the work of Hudson *et al.* [182], $f = (1+C_{HV}+C_{DA}+C_{RL})/4$. The fidelity to ψ at zero time delay is estimated as $f = 0.82 \pm 0.04$, well above the classical limit [see Fig. 4.15(j)].

In order to completely characterise the entangled state the two-photon density matrix ρ has been reconstructed, measuring XX-X correlations in 36 polarisation settings and with the help of a maximum likelihood method [192]. The real and imaginary parts of ρ for a selected QD are displayed in Figs. 4.15(k) and 4.15(l), respectively. The presence of the strong off-diagonal terms $\rho_{HH,VV}$ and $\rho_{VV,HH}$ illustrates immediately the superposition of the two-photon pair wavefunctions. The minimum eigenvalue of the matrix partial transpose is negative (-0.35), which satisfies the Peres inseparability

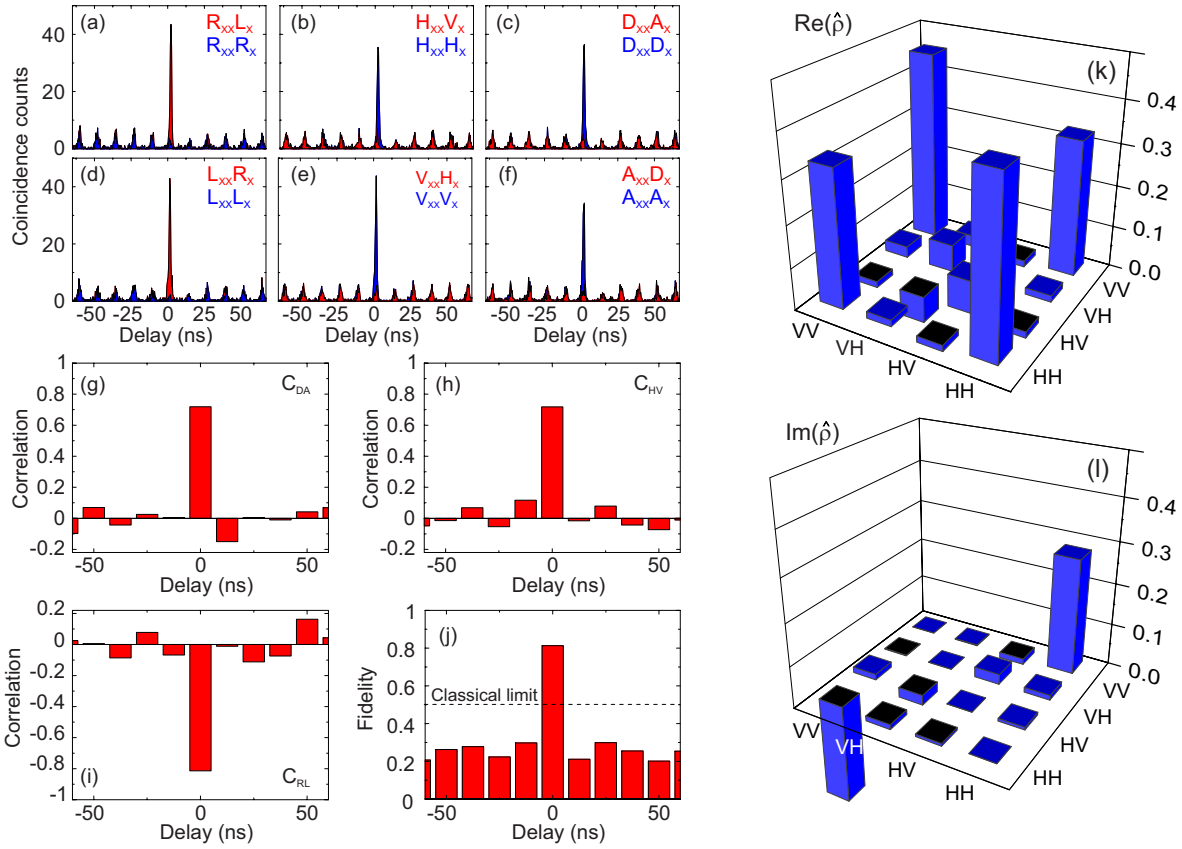

Figure 4.15.: (a)-(f) Polarisation resolved cross-correlation measurement of X and XX photons emitted by a QD whose FSS has been fine-tuned to zero. $R_{XX,X}$ ($L_{XX,X}$), $D_{XX,X}$ ($A_{XX,X}$), $H_{XX,X}$ ($V_{XX,X}$) indicate respectively right (left) circularly polarised photons, diagonally (anti-diagonally) polarised photons, and horizontally (vertically) linearly polarised photons. (g)-(i) Degree of correlation in the (g) diagonal, (h) linear and (i) circular bases for the same QD as in (a)-(f). (j) Fidelity to the maximally entangled Bell state for the same QD as (a)-(i). (k) Real and (l) imaginary part of the two-photon density matrix reconstructed via quantum-state tomography in a QD at $s = 0$. Figure readapted from Ref. [151].

criterion for entanglement [193].
The imaginary components point out to the presence of a phase delay between $|H_{XX}H_X\rangle$ and $|V_{XX}V_X\rangle$ and that this is not exactly the maximally entangled Bell state ψ but rather $\psi \sim \frac{1}{\sqrt{2}}(|H_{XX}H_X\rangle + e^{-i(0.23\pi)}|V_{XX}V_X\rangle)$, which corresponds to the largest eigenvalue $\lambda = 0.86$ of ρ. This phase delay arises most probably from a reflection at the beam splitter. Following the work of James *et al.* [192], the following metrics are extracted from ρ: the tangle (T), concurrence (C) and entanglement of formation (E_F). For a perfect source of entangled (classical) light all these parameters should be equal to 1 (0). For the best QD studied here it is obtained T = 0.56 ± 0.03, C = 0.75 ± 0.02, $E_F = 0.66 \pm 0.05$. These values rate as the highest ever reported for QD-based photon sources [8, 78, 80, 163, 183, 186, 187] and, most importantly, for an electrically-controlled optoelectronic device [8, 80, 163] without the aid of temporal or spectral filtering. Despite all the QDs investigated in the device differ in terms of emission energy, linewidth, XX binding energies, F_p^* and F_d^* values, they all show a very high level of entanglement with average concurrence (largest eigenvalue λ) equal to 0.72 (0.86).

In conclusion, a device where the InGaAs/GaAs QD emission properties are engineered by large electroelastic fields, provided by diode-like nanomembranes integrated onto piezoelectric actuators, has been presented. The two fields modify the interaction energies among electrons and holes in a different manner, allowing for a reshaping of the QD electronic properties. It is demonstrated that the biexciton binding energy can be modified from a binding to an antibinding configuration without affecting the energy of the exciton transition, when the two external perturbations work one "against" the other. Most importantly, the simultaneous application of electric and elastic fields allow to control and cancel the exciton FSS in all the QDs measured. A simple theoretical model, which holds for every QD structure, was developed for supporting the experimental observations. Finally, the demonstration that virtually any QD can be used for the generation of entangled photons, featuring the highest degree of entanglement reported to date for QD-based photon sources with concurrence as high as 0.75 ± 0.02, was given.

4.3. Controlling the formation of QD pairs using nanohole templates

Optically active QDMs (see section 2.5) are potential candidates as the building blocks for quantum computation and cryptography, where more than one qubit operation is required [27, 29]. In contrast with vertically stacked QDs (see section 4.4), the lateral geometry offers advantages such as easy application of lateral electric fields to influence the coupling [106], scalability, and very similar strain situations for all dots.
Laterally interacting QD pairs can be obtained in different ways, taking advantage of the random dot nucleation at step edges [194], when two QDs nucleate close enough to each other [195], or, in a more deterministic way, by modifying the substrate morphology. For example, QD pairs have been grown on the facet edges of mounds [196], at the corners of pyramidal structures formed during selective area epitaxy [197] or on the edges and the bottom of nanoholes [165, 198]. These nanoholes have been created by burying QDs followed by *in situ* strain-selective etching [198, 199] or by thermal annealing [200]. It is also possible to use *ex situ* patterning, which allows the QDM to be positioned at a pre-determined location [201, 202], if the pattern size and growth conditions are carefully selected [199, 203]. A third method is to etch nanoholes *in situ* by using a gallium droplet, where the transition from QD to QD pair was achieved by change in As species [165].

In this section, an alternative and robust method for the QD pair formation will be demonstrated. Self-assembled nanoholes are created *in situ* by droplet etching and the control of the InGaAs/GaAs QD pairs is obtained via a thin GaAs buffer overgrown on the nanoholes. The effect of growth parameters such as indium amount, substrate temperature and arsenic overpressure on this system is investigated. Finally, the optical quality of the capped QD pairs with a thick GaAs layer is shown.

4.3.1. Growth method

The growth of InGaAs QD pairs on nanoholes is described here. Following oxide desorption, a thick undoped GaAs buffer was grown on a GaAs (001) substrate at T_{sub} of 580°C. Then, nanoholes were realised on the surface by supplying 2.85 ML excess gallium (growth rate = 0.25 ML/s) at T_{sub} = 500°C with the As repeatedly pulsed (F_{As} = 0.6 ML/s). This corresponds to a Ga effective rate of 0.05 ML/s, as measured by RHEED oscillations (see section 3.1). At this arsenic overpressure, the transition between the (2 × 4) and c(4 × 4) GaAs surface reconstructions occurs around 500°C. The excess gallium forms droplets on the substrate which etch nanoholes in the surface after 300 s of annealing under As, as described in section 4.1.1. The nanoholes are randomly distributed on the surface with a density of $\sim (1.1 \pm 0.4) \times 10^8$ cm^{-2}. Differently to the GaAs/AlGaAs QD case, the nanoholes are then overgrown with a GaAs buffer of thicknesses (0 − 40) nm at 0.25 ML/s followed by 120 s growth interrupt, in order to vary T_{sub} and allow Ga to diffuse in the nanohole. Finally, (1.3 − 1.6) ML of InAs (growth rate = 0.01 ML/s) was deposited at T_{sub} and As in the ranges (470 − 500)°C and (0.6 − 1.2) ML/s, respectively, followed by a 30 s growth interrupt before quenching of the sample. No spots in the RHEED were seen

during the InAs deposition or the anneal for InAs amounts less than 1.6 ML (θ_{crit} for dot formation on a flat GaAs surface, see section 3.1.1). In fact, the density and size of dots forming in the nanoholes were too low for leading to spots observable in the RHEED pattern.

In total, four series of nanohole samples were grown, as detailed in table 4.1.

	GaAs buffer (nm)	InAs amount (ML)	T_{sub} ($^{\circ}C$)	As flux (ML/s)
Series 1	$0 - 40$	1.5 ($0.83\ \theta_{crit}$)	490	0.6
Series 2	10	$1.3 - 1.6$ ($0.72 - 0.89\ \theta_{crit}$)	490	0.6
Series 3	10	$1.4 - 1.6$ ($0.81 - 0.74\ \theta_{crit}$)	$470 - 510$	0.6
Series 4	10	1.5 ($0.83 - 0.88\ \theta_{crit}$)	490	$0.6 - 1.2$

Table 4.1.: Description of growth parameters used for different sample series. InAs amount is given as a fraction of the critical thickness (θ_{crit}) for dot formation on a planar region, measured by the onset of spots seen on the RHEED pattern.

4.3.2. Role of the GaAs buffer

The shape of the as-etched nanoholes can be modified by the growth of a thin GaAs buffer layer (series 1 in table 4.1), leading to the formation of lateral InGaAs QD pairs at the bottom of the holes during InAs overgrowth. AFM measurements of 20 nanoholes after the droplet etching step show that the nanohole is elongated along the [110] direction. The initial mean depth is (10.5 ± 0.7) nm, and the mean width along the [110] and [1-10] directions are (77 ± 6) nm and (60 ± 3) nm, respectively, where the depth and width were measured relative to the surrounding substrate, as shown in Fig. 4.16(a).

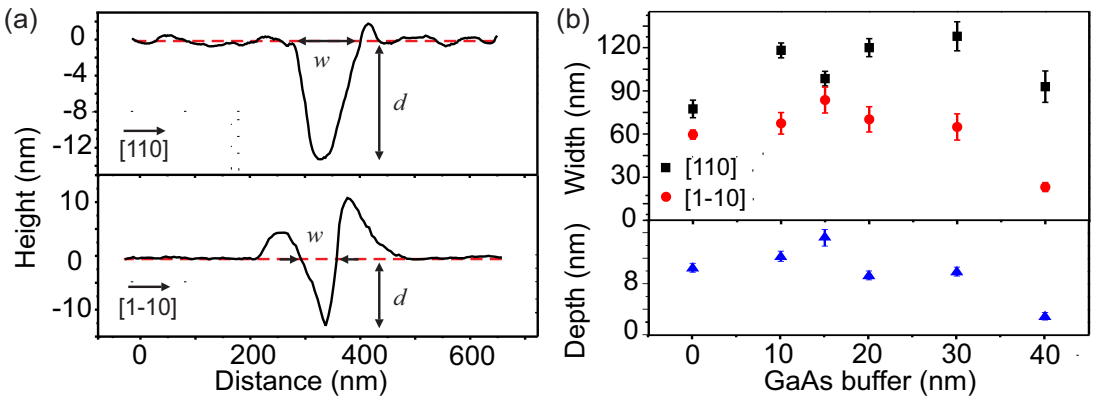

Figure 4.16.: (a) Line sections of a nanohole along the [110] direction (top) and [1-10] direction (bottom), where w is the width and d is the depth. (b) Width of nanoholes along the [110] and [1-10] directions (top) and depth (bottom) varying the GaAs buffer from 0 to 40 nm (average of 20 nanoholes). Figure readapted from Ref. [153].

Figure 4.16(b) shows that the width of the hole in the [110] direction increases with GaAs buffer deposition, staying approximately constant for GaAs buffer thicknesses

of (10 − 30) nm, with maximum value (128 ± 10) nm at 30 nm buffer growth but decreasing by 40 nm buffer growth to (93 ± 11) nm. In the [1-10] direction the trend is similar, with the width reaching a maximum of (84 ± 9) nm after 15 nm buffer growth and subsequently decreasing to (23 ± 3) nm for 40 nm buffer growth. The depth also follows this trend, reaching a maximum of (15 ± 1) nm after 15 nm buffer growth, and subsequently decreasing to (2.9 ± 0.6) nm after 40 nm buffer growth. This initial increase in depth implies that initially there is net migration away from the bottom of the hole towards the neighbouring planar area, but that, after ∼15 nm of GaAs overgrowth the direction of this net migration is reversed and the hole begins to infill. This shows that the concave curvature is not the dominant driving force for adatom migration during the initial stages of growth.

AFM images of nanoholes with 0, 20 and 40 nm buffer are shown in Fig. 4.17(a).

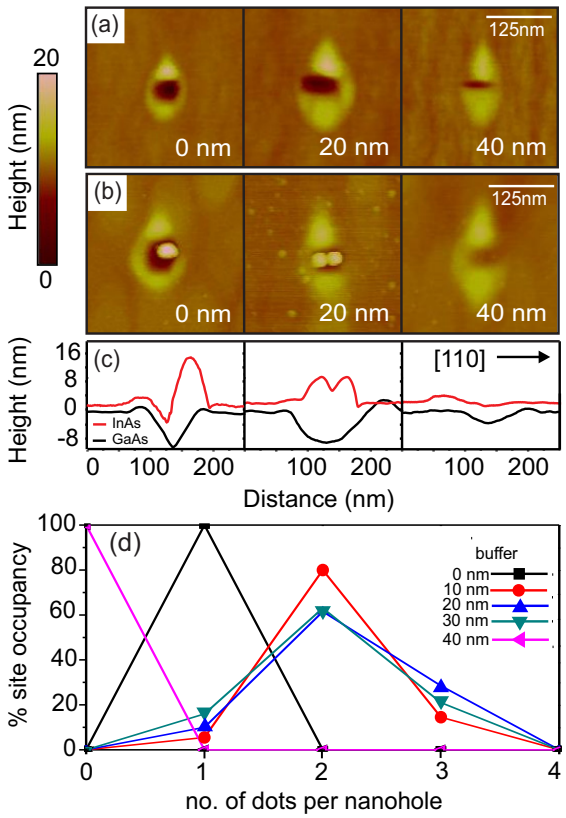

Figure 4.17.: (a) AFM images (250 nm × 250 nm) of nanoholes after 0, 20 and 40 nm GaAs buffer overgrowth and (b) after 1.5 ML InAs deposition at substrate temperature (T_{sub}) of 490°C with (c) respective line sections along the [110] direction. (d) Plot of the percentage site occupancy versus the number of dots per nanohole (statistics on over 100 nanoholes). Figure readapted from Ref. [152].

The nanoholes are surrounded by elevated GaAs mounds, ∼ (2 − 5) nm in height, extending more in the [1-10] than the [110] directions. The corresponding InAs dot distribution after 1.5 ML deposition over these nanoholes is shown in Fig. 4.17(b), with respective linescans in Fig. 4.17(c).

The nanoholes with (0 − 30) nm buffer clearly act as preferential nucleation sites for

dot formation, with dots forming at deposition amounts less than θ_{crit}. For as-grown nanoholes with no GaAs buffer the hole bottom is sharply curved and a single dot forms at the position of maximum curvature. In general, the QD is slightly offset with respect to the centre of the nanohole, due to asymmetry in the self-assembled nanohole. After 20 nm buffer growth, the nanohole outline is much flatter and wider at the bottom, and two QDs nucleate at the corners of the hole, where the surface curvature changes most rapidly. The preferential nucleation is due to net InAs migration towards the bottom of the hole. In fact, the larger step density at the corners of the hole enhances the growth rate towards the hole and hence accelerates the dot formation. The dots inside the nanoholes (in a QD pair) are typically $(5 - 10)$ nm high and $(35 - 45)$ nm in diameter. The peak-to-peak distance between them is $\sim$44 nm for holes with a 10 nm buffer, and this distance reduces with increasing buffer thickness down to $\sim$35 nm for a 30 nm buffer thickness. The hole after 40 nm buffer growth, however, has simply been infilled with planar InGaAs, since the amount of material that accumulates in the hole is not enough to overcome the critical strain, leading to dot formation.
The effect of the buffer thickness on the occupancy of over 100 nanoholes is shown in Fig. 4.17(d). The highest value of QD pairs is 80% with a 10 nm buffer, and decreases to around 60% for 20 and 30 nm buffers. This decrease is reflected by an increase in the number of singly and triply occupied nanoholes and is probably due to increasing size and shape fluctuations of the nanoholes as they start to infill. For samples with $(10 - 30)$ nm buffers around 20% of nanoholes contain triple dots aligned along the [110] direction, due to the elongation of the hole.

4.3.3. Effect of growth parameters

The effect of varying growth parameters such as InAs amount, T_{sub} and As overpressure will be now considered. Figures 4.18(a) and 4.18(b) show, respectively, AFM images and linescans of typical nanoholes overgrown with a 10 nm GaAs buffer and different InAs deposition amounts (series 2 in table 4.1). After 1.3 ML InAs deposition the hole is infilled, but there is not enough material to initiate QD formation in the nanohole. However, by 1.4 ML deposition, 64% of the holes contain QD pairs, increasing to 73% after 1.5 ML deposition, as shown in Fig. 4.18(c). Raising the deposition from 1.4 ML to 1.5 ML leads both to an increase in height and diameter of the dots in the nanohole, such that by 1.5 ML the dots are beginning to merge and most of those double dots are not distinct. By 1.6 ML deposition the QD pairs have coalesced, forming very large and incoherent dots that are very efficient at capturing indium adatoms [204].

The amount of InAs accumulated in the nanoholes after 1.3 ML deposition can be used to get an estimate of the net migration towards the bottom of the nanohole.
In the following, any possible mass transport of the GaAs substrate towards the nanohole during the InAs deposition will be neglected. This seems reasonable since there is no change in the nanohole sidewall profile and surrounding GaAs mound, which implies that the infilling of the nanohole is solely due to net migration of the deposited InAs. The interdiffusion of the InAs at the bottom of the hole with the surrounding GaAs will occur [205] but it is believed to be negligible. If the infilled nanohole is approximated as a partially filled half-ellipsoid [152], considering the density of nanoholes

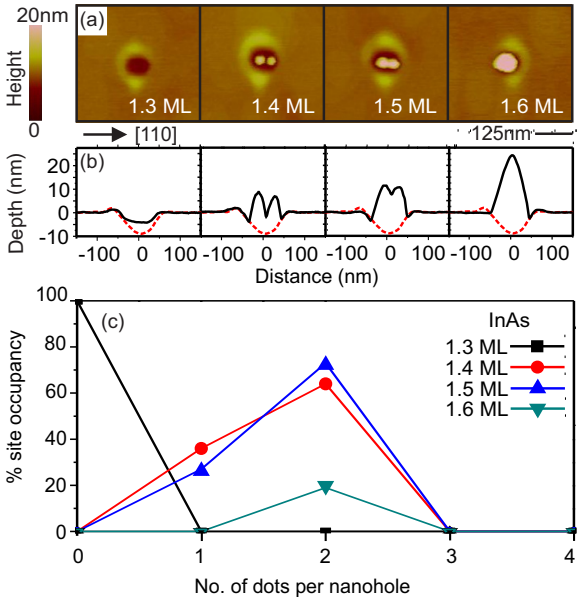

Figure 4.18.: (a) AFM images (375 nm × 375 nm) and (b) line sections along the [110] direction of the nanoholes following 10 nm GaAs buffer overgrowth and InAs deposition, with amount varying from 1.3 ML to 1.6 ML and T_{sub} = 490°C. The red dashed line is the line section of the nanohole following 10 nm GaAs buffer overgrowth. (c) Plot of the percentage site occupancy versus the number of dots per nanohole (statistics on over 100 nanoholes). Figure readapted from Ref. [152].

for this particular sample, by looking at the volume of the nanohole it is calculated that $\sim (7-8)\%$ of the total InAs is deposited in the nanoholes. Since the nanoholes only cover ∼0.9% of the surface area, the average net surface flux towards the nanoholes is about seven times that of the incident flux. This net surface flux will be driven both by the capillarity effect of the concave surface curvature at the bottom of the hole and the high step density on the hole sidewalls.

The net migration towards the nanohole can be modelled by solving the steady state diffusion equation in cylindrical coordinates:

$$-D\left[\frac{d^2n}{dr^2}+\frac{1}{r}\frac{dn}{dr}\right]=F-\frac{n}{\tau_c}, \tag{4.6}$$

where D is the surface diffusion coefficient, n is the adatom density, r is the distance from the centre of the hole, F is the incident flux and τ_c is the lifetime until incorporation of an adatom. The solution reads:

$$n=AI_0\left(\frac{r}{\lambda_D}\right)+BK_0\left(\frac{r}{\lambda_D}\right), \tag{4.7}$$

where A and B are constants defined by the boundary conditions, I_0 and K_0 are the modified Bessel functions [206] and $\lambda_D=\sqrt{D\tau_c}$ is the diffusion length. For simplicity, it has been assumed circular symmetry and used boundary conditions of continuous adatom concentration and flux at the hole edge, and zero adatom flux at distance

$1/\sqrt{\pi\rho^2}$ (ρ is the nanohole's density) from the hole centre, to account for competition from neighbouring nanoholes. Since most of the hole sidewall is only ∼10° from the horizontal plane, a constant diffusion coefficient, D = 4.2 × 10^{-6} cm^2s^{-1} at 500 K [207], for both the planar surface and nanohole can be considered. The experimentally observed hole infilling implies that the average lifetime for incorporation in the nanohole ($\tau_c{}^{hole}$) is ∼0.13 times the lifetime for incorporation on a planar surface ($\tau_c{}^{surface}$) for $\rho = 1.8{\times}10^8$ cm^{-2}, as shown in Fig. 4.19.

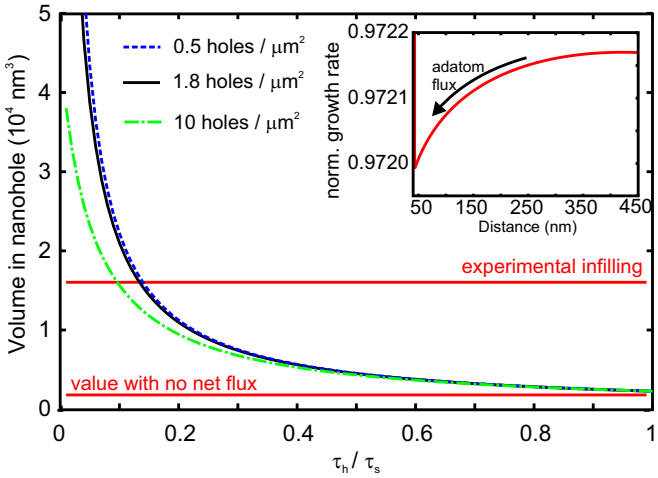

Figure 4.19.: Plot of the modelled infilling of the hole after 1.3 ML InAs deposition, assuming a circular hole and steady state isotropic diffusion, as a function of the ratio between the adatom capture time in the hole (τ_h) and the surrounding area (τ_s). The inset shows the calculated reduction in growth rate (0.01 ML/s) on the planar surface as a function of the distance from the hole center, due to the net adatom flux towards the hole for a value of $\tau_h/\tau_s = 0.13$. Figure from Ref. [152] (modelling from P. Atkinson).

This model predicts only a weak dependence of the infilling on the spacing of the nanoholes, with the infilled volume per nanohole changing by less than 2% over the density range $(0.5-2){\times}10^8$ cm^{-2} and less than 12% over the range $(2-10){\times}10^8$ cm^{-2}, which is supported by other observations [203].

The effect of T_{sub} on the QD pair formation over nanoholes overgrown by a 10 nm buffer is also investigated (series 3 in table 4.1). Figure 4.20(a) shows the AFM images and profiles of an InGaAs QD pair grown at 470, 490 and 510°C, respectively.
The first clear result is that the probability of QD pair formation is relatively independent of the used substrate temperature. Increasing T_{sub} leads to an increase in indium desorption [189]. This means that the amount of InAs which must be deposited for dot formation should be increased, as measured by the onset of spots in the RHEED pattern. As a result, depositing between $(75-80)$% of θ_{crit} leads to between 60% and 80% of nanoholes containing QD pairs. However, it is observed that for achieving clearly defined QD pairs the amount of InAs relative to θ_{crit} must be reduced at higher growth temperature. Even with this reduced deposition amount, QD pairs grown at higher temperatures are larger, both in height and diameter, and more likely to become merged with dislocation forming at the point of contact, which may damage their optical properties.

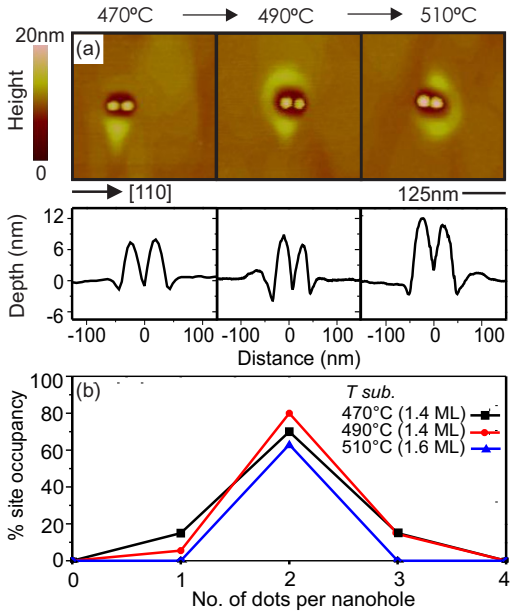

Figure 4.20.: (a) AFM images (375 nm × 375 nm) and line sections along the [110] direction of the InGaAs QD pairs varying the substrate temperature from 470°C to 510°C with 10 nm GaAs buffer. The InAs amount is 1.4 ML at T_{sub} = 470°C and 490°C and 1.6 ML at T_{sub} = 510°C. (b) Plot of the percentage site occupancy as a function of the number of dots per nanohole (statistics on over 100 nanoholes). Figure readapted from Ref. [152].

The migration length of indium is expected to almost double with increasing T_{sub} over the range 470°C to 510°C [208]. However, from our experiment and model, the infilling of the hole is hardly affected by the absolute diffusion length on the flat surface [152]. Instead, the increase in material accumulation could be described by a small decrease in the ratio of ${\tau_c}^{hole}/{\tau_c}^{surface}$ of only ∼10%. This would imply that the lifetime of incorporation over the hole increases slightly less with increasing temperature than the lifetime on a flat surface.

Finally, in Fig. 4.21 the effect of As overpressure on the InGaAs QD pair formation is considered (series 4 in table 4.1).
As the arsenic increases from 0.6 to 0.95 ML/s the hole becomes less wide in the [110] direction and the dots get closer together. When the arrival As flux is 1.2 ML/s, the difference in hole shape is extreme. The hole collapses, becoming much shallower (∼9 nm to ∼4 nm deep), and the mound of GaAs around the sides of the hole becomes higher and much more elongated along the [1-10] direction. This change in GaAs morphology is due to large amount of mass transport occurring under the higher As flux, which can also be seen if no InAs is deposited and the nanohole is simply annealed at T_{sub} of 490°C for 180 s. Increasing the As overpressure at 1.2 ML/s forces the surface, which was in the disordered (2 × 4) reconstruction, into the c(4 × 4) reconstruction with substantial rearrangement of Ga surface atoms. The collapse of the hole is due to the preferential incorporation of Ga adatoms onto B-type step edges [209]. This supports the idea that the nanohole sidewalls are gallium terminated after etching.

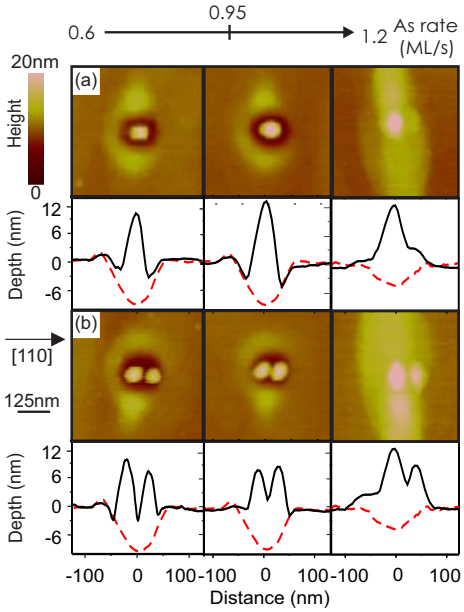

Figure 4.21.: AFM images (250 nm × 250 nm) and line sections along the [110] direction of the (a) single and (b) pair of InGaAs QDs at T_{sub} = 490°C, varying the As flux from 0.6 ML/s to 1.2 ML/s with 10 nm GaAs buffer and 1.5 ML InAs on top of the surface. The red dashed line shows the profile of the nanohole after 10 nm GaAs buffer overgrowth and 30 s anneal at T_{sub} of 500°C under the stated arsenic flux. Figure from Ref. [152].

The effect of the change in hole shape is a shift in the occupancy of the nanoholes away from QD pair occupation, towards more holes containing single dots. In the instances that two dots can be seen it is not clear whether the second dot has nucleated over the hole, or, more probably, on the highly stepped edges of the mound surrounding the hole.

4.3.4. Buried InGaAs QD pairs

In order to understand the shape evolution of the QD pairs during GaAs capping, a sample with InGaAs/GaAs QD pairs was grown over nanoholes covered by a 15 nm GaAs buffer. The sample before capping consists of nanoholes containing two dots of similar size, as shown in the AFM image of Fig. 4.22(a), where the growth was interrupted after the formation of InGaAs QD pairs.
T_{sub} for InAs deposition was 490°C. Due to the intermixing between InAs and GaAs, for the first 5 nm during capping T_{sub} was reduced to 460°C, after which it was ramped up to 490°C for 10 nm and to 570°C for the remaining 55 nm of the GaAs cap. By using a $1NH_4OH{:}1H_2O_2{:}25H_2O$ solution, which etches selectively GaAs over InGaAs alloy with a rate of 10 nm/s [210], it was possible to selectively remove the GaAs capping layer, and reveal the buried InGaAs dots, as shown in the AFM image of Fig. 4.22(b). The centre-to-centre spacing of the capped dots is (39 ± 9) nm, which confirms that the QD pair is hardly changed during the capping process.

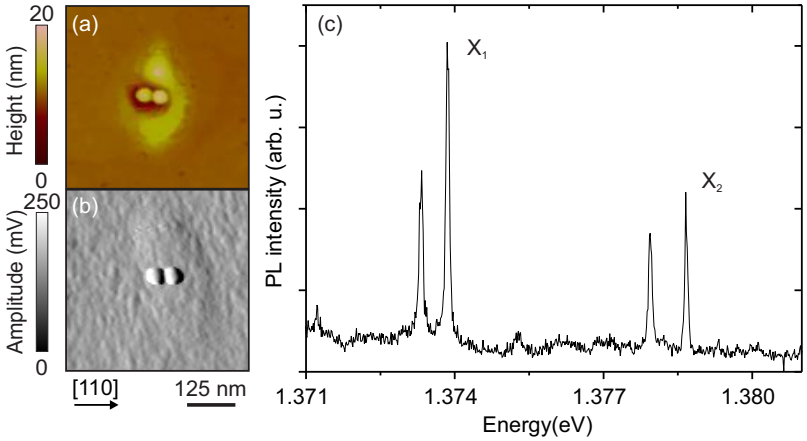

Figure 4.22.: AFM images (500 nm×500 mm) of lateral InGaAs/GaAs QD pairs (a) on surface and (b) buried after selective chemical etching in ammonia solution of the 65 nm GaAs cap (amplitude scan for better contrast). (c) Typical emission spectrum at 5 K of the InGaAs/GaAs QD pairs capped with a thick GaAs layer. Figure (b) readapted from Ref. [153].

The emission spectrum of these QD pairs was investigated by depositing a thicker GaAs capping layer (∼150 nm). Two groups are visible with two neutral excitons [X_1 and X_2 in Fig. 4.22(c)] and two additional lines showing no FSS. The larger FWHM (∼80 μeV) compared to that of a single InGaAs QD on a flat surface (see section 4.2) may be explained by the etching of the nanohole step, which introduces defects in the substrate.

In conclusion, a robust method to grow low density lateral InGaAs QD pairs using a template of nanoholes formed by droplet etching has been demonstrated. Up to 80% of nanoholes containing QD pairs has been observed after depositing over the nanohole a thin GaAs buffer of $(10 - 30)$ nm. The QD pairs form following deposition between 1.3 ML and 1.6 ML at T_{sub} of 490°C with an arsenic arrival flux of 0.6 ML/s. Due to the elongation of the nanoholes, they are aligned along the [110] direction and have centre-to-centre separation of ∼35 nm. From the infilling of the hole a net surface flux towards the hole of ∼7 times the incident flux is observed. Using a model based on the surface diffusion equation, the incorporation lifetime for indium in the nanohole is estimated to be ∼0.13 times that on a planar surface. For deposition amounts greater than 1.6 ML the dots of the QD pair coalesce. Increasing T_{sub} does not significantly alter the dot distribution. However, the nanohole partially collapse with increasing As, due to mass transport as the substrate passes through a surface reconstruction transition. The μ-PL of capped QD pairs underlines good optical quality and a selective etching of the capping layer was used to confirm the double occupancy of the nanoholes. It is worth noticing that the latter analysis based on cap removal also allows to rule out pronounced morphological changes for surface InGaAs QDMs occurring during sample cooling and confirm the reliability of studies based on room temperature AFM. In addition, due to the very low surface density of QDMs, cross-sectional methods such as X-STM and TEM are hardly applicable to this system because of the low probability of finding single QDMs in cleaved or thin specimens.

4.4. Strain-induced active tuning of the coherent tunneling in QDMs

Vertically stacked self assembled InGaAs QDs in a GaAs matrix are the most widely studied QDMs using optical spectroscopy [35–37, 113], in order to define a quantum array and face the scalability challenge. They can also give additional insight into the interactions that apply to single QDs, by investigating their spin properties and the fine structure of the optical spectra [40, 98, 104, 211]. However, the active control of the coupling strength between the two QDs−the key parameter determining the operation rate of quantum gates (see section 2.5.6)−has never been demonstrated. In particular, the probability of the transition from one AC branch (see section 2.5.3) to the other, the so-called Landau-Zener transition [212], important in qubit manipulation [39], increases exponentially as the coupling strength is decreased. Some qubit proposals [34] also require comparable electron and hole tunnelling rates [100]. The spacer thickness in vertical QDMs is frozen and, contrary to electrostatically defined QDMs [213], there is no growth protocol [33] allowing an active control over the spin-qubit. A post-growth tuning of the coherent tunnelling in vertical QDMs, using longitudinal or transverse magnetic fields [214], would overcome this shortcoming but recent experiments and refined theoretical treatments have shown no significant changes in the AC energy gaps for fields up to 6 T [215]. While piezoelectric-induced strains have been used previously to control several properties of semiconductor structures (see section 2.4.3 for details), their potential in the field of QDMs has not been explored so far.

In this section, the first strain tunable InGaAs/GaAs QDM-based device is introduced and the vertical alignment of the dots is characterised. Then, the tunability of the emission wavelength and the active tuning of the coupling strength of holes confined in the single QDM, by externally induced strains and electric fields, is demonstrated. Finally, the effect of these external perturbations on the FSS and the polarisation angle are discussed.

4.4.1. Sample description and vertical alignment

In order to transfer large stress and electric fields to single QDMs, a device design similar to the one described in section 4.2.1 has been realised. The QDMs consist of two vertically stacked InGaAs QDs [31, 32] embedded in the intrinsic region of n-i-p nanomembranes integrated onto PMN-PT, as shown in the sketch of Fig. 4.24(a).

The sample was grown by solid source MBE (see section 3.1) on semi-insulating GaAs (001) substrate. Following oxide desorption, a 300-nm-thick undoped GaAs buffer layer was grown at $T_{sub} = 570°C$. A 100-nm-thick sacrificial layer of $Al_{0.75}Ga_{0.25}As$ was deposited, followed by a 170-nm-thick n-doped (Si at 5×10^{18} cm^{-3}) GaAs layer, a 30-nm-thick n-doped (Si at 5×10^{18} cm^{-3}) $Al_{0.4}Ga_{0.6}As$ layer, a 74.3-nm-thick intrinsic $Al_{0.4}Ga_{0.6}As$ layer and a 10-nm-thick GaAs intrinsic layer containing in the centre a double layer with low density InGaAs QDs. At the beginning of the n-doped GaAs layer, a δ-doping layer (Si at 1.2×10^{13} cm^{-2}) was introduced for an *in situ* n-type ohmic contact [188] in the subsequent device processing. The growth was completed with a 74.3-nm-thick intrinsic $Al_{0.4}Ga_{0.6}As$ layer, a 30-nm-thick p-doped (C at 5×10^{18} cm^{-3})

$Al_{0.4}Ga_{0.6}As$ layer, and a 53-nm-thick p-doped (C at 5×10^{18} cm^{-3}) GaAs layer with higher doping for the last 6 nm (C at 1×10^{19} cm^{-3}), in order to ensure a good ohmic contact. The GaAs/AlGaAs QW reduces carrier escape at high electric fields (F_d) across the diode (see section 2.4.3).
Similarly to the single-QD device (see section 4.2.1), the thickness of the nanomembrane and the position of the QDM layer were optimised for the formation of a simple metal-semiconductor planar cavity. The width of the cavity was chosen as 1.67λ, which corresponds to a nanomembrane ∼450 nm thick for $\lambda = 930$ nm. The QDs were positioned at 1λ from the sacrificial layer.
The sample was rotated during the growth and the low density of QDs was obtained by taking advantage of the temperature gradient across the wafer during growth, as described in section 4.2.1. The double layer of InGaAs QDs was grown at T_{sub} of 505°C with 5.4 nm GaAs spacer in between. The QD height was controlled by the *indium flush* growth method (see section 3.1.1): The PCA dots were capped with thin GaAs layers (2.9 nm/3.3 nm for the bottom/top dot) at the same temperature and then annealed at 570°C for 180 s, in order to remove the InAs from the exposed portion of the dots.

The thin *n-i-p* nanomembranes containing QDMs are integrated onto PMN-PT by gold thermocompression bonding (see section 3.4). The different confined energy levels in the two dots are tuned into resonance by applying a voltage (V_d) across the nanomembranes. Although the top dot is usually larger than the bottom dot because of strain-enhanced nucleation, differences in strain, composition and size cause that the hole ground state in the bottom dot is usually lower in energy. This means that hole tunnelling (see section 2.5.3) can be induced with our sample design. Simultaneously, in-plane (compressive or tensile) biaxial stress is transferred to the QD layers by applying a voltage (V_p) across the PMN-PT.

The vertical alignment for the bilayer configuration (top QD layer separated by 5.4 nm GaAs from the bottom PCA QD layer capped at 2.9 nm) is investigated by means of a statistical analysis of the diameter, height and aspect ratio (height/diameter). Test samples were grown, where the growth was stopped after the single layer, or after the second layer of InAs QDs, as shown respectively by the blue and red columns of Figs. 4.23(a)-(f). The dots are grown at T_{sub} of 505°C by depositing ∼2 ML InAs. The bottom layer of Figs. 4.23(a)-(c) consists of PCA QDs capped with 2.9 nm GaAs, annealed at 575°C for 180 s and additionally capped with 5.4 nm GaAs. Figures 4.23(d)-(f) display the same statistical analysis but the dots in the bottom layer were instead capped directly with 5.4 nm and T_{sub} was not changed before the growth of the second dot layer. For the sake of clarity, in the following the two kinds of vertically stacked QD will be named as type A and type B, respectively. In order to get ensemble information, the samples are studied on the high density regions (density $> 10^{10}$ cm^{-2}, see section 4.2.1 for details).

The single layer of dots shown in Figs. 4.23(a)-(f) (blue bars) has an average diameter of (32 ± 8) nm and a bimodal height distribution with peaks at (3.1 ± 0.8) nm and (17.1 ± 0.3) nm. After partially capping with 2.9 nm GaAs and annealing, the dots A show a very similar diameter to the lower dot layer of (32 ± 14) nm [red bars in Fig. 4.23(a)] and a bimodal height distribution with the peaks shifted to taller dots by

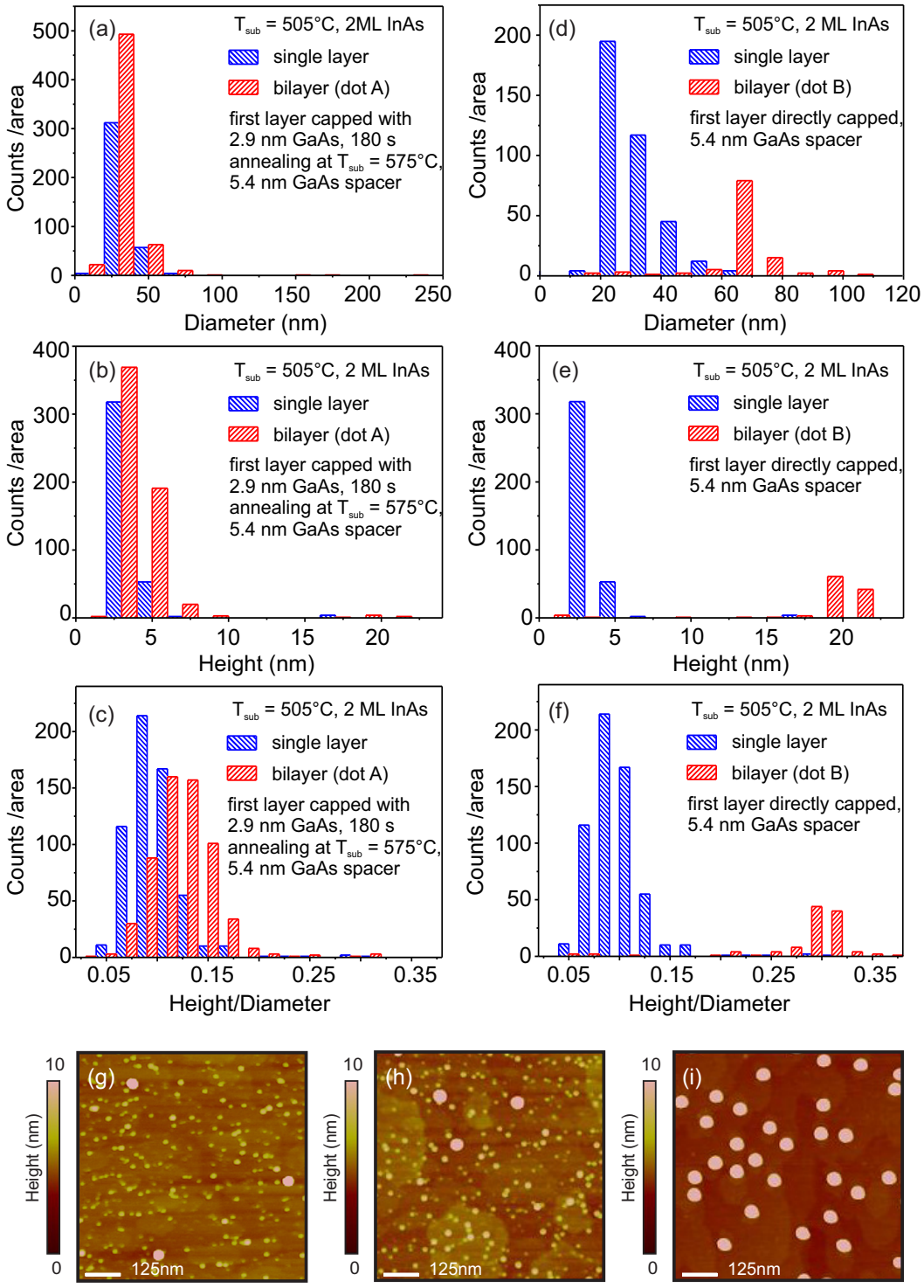

Figure 4.23.: Histograms of QD distribution per area (2 μm $\times$ 2 μm) of (a,d) diameter, (b,e) height and (c,f) aspect ratio (height/diameter) for two stacked InGaAs QDs layers (red column) separated by 5.4 nm GaAs to the first partially capped and annealed QD (dot A) and directly capped with 5.4 nm GaAs without annealing (dot B), respectively. The same distributions of a single layer of InGaAs QDs (blue column) are used for comparison. (g)-(i) AFM images (1 μm $\times$ 1 μm) of the single layer, the dot A and the dot B, respectively.

few nm, especially for the larger ones [red bars in Fig. 4.23(b)]. When comparing the aspect ratio of the two dot layers an increase from (0.10 ± 0.03) nm to (0.12 ± 0.03) nm is found [see Fig. 4.23(c)].
This should be contrasted with the case of stack B. Because there has been no high temperature annealing step, a large amount of In is still floating on the surface after the first dot layer deposition, which leads to significantly larger surface dot compared to stack of type A. It can be seen in Fig. 4.23(d) that the average diameter has changed to (65 ± 13) nm and the dot height is no longer bimodal, but consists of a narrow dot distribution around (18.8 ± 4.0) nm in height [see Fig. 4.23(e)]. This narrowing of the dot distribution can be attributed to dot ripening [216] and highlights the large strain field existing in the barrier region, due to the dot size. The higher In amount content in the barrier region could also be explained by the thin GaAs cap layer, which leaves the top of the pyramids partially uncapped. The distribution of the aspect ratio for the dot B is also completely changed with an increase to (0.28 ± 0.05) nm, as shown in Fig. 4.23(f).
The AFM pictures in Figs. 4.23(g)-(i) show the three cases with the bimodal distributions for the single layer and the surface dots of stack A and the single distribution for stack B, respectively. The high density of small dots on the surface shown in Figs. 4.23(g) and 4.23(h) originates mainly during the cooling down of the sample at the end of the growth. This is a metastable state on the way to stable dot formation and can be due to the reduced thermal diffusivity of indium.

4.4.2. Strain-tunable QDM

The strain tunability of a single InGaAs QDM embedded in an n-i-p diode is demonstrated by using the setup reported in section 3.5.

Figure 4.24(b) shows the simultaneous effect of electric and strain fields on a representative QDM. The electric field values are obtained from the relation $F_d = (V_{bi} - V_d)/L$, where $L = 167$ nm is the thickness of the intrinsic layer with $V_{bi} = 2.05$ V and leakage current less than 1 nA for $V_d > 0$ [see Fig. 3.4(c)]. By sweeping the electric field across the diode from -6.5 to -14.4 kV/cm, with a level arm of $\Delta F_d L = 131.9$ meV, the X-shaped pattern of X^+ in a QDM [37] can be clearly observed.
The ACs circled in Fig. 4.24(b) have a magnitude (ΔE_{AC}) ranging between 0.2 and 0.4 meV, typical for hole tunnelling (see section 2.5.4). The excitonic energy levels as a function of the electric field are sketched in Fig. 4.24(c), following the configuration interaction method reported in Appendix A.1. Transitions between the initial (X^+) and the final (single hole) states have been considered. Two indirect transitions, $^{\underline{1}0}_{1\underline{1}}X^+$ and $^{\underline{1}0}_{2\underline{0}}X^+$, where electron and hole recombine in different dots, anticross two direct transitions, $^{\underline{1}0}_{2\underline{0}}X^+$ and $^{\underline{1}0}_{1\underline{1}}X^+$, where the recombination takes place in the same dot[1]. The characteristic X-shape of the pattern originates when there are anticrossings in both the initial and final states of the optical transition and there is a Coulomb energy difference of the electron-hole (e-h) attraction and hole-hole (h-h) repulsion between

[1]The upper (lower) numbers in the notation of the quantum states are the numbers of electrons (holes) in the bottom (B) and top (T) dot, respectively, and the underlines represent where the recombination takes place. See section 2.5.3 for details.

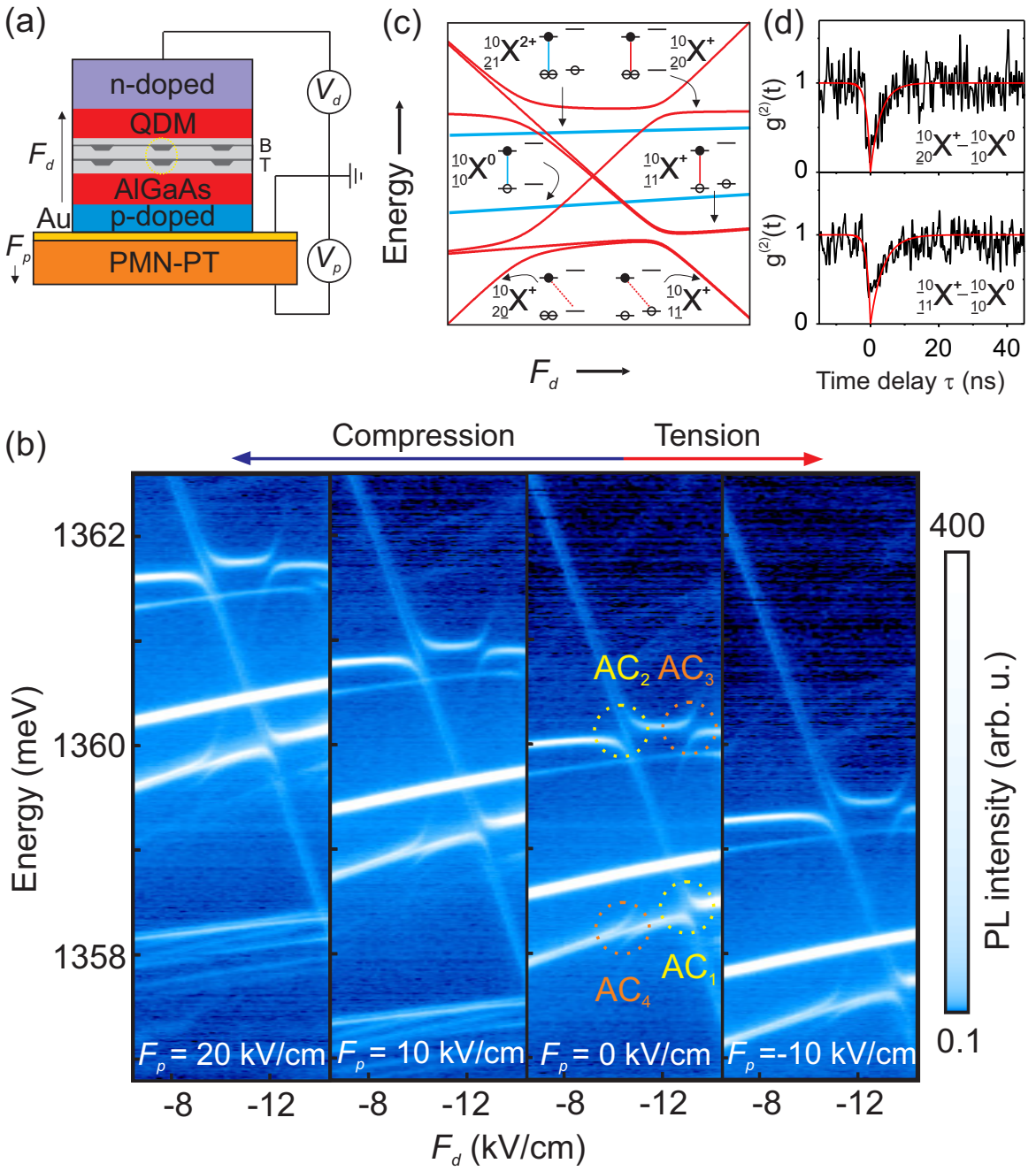

Figure 4.24.: (a) Sketch of the device with vertically stacked disk-shaped InGaAs QDs embedded in n-i-p nanomembranes integrated on top of a PMN-PT. (b) Colour-coded μ-PL maps of a representative QDM as a function of F_p and F_d (PL intensity in logarithmic scale). (c) Calculated transition energies of X^+ and X^0 excitons in a QDM. (d) Second-order correlation functions g^2(t) between $^{10}_{20}X^+$ (upper panel), $^{10}_{11}X^+$ (lower panel) and $^{10}_{10}X^0$, respectively. The red line is the fit of the ideal function. Figures (a)-(c) from Ref. [154].

$^{10}_{\underline{2}0}X^+$ and $^{10}_{\underline{1}1}X^+$. The AC_1 and AC_2 (see map at strain field $F_p = 0$ kV/cm) represent the anticrossing of $^{10}_{\underline{1}1}X^+$ and $^{10}_{\underline{2}0}X^+$ respectively with $^{10}_{\underline{1}\underline{1}}X^+$. The anticrossing of the direct trion recombinations with the weak transition $^{10}_{\underline{2}\underline{0}}X^+$, theoretically forbidden because of no holes in the final state but partially tunnel-induced in the experiment, is represented by the AC_3 and AC_4. Because of the optically very weak bonding branch of the AC_4, this will be considered in the following as the one formed by the anti-bonding branch and the central line.
A clear spin effect is visible by looking at AC_2. Due to Pauli blocking [98, 217], the lower branch of the AC represents a singlet-spin state. Since tunnelling is spin preserving, the line going through the AC is a spin-triplet configuration of the two holes in X^+, which cannot tunnel couple (see section 2.5.5).
Indirect transitions show more pronounced Stark shifts than direct excitons due to their larger static electric dipole (see section 2.5.3). From the slope of the energy of the indirect transitions with respect to F_d, an electron-hole average distance of ∼7 nm is inferred in reasonable agreement with the nominal centre-to-centre dot separation ($d = 8.5$ nm). Two additional direct recombination lines are observed in the spectra: the brightest line stems from the neutral exciton, $^{10}_{\underline{1}0}X^0$, and the weakest line from the doubly positively charged exciton, $^{10}_{\underline{2}1}X^{2+}$. From the slope of the direct transition in the bottom dot a permanent exciton dipole ∼0.48 e·nm is obtained, where the positive sign means that the electron wavefunction is shifted towards the dot apex, possibly due to In enrichment [218].

The polarised cross-correlation measurements between X^+ and X^0 are shown in Fig. 4.24(d). The setup is similar to the one described in section 4.1.2 with the two photon emitted by X^+ and X^0 detected respectively by the two APDs. The antibunching dip around $\tau = 0$ indicates that the $^{10}_{\underline{2}0}X^+$ (upper panel) or $^{10}_{\underline{1}1}X^+$ (lower panel) and the $^{10}_{\underline{1}0}X^0$ don't coexist in the QDM. The asymmetric shape measured for both configurations at positive (negative) τ values is due to the difference in the carrier population rate of the X^0 (X^+) after X^+ (X^0).
By fitting the measured data to an exponential law, the time constants for detection of $^{10}_{\underline{1}0}X^0$ before $^{10}_{\underline{2}0}X^+$ (upper panel) or before $^{10}_{\underline{1}1}X^+$ (lower panel) emissions are 1.12 ns and 1.01 ns, respectively, whereas the time constants for detection of $^{10}_{\underline{1}0}X^0$ after $^{10}_{\underline{2}0}X^+$ (upper panel) or after $^{10}_{\underline{1}1}X^+$ (lower panel) emissions are 2.95 ns and 3.73 ns, respectively. This is related to the dephasing time of the X^0, i.e., the damping lifetime due to fluctuating magnetic environment and charge fluctuations, which is longer in a QDM with respect to single QDs [40]. In fact, lifetimes of 1.36 ns and 1.07 ns have been measured, respectively, for the neutral and charged excitons in lens shaped single InGaAs/GaAs QDs [219].

The effect of biaxial stress on the QDMs can be studied by using the additional "tuning knob" in the device. The application of a voltage V_p on the piezo changes the spectrum significantly, as shown in Fig. 4.24(b). The PL emission lines blue-shift (red-shift) for positive (negative) F_p, due to compressive (tensile) strain, similar to the single-QD behaviour (see sections 4.1.2 and 4.2.2). At the same time compressive (tensile) strain pushes the ACs to higher (lower) F_d, as predicted in the work of Wang *et al.* [220]. The amount of in-plane strain transferred to the GaAs nanomembrane can

be estimated by comparison with previous work [145]. When F_p is swept through the whole tuning range ($\Delta F_p = 30$ kV/cm), the corresponding energy shift of the neutral exciton (ΔE_p) is about 2.4 meV and the strain transferred ∼0.06%.

4.4.3. Effect of strain field on the coupling strength

In this paragraph it will be investigated how the simultaneous application of strain and electric field to the single QDM affects the coupling strength.

Figures 4.25(a)-(d) show higher resolution μ-PL spectra of the same QDM described in the previous section. In particular, Figs. 4.25(a) and 4.25(b) represent the region of AC_1 at the highest and lowest value of compressive (−0.04%) and tensile (0.02%) strains F_p achieved in our device, respectively 20 kV/cm and −10 kV/cm. It is observed that application of compressive (tensile) strain leads to a reduction (increase) of the tunnel coupling. In fact, starting with a value of 187 μeV at $F_p = 0$ kV/cm, a linear increase of ΔE_{AC1} by 27 μeV for $\Delta E_p = 2.4$ meV is measured, as shown by the shift of the minima of the parabola in Fig. 4.25(e). The precise energy splitting (ΔE) between bonding and anti-bonding molecular states at a fixed F_d is obtained by two Lorentzian function manually centred at the brightest point of the two distributions.
The PL intensity of X^+ in this QDM (QDM 2 in table 4.2) at AC_1 and AC_2 positions for two extreme values of F_p (20 and −10 kV/cm) is shown in Figs. 4.26(a and b) and 4.26(c and d), respectively. The minimum energy splitting (ΔE_{AC}) is visible following the red continuous lines (guides to the eye). The PL intensities at AC_2 show the additional triplet peak (see section 2.5.5), which enhances the background noise in the AC region.

A more pronounced effect was measured for AC_2 with a tuning range of 48 μeV in the same interval of fields, as shown in Figs. 4.25(c, d, f) and the value at $F_p = 0$ kV/cm was 351 μeV. In conclusion, by varying the strain ΔE_{AC1} and ΔE_{AC2} can be modified by more than 14% within the range of F_p.
From the linear fit of the ACs as a function of ΔE_p [see Fig. 4.25(i)], a slope ratio $\alpha(AC_2)/\alpha(AC_1) = 1.9$ is obtained. This result is consistent with the coupling dynamics obtained by the formula

$$\Delta E_{AC2} = \sqrt{2}\Delta E_{AC1}\sqrt{1 + 2J_{eh}^2/\Delta E_{AC1}^2}, \tag{4.8}$$

as reported in section 2.5.5, where the singlet-triplet splitting $J_{eh} \sim 115$ μeV at $F_p = 0$ kV/cm is in the range of the values obtained in similar structures [211], and the factor $\sqrt{2}$ considers the tunnelling of two holes between the two dots. In fact, AC_1 represents the tunnelling of the single hole and AC_2 the tunnelling of the hole in presence of an e-h pair.
A similar strain effect on the AC energy gaps is measured on all the other anticrossings [see Fig. 4.25(i)]. For example, Figs. 4.25(g) and 4.25(h) show the parabolic behaviour of ΔE as a function of F_d around AC_3 and AC_4 at $F_p = 20$, 10, 0, −10 kV/cm. Starting with values at $F_p = 0$ kV/cm of 183 and 163 μeV, respectively, the total tuning ranges are 30 and 20 μeV. The energy values and the slope obtained from the linear fit for AC_3 are comparable with AC_1, underlining the similarity of the coupling mechanisms (see the table in Fig. 4.25). On the other hand, ΔE_{AC4} is much smaller than ΔE_{AC2} because ΔE_{AC4} represents the energy distance between the upper branch of the anticrossing

Anticrossing	AC_1	AC_2	AC_3	AC_4
Transition	$^{10}_{\underline{11}}X^+ \longleftrightarrow {}^{10}_{\underline{11}}X^+$	$^{10}_{\underline{20}}X^+ \longleftrightarrow {}^{10}_{\underline{11}}X^+$	$^{10}_{\underline{11}}X^+ \longleftrightarrow {}^{10}_{\underline{20}}X^+$	$^{10}_{\underline{20}}X^+ \longleftrightarrow {}^{10}_{\underline{20}}X^+$

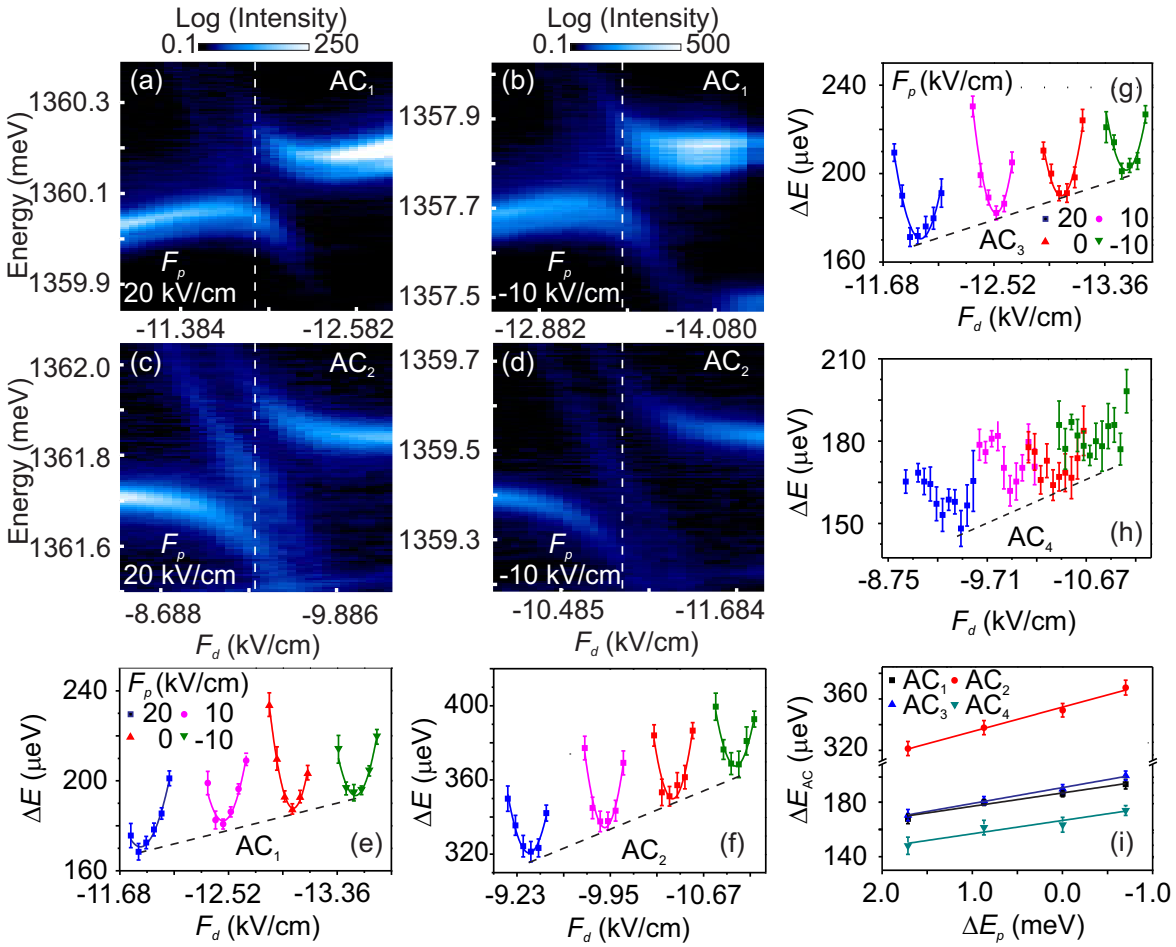

Figure 4.25.: Colour-coded μ-PL maps of the (a,b) AC_1 and (c,d) AC_2 regions as a function of F_d at $F_p = 20$ kV/cm (compressive strain, -0.04%) and $F_p = -10$ kV/cm (tensile strain, 0.02%), respectively. The dashed line marks the AC position. (e)-(h) Parabolic behaviour of the energy splitting (ΔE) between the bonding and anti-bonding molecular states around (e) AC_1, (f) AC_2, (g) AC_3, and (h) between the anti-bonding branch and the triplet line around AC_4 as a function of F_d at $F_p = 20$, 10, 0, -10 kV/cm. (i) Behaviour of ΔE_{AC} at AC_{1-4} as a function of the neutral exciton PL energy shift (ΔE_p), when F_p is varied through the whole tuning range ($\Delta F_p = 30$ kV/cm). The table (top) summarise the different anticrossings for the X^+ with the respective transitions. Figure readapted from Ref. [154].

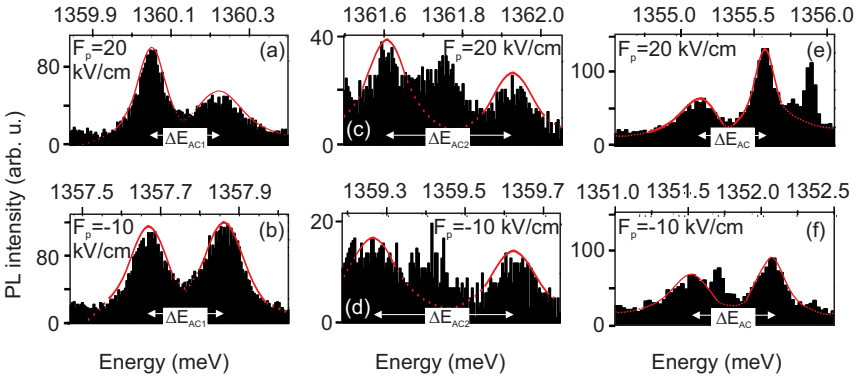

Figure 4.26.: PL intensity of QDM 2 at (a,b) AC_1 and (c,d) AC_2 positions for $F_p = 20$ and -10 kV/cm, respectively. (e,f) PL intensity of QDM 1 at (e) $F_p = 20$ kV/cm and (f) $F_p = -10$ kV/cm. The red continuous lines are guides to the eye. Figure readapted from Ref. [154]

and the central line.

Another effect of strain is visible by looking at Figs. 4.25(c) and 4.25(d). The triplet line that passes almost unaffected through AC_2 at the resonance point (see section 2.5.5) is no longer in the centre and its energy separation from the anti-bonding branch (higher energy component) is slightly increased. This reflects a different influence of strain on the triplet and singlet states, due to the overlap of the symmetric and antisymmetric part of the wavefunctions.

Other six QDMs chosen randomly in this device were measured and the strain tuning of the coupling strength gave very similar results, as shown in table 4.2.

QDM	1	2	3	4	5	6
ΔE_{AC} (μeV)	500	187	204	225	254	259
Tuning (μeV)	74	27	50	66	74	76

Table 4.2.: ΔE_{AC} at $F_p = 0$ kV/cm and the tuning of ΔE_{AC} in the range $F_p = 20$ to -10 kV/cm for six QDMs.

For example, after the same fitting procedure explained above, the ΔE_{AC} and its tuning for the QDM 1 are 500 μeV and 74 μeV, respectively. This is represented in Figs. 4.26(e) and 4.26(f) for two extreme values of F_p. The ΔE_{AC} fluctuates between different QDMs with an average value of (270 $\pm$ 120) μeV at $F_p = 0$ kV/cm. This is due to fluctuations over the size, shape and composition among the different QDs and it is related to the lack of control over the QD growth processes. On the other hand, the effect of the induced strain is quite similar for all the investigated QDMs, with an average value of change in ΔE_{AC} for the range of strain applied of (61 $\pm$ 19) μeV. Therefore, these data clearly demonstrate that the combination of strain and electric fields allows the coupling strength of the QDM to be actively manipulated.

Although in this work the maximum applied strain was 0.06%, a higher strain of up to 0.4% has been obtained using a different batch of piezo-electric substrates, as shown earlier in section 4.2. Assuming a linear relation between coupling strength and strain

(at large values of strain this is an underestimation because the non linear contributions will start to be significant), it would be possible to obtain the same predefined coupling strength for any QDM in our sample, since it would be possible to change the value of the AC energy gap by > 400 μeV, which is greater than the variation in AC energy gaps of the QDM ensemble. In order to support this assumption, $\mathbf{k}\cdot\mathbf{p}$ calculations (see section 2.2) have been made on a representative QDM with 8.5 nm dot centre-to-centre separation and $\Delta E_{\mathrm{AC}} = 284$ μeV. As a result, the coupling strength can be varied in the range $(124 - 395)$ μeV for -0.2% compressive strain to 0.2% tensile strain.

Relevant parameters of the QDM and their evolution upon application of stress can be extracted by describing the system with a modified Hamiltonian from the model reported in the work of Stinaff *et al.* [37], by taking into account the Stark shifts of the direct transitions. The transitions between the initial state with one electron and two holes ($\hat{\mathrm{H}}_{X^+}$) and the final state with a single hole ($\hat{\mathrm{H}}_h$) are considered, focusing on the four lines that anticross each other and neglecting the spin-exchange interaction (see Appendix A.1 for details).
The pattern is obtained by considering the two matrices (see section 2.5.3):

$$\hat{\mathrm{H}}_{X^+}^{(2\times2)} = \begin{pmatrix} \Gamma^{(-)} & -t_{X^+} \\ -t_{X^+} & -F'_d d^*_{X^+} \end{pmatrix}, \quad \hat{\mathrm{H}}_h = \begin{pmatrix} \epsilon_h & -t_h \\ -t_h & \epsilon_h - F'_d d^*_h \end{pmatrix}, \tag{4.9}$$

where $\hat{\mathrm{H}}_{X^+}^{(2\times2)}$ is the reduced Hamiltonian of the singlet states, $\Gamma^{(-)}$ is the energy distance between $\substack{10\\20}X^+$ and $\substack{10\\11}X^+$, $t = \Delta E_{\mathrm{AC}}/2$ is the tunneling rate, F'_d is the electric field ($F'_d = 0$ at AC_1), d^* is the effective interdot distance, and ϵ_h is the ground state energy of the hole.
By diagonalising the reduced matrix $\hat{\mathrm{H}}_{X^+}^{(2\times2)}$ of the initial state (X^+), the eigenvalues are:

$$E^{(i)}_{1,2} = \frac{-F'_d d^*_{X^+} + \Gamma^{(-)} \pm \sqrt{(F'_d d^*_{X^+} - \Gamma^{(-)})^2 + 4t^2_{X^+}}}{2}, \tag{4.10}$$

In the same way, the eigenvalues of the single hole matrix read:

$$E^{(f)}_{1,2} = \epsilon_h + \frac{-F'_d d^*_h \pm \sqrt{(F'_d d^*_h)^2 + 4t^2_h}}{2}. \tag{4.11}$$

Finally, the energy differences $E^{(i)}_{1,2} - E^{(f)}_{1,2}$ provide the pattern plotted in Fig. 4.27(b) at $F_p = -10$ kV/cm, which fits the experimental data in Fig. 4.27(a). The parameters used for fitting at different values of F_p are reported in table 4.3, where J_{eh} is indirectly calculated by the formula reported in section 2.5.5.
It is clear that under compression t_h, t_{X^+} and J_{eh} decrease linearly as a function of ΔE_p [see Fig. 4.27(c)]. Additional information is obtained by looking at the screening, that is the difference $d - d^*$, as a function of ΔE_p. This difference at $F_p = 0$ kV/cm is $\sim$11% larger for the initial state (X^+) with respect to the final state (single hole), because of the extra *e*-*h* pair. Moreover, $d - d^*$ slightly changes by the applied strain ($\sim$5% in the whole range of F_p).

In order to understand the physical origin of the observed changes in ΔE_{AC}, the

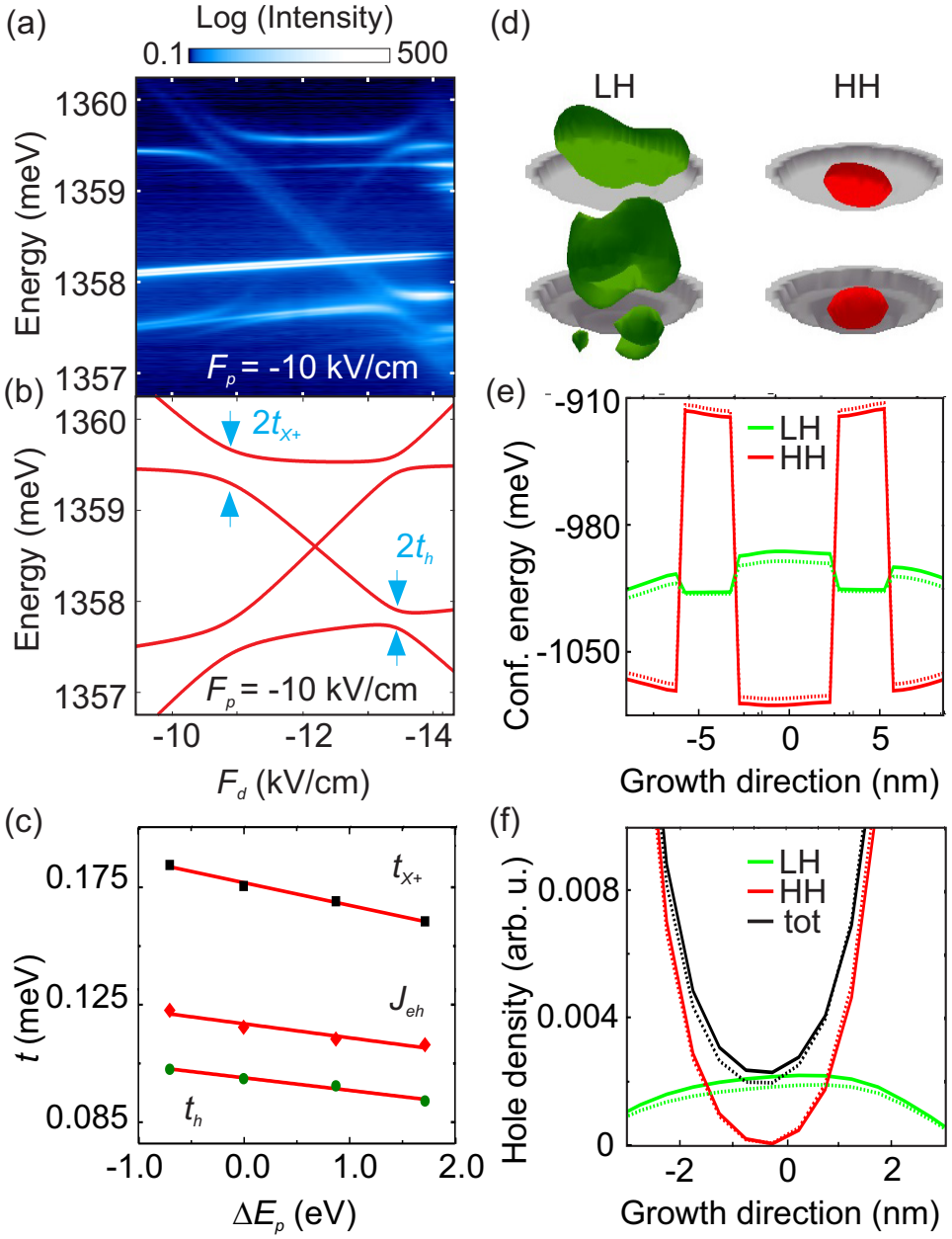

Figure 4.27.: (a) Colour-coded μ-PL map of a representative InGaAs/GaAs QDM (QDM 2 in table 4.2) as a function of F_d at $F_p = -10$ kV/cm. (b) Transition energies of X^+ in the QDM (AC lines) resulting from a fit to the experimental spectrum of (a). (c) Tunneling energies of single hole (t_h) and X^+ (t_{X^+}) and electron-hole exchange interaction (J_{eh}) as a function of ΔE_p, when F_p is varied in the whole range. (d) 3D hole probability density of LH (green) and HH (red) in the QDM (gray). The centre-to-centre dot separation is 8.5 nm. (e) Confinement potentials of LH (green) and HH (red) for the structure without (solid) and with induced compressive strain of $\varepsilon_{xx} = \varepsilon_{yy} = -0.1\%$ (dotted). Energy is displayed in electron view. (f) Hole probability density in the barrier region of LH (green), HH (red) and total (black) for the unstrained (solid) and strained (dotted) case. Figure from Ref. [154].

F_p (kV/cm)	t_h (μeV)	t_{X^+} (μeV)	J_{eh} (μeV)	d_h^* (nm)	$d_{X^+}^*$ (nm)	$\Gamma^{(-)}$ (meV)
-10	98	185	123	7.4	6.5	1.649
0	94	176	115	7.3	6.3	1.649
10	91	169	110	7.2	6.2	1.649
20	84	161	108	7.0	6.1	1.649

Table 4.3.: Parameters used to fit the experimental data at $F_p = -10, 0, 10, 20$ kV/cm. J_{eh} is indirectly obtained by the tunneling energies t_h and t_{X^+}.

electronic structure and the optical properties of the studied QDMs are calculated by V. Křápek using eight-band $\mathbf{k}\cdot\mathbf{p}$ method (see section 2.2), including a realistic description of the strain distribution and piezoelectric field [69, 221]. The model QDM consists of two identical lens shaped QDs with 3 nm of height and 15 nm of radius and a centre-to-centre dot separation of 8.5 nm. The $In_{0.3}Ga_{0.7}As$ QDs are embedded in pure GaAs surroundings. The structure is placed in the middle of the simulation area with the vertical extension of 31 nm and the lateral dimensions of 33 nm and discretised with a grid step of 0.5 nm. The calculation flow consists of the minimisation of the strain energy (continuum elasticity model), piezoelectric potential calculations involving the second order terms [221], and the eight-band envelope function model for the quantum states [69].
For the QDM 2 with $F_p = 0$ kV/cm, it is obtained a transition energy $\sim$1.37 eV for the neutral exciton, ΔE_{AC1} of 284 μeV, and a decrease in the tunnel coupling while sweeping the externally induced strain from tensile 0.02% to compressive -0.04% by 46 μeV, i.e., a relative change of 16%, in agreement with the experimental results. The small difference between the experimental and theoretical values for the emission energy and ΔE_{AC1} are explained by the strong dependence on structural parameters, in particular the thickness of the spacing layer. Figures 4.27(d) and 4.27(f) show the hole probability density for LH and HH. While the HH component is more localised at the dot position, the LH component dominates in the barrier region [100]. This can be explained by looking at the band edge of LHs in the GaAs barrier [see Fig. 4.27(e)] about 80 meV below the HH band edge, due to the local tensile strain induced by the QDs in the GaAs barrier region. The HHs penetrate the barrier region only by exponentially decaying tails at the QD boundaries, leaving negligible probability density in the barrier centre. The compressive strain increases the energy of LHs with respect to the HHs, leading to the reduction of the LH component in the barrier and therefore the tunnel coupling [see the dotted lines in Figs. 4.27(e) and 4.27(f)]. On the other hand, it is found that an opposite dependence of ΔE_{AC1} on strain can be obtained by reducing the centre-to-centre dot separation below 8 nm. This will promote the HHs in the barrier region, due to the decrease of the potential barrier and reduction of the LH weight, leading to an increase of tunnel coupling upon lateral compression.

4.4.4. Fine structure splitting

The study of the FSS in the QDMs is extremely interesting for discovering unique feature of these combinations and obtaining a deeper understanding of the spin in-

teractions in QDs. As explained in section 2.4.2 for X^0 in a single QD, the dark and bright states are separated by the *e-h* exchange interaction and this separation depends strongly on the overlap between the electron and hole wavefunctions. A more complex picture is observed in single QDMs. By using the PL setup shown in section 3.5 with a double spectrometer, polarisation resolved measurement of the positively charged and neutral excitons described in the previous sections are performed. The μ-PL map of emission energy as a function of voltage is reported in Figure 4.28(a), with the sketch of the direct transitions ${}^{10}_{11}X^+$, ${}^{10}_{10}X^0$, ${}^{10}_{21}X^{2+}$, and ${}^{10}_{20}X^+$ for the sake of clarity.

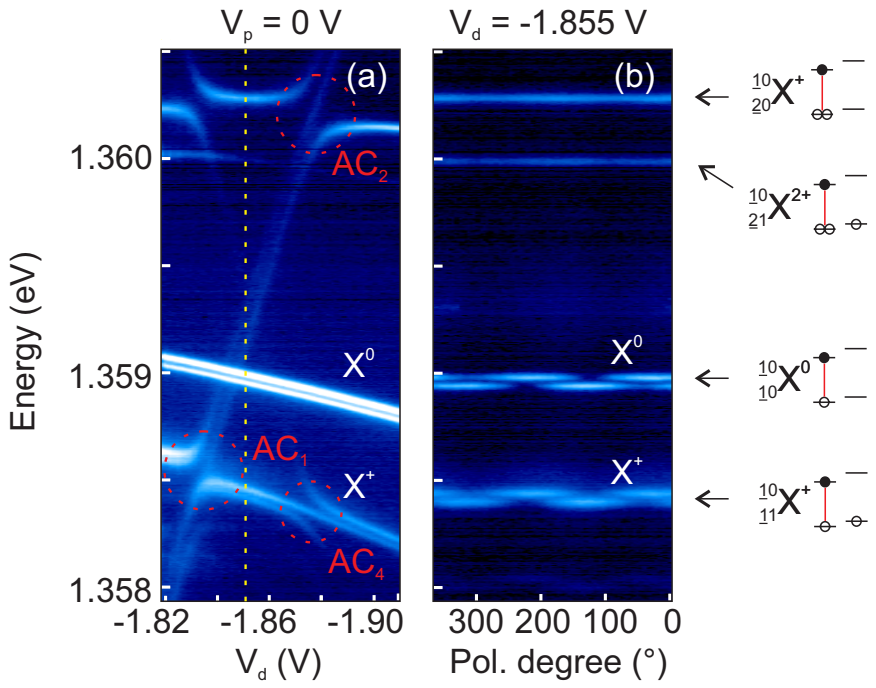

Figure 4.28.: Colour-coded μ-PL maps of QDM 2 (see table 4.2) as a function of (a) V_d and (b) polarisation angle (PL intensity in logarithmic scale). The yellow dashed line in (a) represents $V_d = 1.855$ V, where the map (b) is measured. The sketches on the right-hand side represent the direct transitions in X^+.

As expected, ${}^{10}_{10}X^0$ shows fine structure [see Fig. 4.28(b)], similar to the single QD case (see section 4.2.3). The behaviour of X^+ is more interesting: when the three carriers reside in the same dot (${}^{10}_{20}X^+$) or in the case of ${}^{10}_{21}X^{2+}$ there is no splitting, due to the full shell with spin singlet character (see section 2.5.5). However, in the case of ${}^{10}_{11}X^+$ the unpaired hole spin left, created by hole tunnelling into the other dot, results in a bright doublet structure. The *e-h* exchange interaction decays with the distance at least as $1/|\mathrm{r}|^3$ (some terms faster) and the remaining electron and hole ensure that the indirect trion behaves like a neutral exciton.
When the ${}^{10}_{20}X^+$ is observed through the anticrossing AC_2 [see Fig. 4.28(a)], a typical behaviour due to the contribution of both singlet and triplet states is seen (see section 2.5.5). The Pauli principle prevents the unpaired spins to tunnel resulting in a triplet state line with $m = 0$ that crosses the AC region. Mixing of the singlets and triplets via the *e-h* exchange interaction at the anticrossing produces the observed wig-

gling of the triplet line. For the total interaction both *e-h* and *h-h* exchanges should be taken into account (see section 2.5.5).

In the following, the discussion will focus on $^{10}_{10}X^0$ and $^{10}_{11}X^+$, which will be called X^0 and X^+, respectively. X^0 has a slightly larger FSS (s) and polarisation angle (θ) compared to X^+, with values for both around 40 μeV and 98°, respectively.
The evolution of the FSS and how the relative phase of the two different excitonic components with polarisation angle depends on the voltage on the diode (V_d) are investigated. By means of a Lorentzian fitting of the two bright excitonic states in the polarisation resolved PL spectra, s and θ of the oscillation for X^0 and X^+ have been obtained, as shown in Figs. 4.29(a and c) and 4.29(b and d), respectively.

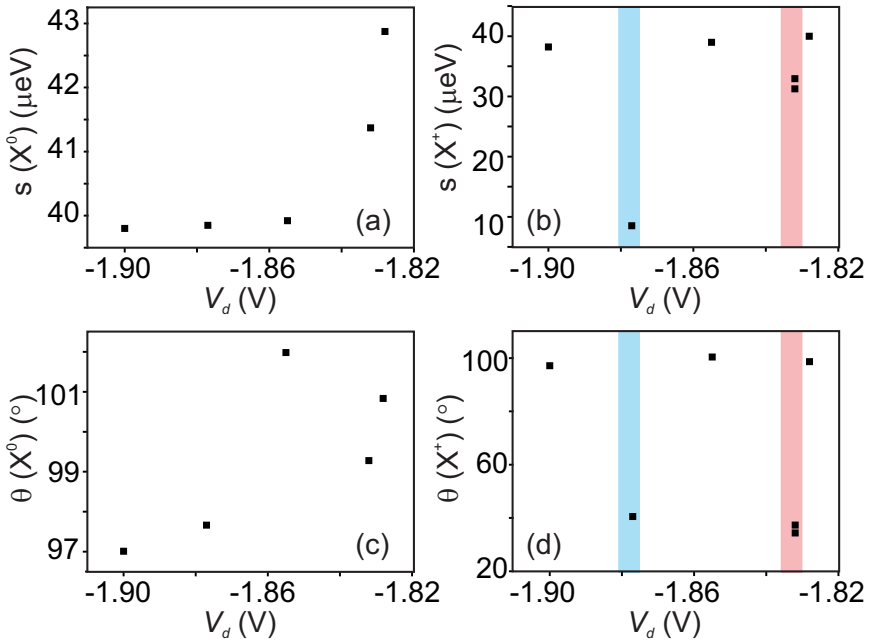

Figure 4.29.: s and θ as a function of V_d at $V_p = 0$ V for (a,b) $^{10}_{10}X^0$ and (c,d) $^{10}_{11}X^+$, respectively (for the sake of simplicity X^0 and X^+ in figure). The anticrossing regions AC_1 and AC_4 are highlighted in red and blue, respectively.

The amplitude of FSS and θ decrease by increasing the voltage, consistent with the behaviour of the single QD before the lower bound [149]. This can be explained by the effect of the electric field on the electron and hole wavefunctions, changing the *e-h* overlap, which in turn largely affects the long-range component of the exchange interaction (see section 2.4.2). In particular, X^0 is few μeV larger than X^+ and both vary in the range 43 to 38 μeV with the phase from 101° to 97°, when V_d increases from -1.9 to -1.828 V (the two excitonic states should have 90° phase difference in absence of external field applied).
Following X^+ through the anticrossing (AC_1) at $V_d = -1.832$ V even more reduction of s to 30 μeV and the phase to 35° [see red region of Figs. 4.29(b) and 4.29(d)] can be observed. A similar behaviour was measured in the work of Sköld *et al.* [222] for X^0 and can be explained by the weakened exchange interaction when the tunneling increases. In that case, the FSS was zero at the anticrossing, due to the two holes pulled

apart when the hole wavefunction moves from the bottom dot to the top dot. These small or negligible values for FSS render the QDMs very promising candidates for the generation of entangled-photon pairs [115]. At $V_d = -1.877$ V, the line going straight at AC_4 [see Fig. 4.28(a)] shows a small splitting by around 9 μeV with a phase $\sim 40°$ [see blue region of Figs. 4.29(b) and 4.29(d)]. This can be explained as a dark state-triplet that can couple with the bright excitonic states via the hole spin mixing [223].

Now the behaviour of s and θ, when the additional "tuning knob" on the piezo (V_p) is switched on, will be analysed. This is shown, respectively, in Figs. 4.30(a) and 4.30(c) for X^0.

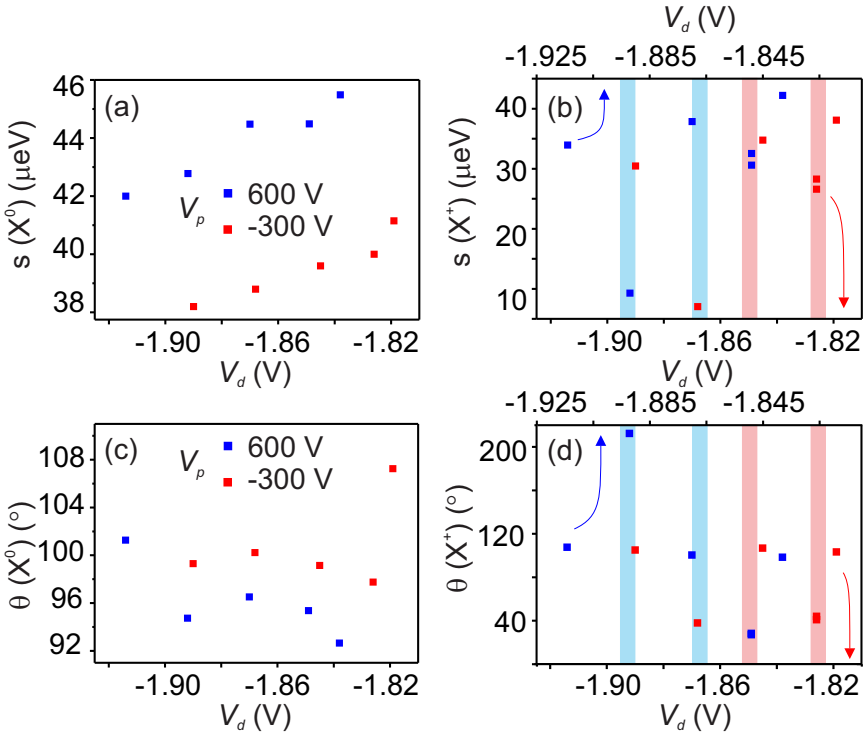

Figure 4.30.: s and θ as a function of V_d with $V_p = 600$ V (blue) and -300 V (red) for (a,c) $^{10}_{\bar{1}0}X^0$ and (b,d) $^{10}_{\bar{1}1}X^+$, respectively (for the sake of simplicity X^0 and X^+ in figure). The anticrossing regions AC_1 and AC_4 are highlighted in red and blue, respectively, and the double x-axes take into account the shift of the AC position by changing V_p.

The amplitude of the FSS increases and the phase decreases with compressive strain, as reported for the single QDs [149] for fields larger than the value at which s reaches a minimum. The doublet structure of $^{10}_{\bar{1}1}X^+$ also shows a splitting which increases with compressive strain [see Fig. 4.30(b)]. Moreover, compressive (tensile) strain pushes the ACs to lower (higher) voltages V_d, as reported at $V_p = 0$ V.
At the AC points, s and θ show marked dips with a decreasing by 25% and 60%, respectively [see red regions in Figs. 4.30(b) and 4.30(d)]. At AC_4, in particular, the phase change is very sensitive to the applied strain [see blue regions in Figs. 4.30(b) and 4.30(d)], e.g., θ decreases by 70° (from $\sim 110°$ to $\sim 40°$) for an applied tensile strain ($V_p = -300$ V) whereas it increases by 160° (from $\sim 40°$ to $\sim 200°$) for an applied compressive stress ($V_p = 600$ V). This could be a signature of the critical point, where

the polarisation direction is inverted, as shown for the single dot case in Fig. 4.13(b). The description confirms the possibility of manipulating the excitonic properties of QDMs via the simultaneous application of strain and electric fields, with the advantage of having $s \approx 0$ at the AC positions.

Finally, bright PL intensity of the X^0 and weaker for X^+ are observed. The low (I_L) and high (I_H) energy components increase with increasing compressive strain, as shown in Figs. 4.31(a) and (b) and 4.31(c) and (d), respectively, which is assigned to a change in the hole capture cross section [224].

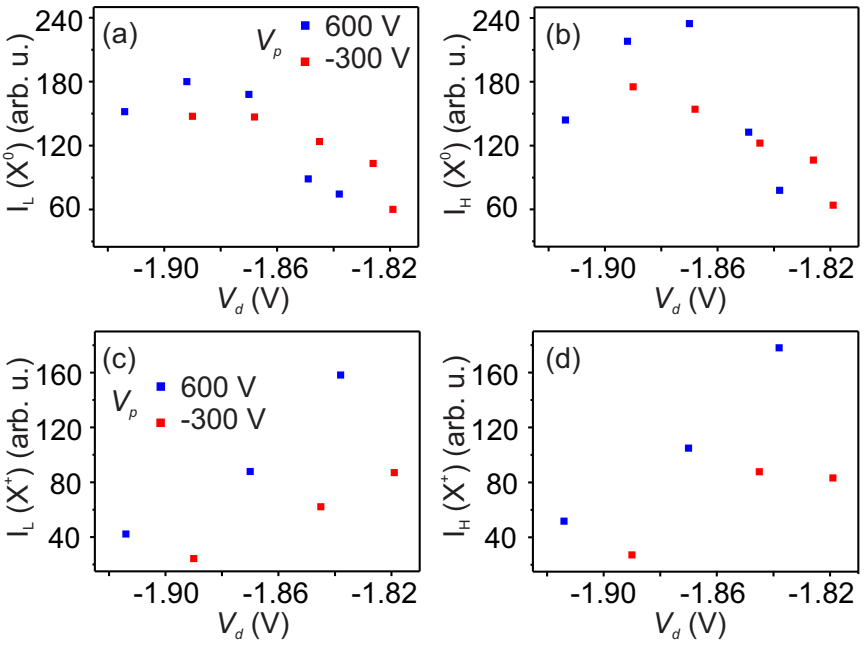

Figure 4.31.: PL integrated intensity for the (a,c) low and (b,d) high energy components as a function of V_d and V_p = 600 V (blue) and −300 V (red) for $^{10}_{\underline{10}}X^0$ and $^{10}_{\underline{11}}X^+$, respectively (for the sake of simplicity X^0 and X^+ in figure).

On the other hand, by applying lower voltages on the diode (V_d), the PL intensity for X^0 increases and for X^+ decreases. This difference could be explained by the tilt of the bands to the flat band position, where the recombination of the X^0 is favourable with respect of the X^+.

In conclusion, a strain tuneable InGaAs/GaAs QDM, where two vertically stacked QDs were embedded in the intrinsic region of an n-i-p nanomembrane diode integrated on a piezo-electric carrier substrate, is demonstrated. By a simultaneous application of electric and stress fields, the coupling strength can be actively tuned. The value of the AC energy gaps for hole tunneling, averaged over six molecules, is (270 ± 120) μeV at zero strain field with a strain-induced reduction of (61 ± 19) μeV. For example, the AC energies was varied by up to 27 μeV and 48 μeV for the single hole and the charged exciton, respectively. Eight-band $\mathbf{k}\cdot\mathbf{p}$ calculations reveal that the origin of the observed effect is a strain-induced modification of the HH and LH effective confinement potentials in the barrier and dot regions. The hole probability density changes in the barrier, leading to a reduction of the hole tunneling for compressive strain. The FSS of

the direct recombinations X^0 and X^+, with two holes in different dots, were measured. Electric and strain fields can tune the amplitude and phase in the QDM, similar to the QD case. The FSS amplitude and the phase decreases at the AC positions because of the separation of the carriers in the two dots, leading to a reduced electron-hole interaction. The PL intensity of both X^0 and X^+ show similar strain dependence with increasing counts by applying compressive strain, due to an increased electron-hole overlap that increases the radiative efficiency; opposite dependence was measure in the case of the electric field. This means that strain can reduce the electric field required to bring the states into resonance, enhancing the intensity around the anticrossing.

5. Conclusions

This work presents a study of single self-assembled QDs and QDMs, focusing on the effect that strain and electric fields have on their electronic and optical properties.

Single self-assembled QDs may become key elements for quantum computing and quantum key distribution since they are sources of single photons and, under certain conditions, can provide polarisation entangled photon pairs on demand and can be used as hosts of stationary qubits (electron or hole spins). The use of the XX-X cascade proposed by Benson et al. [14] for achieving entangled photon pair emission puts stringent requirements on the splitting of the intermediate X-state (FSS), which should be of the order of the emission linewidth [78]. This X-state splitting is due to the intrinsic strain and shape asymmetry of self assembled QDs. In order to reduce the splitting, an extraordinary precision and control of the epitaxial growth should be accompanied by a development of tuning and processing techniques, due to the natural inhomogeneous distribution of QD energy levels. Moreover, control of a combination of QDs, such as in QDMs, is the natural step towards the realisation of a scalable information processing device, requiring controllable tuning of the tunnelling rates of carriers. These two issues were addressed in this work together with a development of new fabrication strategies for as-grown nanostructures.

High quality GaAs/AlGaAs QDs with very low density $\sim (0.2 - 2.5)\times 10^8$ cm^{-2} and wavelength tuneable over a wide range of 200 meV have been demonstrated, based on the infilling nanoholes fabricated by droplet etching epitaxy with different GaAs amounts. A fine tuning to the ^{87}Rb D_2 absorption lines is obtained by means of magnetic and strain fields. An on-chip tuning technique for inducing strain in the dot layer has permitted the QD emission energy to be controllably varied over a spectral range exceeding 10 meV, comparable to the ensemble inhomogeneous broadening. This, together with the record single dot linewidth of 3.8 μeV, increases the yield of single photons that could be slowed down via a hybrid semiconductor-atomic interface.

A new device structure allowing the emission properties of InGaAs/GaAs QDs to be engineered by large electroelastic fields, provided by diode-like nanomembranes integrated onto piezoelectric actuators, has been presented. The two fields modify the interaction energies among electrons and holes in a different manner, allowing a reshaping of the QD electronic properties. The biexciton binding energy can be modified from a binding to an antibinding configuration without affecting the energy of the exciton transition, when the two external perturbations work one "against" the other. Most importantly, the simultaneous application of electric and elastic fields allows the control and cancellation of the exciton FSS in all the QDs measured. A simple theoretical model, which holds for every QD structure, was developed for supporting the experimental observations. The demonstration that virtually any QD can be used for the generation of entangled photons, featuring the highest degree of entanglement re-

ported to date for QD-based photon sources, with concurrence as high as 0.75 ± 0.02, from InGaAs/GaAs dots under applied electric and strain fields, has been shown.

Lateral or vertical combinations of two dots have been studied by developing new growth protocols and manufacturing new optoelectronic devices.

A robust method to grow low density lateral InGaAs/GaAs QD pairs using a template of nanoholes formed by droplet etching has been demonstrated. InAs migration towards the bottom of the nanohole leads to a locally enhanced growth rate and earlier dot formation at the hole site. The deposition of a thin GaAs buffer of between $(10 - 30)$ nm over the holes changes their shape, leading to the nucleation of QD pairs in each hole. As a result, up to 80% of nanoholes contain QD pairs following deposition of 1.3 ML and 1.6 ML at 490°C with an arsenic arrival flux of 0.6 ML/s. The QD pairs are aligned along the [110] direction and have centre-to-centre separation of ∼35 nm. From the infilling of the hole a net surface flux towards the hole of ∼7 times the incident flux is observed. Using a model based on the surface diffusion equation, the incorporation lifetime for indium in the nanohole is estimated to be ∼0.13 times that on a planar surface. For deposition amounts greater than 1.6 ML the dots of the QD pair coalesce. Increasing the substrate temperature does not significantly alter the dot distribution. However, the nanoholes partially collapse with increasing arsenic, due to mass transport as the substrate passes through a surface reconstruction transition. The μ-PL of capped QD pairs underlines good optical quality and a selective etching of the capping layer was used to confirm the double occupancy of the nanoholes.

Vertically aligned InGaAs/GaAs QDMs were embedded in the intrinsic region of an n-i-p nanomembrane diode, integrated on a piezoelectric substrate. For the first time, the simultaneous application of electric and strain fields allowed the coupling strength of hole tunnelling to be actively tuned. The average value of the anticrossing (AC) energy gaps is (270 ± 120) μeV at zero strain field with a strain-induced reduction of (61 ± 19) μeV. For example, the AC energy gaps were varied by up to 27 μeV and 48 μeV for the single hole and the charged exciton in a QDM, respectively. Eight-band $\mathbf{k}\cdot\mathbf{p}$ calculations reveal that the origin of the observed effect is a strain-induced modification of the HH and LH effective confinement potentials in the barrier and dot regions. The hole probability density changes in the barrier, leading to a reduction of the hole tunnelling for compressive strain.

In contrast to single QDs, charged excitons in QDMs can show FSS. This was measured for the positive trion, where the two holes are in separated dots and the recombination is in the same dot, and compared with the fine structure of the neutral exciton. The amplitude and the phase of FSS were tuned by a combination of electric and strain fields, similar to the QD case. In addition, their values decrease strongly at the AC positions because of the separation of the carriers in the two dots, leading to a reduced electron-hole interaction. The intensity of the light emitted from X^0 and X^+ increases on application of compressive strain, due to an increased electron-hole overlap that increases the radiative efficiency. On the other hand, the intensity increased (decreased) for X^0 (X^+) under application of a forward bias electric field due to increased carrier separation. This means that strain can reduce the electric field required to bring the states into resonance, enhancing the intensity around the anticrossing.

6. Outlook

The unprecedented control over the biexciton binding energy in InGaAs/GaAs QDs can be exploited for the fabrication of energy tunable sources of entangled photons via the time-reordering or the time-bin scheme [225]. This would pave the way towards entanglement swapping between distant QD-based qubits [164]. The concept of combining different external perturbations to achieve independent control of different QD parameters can also be exploited in the field of quantum communication, where quantum emitters with reconfigurable emission properties may be a fundamental requirement. Moreover, this device concept can be extended to QDs emitting at 1.3 or even 1.5 μm, leading to a significant increase of the number of QDs suitable for entangled photon generation at telecom wavelengths.
By taking advantage of the droplet etching epitaxy, it can be finally possible to realise GaAs/AlGaAs QDMs infilling the nanoholes with two layers of GaAs separated by a thin layer of AlGaAs. The advantage of this structure is the absence of the inherent strain, which leads to composition gradient in the dot and set limits to the dot sizes in InGaAs/GaAs QDMs. Remarkably, the smaller nuclear spin moment of gallium compared with indium suggests that GaAs/AlGaAs QDs and QDMs could be preferable for spin physics. For example, the use of strain-free GaAs/AlGaAs QDs [163, 187] may yield even larger entanglement levels due to the reduced nuclear magnetic fields and associated fluctuations.
The lateral geometry of InGaAs/GaAs QD pairs can be extended to more QDs, which can be coupled independently via a top gate over the QDM.
The demonstrated strain control of the coupling strength in QDMs may pave the way to a precise and flexible control of the entanglement between solid-state spin qubits in optically active QDMs. When combined with fast electric pulses [87] it may allow the Landau-Zener transition from one AC branch to the other to be studied, since this transition increases exponentially as the coupling strength is decreased. In this way, target QDM states inaccessible with only one field can be explored and the desired delocalised QDM states can be both initialised and read-out. Moreover, the effect of the HHs in the barrier region can be investigated by reducing the centre-to-centre dot separation below 8 nm, since $\mathbf{k}\cdot\mathbf{p}$ calculations showed opposite dependence in the AC energy gaps on strain.

A. Appendix

A.1. Theoretical description of trion states in QDMs

Trion states in QDMs are calculated with a configuration interaction method using a Hamiltonian of Ref. [98]. Since it should be investigated the effect of the strain on the coupling strength, the system has been simplified by neglecting the spin exchange interactions ($J_{eh} = 0$) for the fine structure of the PL map (only the contribution to the tunnelling energies have been considered). In order to take into account the Stark shift of the direct transitions, a different interdot effective distance d^* for the initial (X^+) and the final (single hole) states has been introduced. The H_{11} term of the initial state can be decoupled from the system because the energy range is far from the region of interest. In this way the three triplet states are decoupled and the reduced 2×2 matrix of the singlet states is left, where H_{22} reads $\Gamma^{(-)} = V^{hh}_{BBBB} - V^{eh}_{BBBB} - V^{hh}_{BBTT} + V^{eh}_{BBTT}$ and $V^{hh}_{BTBT} \sim 0$. The Coulomb terms are

$$V^{\alpha,\beta}_{ijkl} = \pm \int d\mathbf{r}d\mathbf{r}'|\mathbf{r} - \mathbf{r}'|\phi^{\alpha*}_i(\mathbf{r})\phi^{\beta*}_{\mathbf{k}}(\mathbf{r}')\phi^{\alpha}_{\mathbf{j}}(\mathbf{r})\phi^{\beta}_{\mathbf{l}}(\mathbf{r}'), \tag{A.1}$$

where ϕ^{α}_i is the orthonormalized wavefunction of particle α in dot i.

The Hamiltonian of the final state, constituted of a single hole in the bottom or top dot, reads

$$\hat{\mathrm{H}}_h = \begin{pmatrix} \epsilon_h & -t_h \\ -t_h & \epsilon_h - F'_d d^*_h \end{pmatrix}, \tag{A.2}$$

where ϵ_h is the ground state confinement energy of the hole and $t_h = \langle \phi^h_B | \hat{\mathrm{H}}^h | \phi^h_T \rangle$ is the hole tunnelling matrix.
By diagonalising the reduced matrix $\hat{\mathrm{H}}^{(2\times2)}_{X^+}$ of the initial state (X^+) and of the single hole 4.4.3, the eigenvalues reported in the equations 4.10 and 4.11, respectively, are obtained.
The four PL transitions of Fig. 3(b) in the main text are calculated by the differences

$E_{1,2}^{(i)} - E_{1,2}^{(f)}$:

$$\begin{aligned}
E_2^{(i)}\text{-}E_1^{(f)} &= \text{-}\epsilon_h\text{-}\frac{\text{-}F'_d(d^*_h\text{-}d^*_{X^+})\text{-}\Gamma^{(-)}+\sqrt{(F'_d d^*_h)^2+4t_h^2}+\sqrt{(F'_d d^*_{X^+}\text{-}\Gamma^{(-)})^2+4t_{X^+}^2}}{2};\\
E_1^{(i)}\text{-}E_1^{(f)} &= \text{-}\epsilon_h\text{-}\frac{\text{-}F'_d(d^*_h\text{-}d^*_{X^+})\text{-}\Gamma^{(-)}+\sqrt{(F'_d d^*_h)^2+4t_h^2}\text{-}\sqrt{(F'_d d^*_{X^+}\text{-}\Gamma^{(-)})^2+4t_{X^+}^2}}{2};\\
E_2^{(i)}\text{-}E_2^{(f)} &= \text{-}\epsilon_h\text{-}\frac{\text{-}F'_d(d^*_h\text{-}d^*_{X^+})\text{-}\Gamma^{(-)}\text{-}\sqrt{(F'_d d^*_h)^2+4t_h^2}+\sqrt{(F'_d d^*_{X^+}\text{-}\Gamma^{(-)})^2+4t_{X^+}^2}}{2};\\
E_1^{(i)}\text{-}E_2^{(f)} &= \text{-}\epsilon_h\text{-}\frac{\text{-}F'_d(d^*_h\text{-}d^*_{X^+})\text{-}\Gamma^{(-)}\text{-}\sqrt{(F'_d d^*_h)^2+4t_h^2}\text{-}\sqrt{(F'_d d^*_{X^+}\text{-}\Gamma^{(-)})^2+4t_{X^+}^2}}{2}.
\end{aligned} \tag{A.3}$$

ΔE_{AC2} is obtained from the minimum of the difference between equations. A.3 and A.3:

$$\Delta E_{\mathrm{AC2}} = 2t_{X^+}, F'_d = \frac{\Gamma^{(-)}}{d^*_{X^+}}. \tag{A.4}$$

In the same way for the other ACs:

$$\Delta E_{\mathrm{AC1}} = \Delta E_{\mathrm{AC3}} = 2t_h, F'_d = 0; \tag{A.5}$$

$$\Delta E_{\mathrm{AC4}} = \Delta E_{\mathrm{AC2}} = 2t_{X^+}, F'_d = \frac{\Gamma^{(-)}}{d^*_{X^+}}. \tag{A.6}$$

Finally, it is possible to calculate the electric field at the crossing point of the X-shaped pattern by equating equations A.3 and A.3:

$$F'_d = \frac{-d^*_{X^+}\Gamma^{(-)} + \sqrt{(d^*_h\Gamma^{(-)})^2 + 4(d^{*2}_h - d^{*2}_{X^+})(t^2_{X^+} - t^2_h)}}{d^{*2}_h - d^{*2}_{X^+}}. \tag{A.7}$$

Bibliography

[1] M. Planck, *Zur Theorie des Gesetzes der Energieverteilung im Normalspektrum*, Deutsche Physikalische Gesellschaft. Verhandlungen **2**, 237-245 (1900).

[2] A. Einstein, B. Podolsky, and N. Rosen, *Can quantum mechanical description of physical reality be considered complete?*, Phys. Rev. **47**, 777-780 (1935).

[3] R. P. Feynman, *Quantum mechanical computers*, Optics News, 1985; Reprinted in: Foundations Phys. **16**, 507-531 (1986).

[4] P. W. Shor, *Polynomial-time algorithms for prime factorization and discrete logarithms on a quantum computer*, SIAM J. Comp. **26**, 1484-1509 (1997).

[5] C. H. Bennett and D. P. DiVincenzo, *Quantum information and computation*, Nature **404**, 247-255 (2000).

[6] A. Schliwa, M. Winkelnkemper, and D. Bimberg, *Few-particle energies versus geometry and composition of $In_xGa_{1-x}As/GaAs$ self-organized quantum dots*, Phys. Rev. B **79**, 075443 (2009).

[7] P. Michler, A. Kiraz, C. Becher, W. V. Schoenfeld, P. M. Petroff, L. Zhang, E. Hu, and A. Imamoğlu, *A quantum dot single-photon turnstile device*, Science **290**, 2282-2285 (2000).

[8] C. L. Salter, R. M. Stevenson, I. Farrer, C. A. Nicoll, D. A. Ritchie, and A. J. Shields, *An entangled-light-emitting diode*, Nature **465**, 594-597 (2010).

[9] D. Englund, A. Faraon, I. Fushman, N. Stoltz, P. M. Petroff, and J, Vučković, *Controlling cavity reflectivity with a single quantum dot*, Nature **450**, 857-861 (2007).

[10] N. N. Ledentsov, *Quantum dot laser*, Semicond. Sci. Technol. **26**, 014001 (2011).

[11] B. D. Gerardot, D. Brunner, P. A. Dalgarno, P. Öhberg, S. Seidl, M. Kroner, K. Karrai, N. G. Stoltz, P. M. Petroff, and R. J. Warburton, *Optical pumping of a single hole spin in a quantum dot*, Nature **451**, 441-444 (2008).

[12] M. Atatüre, *Quantum-dot spin-state preparation with near-unity fidelity*, Science **312**, 551-553 (2006).

[13] S. Rodt, R. Heitz, A. Schliwa, R. L. Sellin, F. Guffarth, and D. Bimberg, *Repulsive exciton-exciton interaction in quantum dots*, Phys. Rev. B **68**, 035331 (2003).

[14] O. Benson, C. Santori, M. Pelton, and Y. Yamamoto, *Regulated and entangled photons from a single quantum dot*, Phys. Rev. Lett. **84**, 2513 (2000).

[15] D. P. DiVincenzo, *Quantum computation*, Science **270**, 255-261 (1995).

[16] A. Imamoğlu, D. D. Awschalom, G. Burkard, D. P. DiVincenzo, D. Loss, M. Sherwin and A. Small, *Quantum information processing using quantum dot spins and cavity QED*, Phys. Rev. Lett. **83**, 4204 (1999).

[17] A. J. Shields, *Semiconductor quantum light sources*, Nature Photon. **1**, 215-223 (2007).

[18] K. De Greve, L. Yu, P. L. McMahon, J. S. Pelc, C. M. Natarajan, N. Y. Kim, E. Abe, S. Maier, C. Schneider, M. Kamp, S. Höfling, R. H. Hadfield, A. Forchel, M. M. Fejer, and Y. Yamamoto, *Quantum-dot spin-photon entanglement via frequency downconversion to telecom wavelength*, Nature **491**, 421-425 (2012).

[19] W. B. Gao, P. Fallahi, E. Togan, J. Miguel-Sanchez, and A. Imamoğlu, *Observation of entanglement between a quantum dot spin and a single photon*, Nature **491**, 426-430 (2012).

[20] R. J. Young, R. M. Stevenson, P. Atkinson, K. Cooper, D. A. Ritchie, and A. J. Shields, *Improved fidelity of triggered entangled photons from single quantum dots*, New J. Phys. **8**, 29 (2006).

[21] N. Akopian, N. H. Lindner, E. Poem, Y. Berlatzky, J. Avron, D. Gershoni, B. D. Gerardot, and P. M. Petroff, *Entangled photon pairs from semiconductor quantum dots*, Phys. Rev. Lett. **96**, 130501 (2006).

[22] R. M. Stevenson, R. J. Young, P. Atkinson, K. Cooper, D. A. Ritchie, and A. J. Shields, *A semiconductor source of triggered entangled photon pairs*, Nature **439**, 179-182 (2006).

[23] N. Akopian, L. Wang, A. Rastelli, O. G. Schmidt, and V. Zwiller, *Slowing down single photons from a quantum dot in a rubidium vapour cell*, Nature Photon. **5**, 230-233 (2011).

[24] X. Li, Y. Wu, D. Steel, D. Gammon, T. H. Stievater, D. S. Katzer, D. Park, C. Piermarocchi, and L. J. Sham, *An all-optical quantum gate in a semiconductor quantum dot*, Science **301**, 809-811 (2003).

[25] G. Schedelbeck, W. Wegscheider, M. Bichler, and G. Abstreiter, *Coupled quantum dots fabricated by cleaved edge overgrowth: from artificial atoms to molecules*, Science **278**, 1792-1795 (1997).

[26] T. Hatano, M. Stopa, and S. Tarucha, *Single-electron delocalization in hybrid vertical-lateral double quantum dots*, Science **309**, 268-271 (2005).

[27] J. R. Petta, A. C. Johnson, J. M. Taylor, E. A. Laird, A. Yacoby, M. D. Lukin, C. M. Marcus, M. P. Hanson, and A. C. Gossard, *Coherent manipulation of coupled electron spins in semiconductor quantum dots*, Science **309**, 2180-2184 (2005).

[28] D. Loss and D. P. DiVincenzo, *Quantum computation with quantum dots*, Phys. Rev. A **57**, 120 (1998).

[29] L. Robledo, J. Elzerman, G. Jundt, M. Atatüre, A. Högele, S. Fält, and A. Imamoğlu, *Conditional dynamics of interacting quantum dots*, Science **320**, 772-775 (2008).

[30] J. Stangl, V. Hol, and G. Bauer, *Structural properties of self-organized semiconductor nanostructures*, Rev. Mod. Phys. **76**, 725 (2004).

[31] Q. Xie, A. Madhukar, P. Chen, and N. P. Kobayashi, *Vertically self-organized InAs quantum box islands on GaAs(100)*, Phys. Rev. Lett. **75**, 2542 (1995).

[32] G. S. Solomon, J. A. Trezza, A. F. Marshall, and J. S. Harris, *Vertically aligned and electronically coupled growth induced InAs islands in GaAs*, Phys. Rev. Lett. **76**, 952 (1996).

[33] A. S. Bracker, M. Scheibner, M. F. Doty, E. A. Stinaff, I. V. Ponomarev, J. C. Kim, L. J. Whitman, T. L. Reinecke, and D. Gammon, *Engineering electron and hole tunneling with asymmetric InAs quantum dot molecules*, Appl. Phys. Lett. **89**, 233110 (2006).

[34] M. Bayer, P. Hawrylak, K. Hinzer, S. Fafard, M. Korkusinski, Z. R. Wasilewski, O. Stern, and A. Forchel, *Coupling and entangling of quantum states in quantum dot molecules*, Science **291**, 451-453 (2001).

[35] H. J. Krenner, M. Sabathil, E. C. Clarke, A. Kress, D. Schuh, M. Bichler, G. Abstreiter, and J. J. Finley, *Direct observation of controlled coupling in an individual quantum dot molecule*, Phys. Rev. Lett. **94**, 057402 (2005).

[36] G. Ortner, M. Bayer, Y. Lyanda-Geller, T. L. Reinecke, A. Kress, J. P. Reithmaier, and A. Forchel, *Control of vertically coupled InGaAs/GaAs quantum dots with electric fields*, Phys. Rev. Lett. **94**, 157401 (2005).

[37] E. A. Stinaff, M. Scheibner, A. S. Bracker, I. V. Ponomarev, V. L. Korenev, M. E. Ware, M. F. Doty, T. L. Reinecke, and D. Gammon, *Optical signatures of coupled quantum dots*, Science **311**, 636-639 (2006).

[38] D. Kim, S. G. Carter, A. Greilich, A. S. Bracker, and D. Gammon, *Ultrafast optical control of entanglement between two quantum-dot spins*, Nature Phys. **7**, 223-229 (2011).

[39] G. Cao, H.-O. Li, T. Tu, L. Wang, C. Zhou, M. Xiao, G.-C. Guo, H.-W. Jiang, and G.-P. Guo, *Ultrafast universal quantum control of a quantum-dot charge qubit using Landau-Zener-Stückelberg interference*, Nature Comm. **4**, 1401 (2013).

[40] K. M. Weiss, J. M. Elzerman, Y. L. Delley, J. Miguel-Sanchez, and A. Imamoğlu, *Coherent two-electron spin qubits in an optically active pair of coupled InGaAs quantum dots*, Phys. Rev. Lett. **109**, 107401 (2012).

[41] M. Khoshnegar, A. Jafari-Salim, M. H. Ansari, and A. H. Majedi, *Toward tripartite hybrid entanglement in quantum dot molecules*, New J. Phys. **16**, 023019 (2014).

[42] R. J. Keyes and T. M. Quist, *Injection luminescent pumping of CaF_2:U^{3+} with GaAs diode lasers*, Appl. Phys. Lett. **4**, 50 (1964).

[43] R. D. Dupuis and P. D. Dapkus, *Continuous room temperature operation of $Ga_{(1-x)}Al_xAs$-GaAs double-heterostructure lasers grown by metalorganic chemical vapor deposition*, Appl. Phys. Lett. **32**, 406 (1978).

[44] O. Zitouni, K. Boujdaria, and H. Bouchrina, *Band parameters for GaAs and Si in the 24-k·p model*, Semicond. Sci. Technol. **20**, 908 (2005).

[45] G. Burkard, *Quantum information: Positively spin coherent*, Nat. Mater. **7**, 100-101 (2008).

[46] M. Bayer, G. Ortner, O. Stern, A. Kuther, A. A. Gorbunov, A. Forchel, P. Hawrylak, S. Fafard, K. Hinzer, T. L. Reinecke, S. N. Walck, J. P. Reithmaier, F. Klopf, and F. Schafer, *Fine structure of neutral and charged excitons in self-assembled In(Ga)As/(Al)GaAs quantum dots*, Phys. Rev. B. **65**, 195315 (2002).

[47] *Physics of group IV elements and III-V compounds*, Vol. 17a of Landolt-Böornstein tables, edited by O. Madelung, M. Schultz, and H. Weiss, (Springer, Berlin, 1982).

[48] H. W. van Kesteren, E. C. Cosman, W. A. J. A. van der Poel, and C. T. Foxon. *Fine structure of excitons in type-II GaAs/AlAs quantum wells*, Phys. Rev. B **41**, 5283 (1990).

[49] V. Křápek, *Excitonic structure of absorption edge in quantum dots*, PhD thesis (2008).

[50] S. L. Chuang, *Physics of photonic devices*, 2nd edition (Wiley, New York, 2009).

[51] P. Yu and M. Cardona, *Fundamentals of semiconductors: Physics and materials properties* (Springer, Berlin, 2005).

[52] Y. Sun, S. E. Thompson, and T. Nishida, *Strain effect in semiconductors: theory and device applications* (Springer, London, 2010).

[53] G. E. Pikus and G. L. Bir, *Symmetry and strain induced effects in semiconductors* (Wiley, New York, 1974).

[54] D. Bimberg, M. Grundmann, and M. M. Ledenstov, *Quantum dot heterostructures* (Wiley, Chichester, 1999).

[55] http://www.ioffe.ru/SVA/NSM/Semicond/GaAs.

[56] S. Sanguinetti, M. Henini, M. Grassi Alessi, M. Capizzi, P. Frigeri, and S. Franchi, *Carrier thermal escape and retrapping in self-assembled quantum dots*, Phys. Rev. B **60**, 8276 (1999).

[57] P. Borri, W. Langbein, S. Schneider, U. Woggon, R. L. Sellin, D. Ouyang, and D. Bimberg, *Ultralong dephasing time in InGaAs quantum dots*, Phys. Rev. Lett. **87**, 157401 (2001).

[58] J. H. Davies, *The physics of low-dimensional semiconductors* (Cambridge University Press, 1998).

[59] G. W. Bryant and G. S. Solomon, *Optics of quantum dots and wires* (Artech House, Boston, 2005).

[60] C. Weisbuch and B. Vinter, *Quantum semiconductor structures* (Academic Press, Inc., San Diego, 1991).

[61] N. N. Ledentsov, J. Böhrer, M. Beer, F. Heinrichsdorff, M. Grundmann, D. Bimberg, S. V. Ivanov, B. Ya. Meltser, S. V. Shaposhnikov, I. N. Yassievich, N. N. Faleev, P. S. Kop'ev, and Zh. I. Alferov, *Radiative states in type-II GaSb/GaAs quantum wells*, Phys. Rev. B **52**, 14058 (1995).

[62] A. D. Yoffe, *Semiconductor quantum dots and related systems: electronic, optical, luminescence and related properties of low dimensional systems*, Adv. Phys. **50**, 1 (2001).

[63] *Single quantum dots: fundamentals, applications and new concepts*, edited by P. Michler (Springer, Berlin, 2003).

[64] W. Langbein, P. Borri, U. Woggon, V. Stavarache, D. Reuter, and A. D. Wieck, *Control of fine-structure splitting and biexciton binding in $In_xGa_{1-x}As$ quantum dots by annealing*, Phys. Rev. B **69**, 161301(R) (2004).

[65] A. Schliwa, M. Winkelnkemper and D. Bimberg, *Impact of size, shape, and composition on piezoelectric effects and electronic properties of In(Ga)As/GaAs quantum dots*, Phys. Rev. B **76**, 205324 (2007).

[66] H. D. Robinson and B. B. Goldberg, *Light-induced spectral diffusion in single self-assembled quantum dots*, Phys. Rev. B **61**, 5086(R) (2000).

[67] G. A. Narvaez, G. Bester, and A. Zunger, *Pressure effects on neutral and charged excitons in self-assembled (In,Ga)As/GaAs quantum dots*, Phys. Rev. B **72**, 041307(R) (2005).

[68] G. Bester, S. Nair, and A. Zunger, *Pseudopotential calculation of the excitonic fine structure of million-atom self-assembled $In_{1-x}Ga_xAs/GaAs$ quantum dots*, Phys. Rev. B **67**, 161306(R) (2003).

[69] O. Stier, M. Grundmann, and D. Bimberg, *Electronic and optical properties of strained quantum dots modeled by 8-band k·p theory*, Phys. Rev. B **59**, 5688 (1999).

[70] E. Blackwood, M. J. Snelling, R. T. Harley, S. R. Andrews, and C. T. B. Foxon, *Exchange interaction of excitons in GaAs heterostructures*, Phys. Rev. B **50**, 14246 (1994).

[71] D. Gammon, E. S. Snow, B. V. Shanabrook, D. S. Katzer, and D. Park, *Fine structure splitting in the optical spectra of single GaAs quantum dots*, Phys. Rev. Lett. **76**, 3005 (1996).

[72] R. J. Young, R. M. Stevenson, A. J. Shields, P. Atkinson, K. Cooper, D. A. Ritchie, K. M. Groom, A. I. Tartakovskii, and M. S. Skolnick, *Inversion of exciton level splitting in quantum dots*, Phys. Rev. B **72**, 113305 (2005).

[73] S. Malik, C. Roberts, R. Murray, and M. Pate, *Tuning self-assembled InAs quantum dots by rapid thermal annealing*, Appl. Phys. Lett. **71**, 1987 (1997).

[74] S. Sanguinetti, T. Mano, A. Gerosa, C. Somaschini, S. Bietti, N. Koguchi, E. Grilli, M. Guzzi, M. Gurioli, and M. Abbarchi, *Rapid thermal annealing effects on self-assembled quantum dot and quantum ring structures*, J. Appl. Phys. **104**, 113519 (2008).

[75] J. P. Reithmaier, G. Sęk, A. Löffler, C. Hofmann, S. Kuhn, S. Reitzenstein, L. V. Keldysh, V. D. Kulakovskii, T. L. Reinecke, and A. Forchel, *Strong coupling in a single quantum dot-semiconductor microcavity system*, Nature **432**, 197-200 (2004).

[76] B. D. Gerardot, S. Seidl, P. A. Dalgarno, R. J. Warburton, D. Granados, J. M. Garcia, K. Kowalik, O. Krebs, K. Karrai, A. Badolato, and P. M. Petroff, *Manipulating exciton fine structure in quantum dots with a lateral electric field*, Appl. Phys. Lett. **90**, 041101 (2007).

[77] S. Seidl, M. Kroner, A. Högele, K. Karrail, R. J. Warburton, A. Badolato, and P. M. Petroff, *Effect of uniaxial stress on excitons in a self-assembled quantum dot*, Appl. Phys. Lett. **88**, 203113 (2006).

[78] A. Muller, W. Fang, J. Lawall, and G. S. Solomon, *Creating polarization-entangled photon pairs from a semiconductor quantum dot using the optical stark effect*, Phys. Rev. Lett. **103**, 217402 (2009).

[79] M. M. Vogel, S. M. Ulrich, R. Hafenbrak, P. Michler, L. Wang, A. Rastelli, and O. G. Schmidt, *Influence of lateral electric fields on multiexcitonic transitions and fine structure of single quantum dots*, Appl. Phys. Lett. **91**, 051904 (2007).

[80] A. J. Bennett, M. A. Pooley, R. M. Stevenson, M. B. Ward, R. B. Patel, A. Boyer de la Giroday, N. Sköld, I. Farrer, C. A. Nicoll, D. A. Ritchie, and A. J. Shields, *Electric-field-induced coherent coupling of the exciton states in a single quantum dot*, Nature Phys. **6**, 947-950 (2010).

[81] J. J. Finley, M. Sabathil, P. Vogl, G. Abstreiter, R. Oulton, A. I. Tartakovskii, D. J. Mowbray, M. S. Skolnick, S. L. Liew, A. G. Cullis, and M. Hopkinson, *Quantum-confined Stark shifts of charged exciton complexes in quantum dots*, Phys. Rev. B **70**, 201308(R) (2004).

[82] J. A. Barker and E. P. O'Reilly, *Theoretical analysis of electron-hole alignment in InAs-GaAs quantum dots*, Phys. Rev. B **61**, 13840 (2000).

[83] Z. L. Yuan, B. E. Kardynal, R. M. Stevenson, A. J. Shields, C. J. Lobo, K. Cooper, N. S. Beattie, D. A. Ritchie, and M. Pepper, *Electrically driven single-photon source*, Science **295**, 102-105 (2002).

[84] C. Y. Hung, T. E. Schlesinger, and M. L. Reed, *Piezoelectrically induced stress tuning of electro-optic devices*, Appl. Phys. Lett. **59**, 3598 (1991).

[85] T. Zander, A. Herklotz, S. Kiravittaya, M. Benyoucef, F. Ding, P. Atkinson, S. Kumar, J. D. Plumhof, K. Dörr, A. Rastelli, and O. G. Schmidt, *Epitaxial quantum dots in stretchable optical microcavities*, Opt. Express **17**, 22452 (2009).

[86] J. D. Plumhof, V. Křápek, F. Ding, K. D. Jöns, R. Hafenbrak, P. Klenovský, A. Herklotz, K. Dörr, P. Michler, A. Rastelli, and O. G. Schmidt, *Strain-induced anticrossing of bright exciton levels in single self-assembled GaAs/$Al_xGa_{1-x}As$ and $In_xGa_{1-x}As$/GaAs quantum dots*, Phys. Rev. B **83**, 121302(R) (2011).

[87] J. Zhang, F. Ding, E. Zallo, R. Trotta, B. Höfer, L. Han, S. Kumar, Y. H. Huo, A. Rastelli, and O. G. Schmidt, *A nanomembrane-based wavelength-tunable high-speed single-photon-emitting diode*, Nano Lett. **13**, 5808 (2013).

[88] W. Sheng and J.-P. Leburton, *Anomalous quantum-confined stark effects in stacked InAs/GaAs self-assembled quantum dots*, Phys. Rev. Lett. **88**, 167401 (2002).

[89] G. Ortner, M. Bayer, A. Larionov, V. B. Timofeev, A. Forchel, Y. B. Lyanda-Geller, T. L. Reinecke, P. Hawrylak, S. Fafard, and Z. Wasilewski, *Fine structure of excitons in InAs/GaAs coupled quantum dots: A sensitive test of electronic coupling*, Phys. Rev. Lett. **90**, 086404 (2003).

[90] G. Ortner, I. Yugova, A. Larionov, G. B. H. von Högersthal, M. Bayer, P. Hawrylak, S. Fafard, and Z. Wasilewski, *Experimental demonstration of coherent coupling of two quantum dots*, Physica E **26**, 281-285 (2005).

[91] G. Ortner, I. Yugova, G. B. H. von Högersthal, A. Larionov, H. Kurtze, D. R. Yakolev, M. Bayer, S. Fafard, Z. Wasilewski, P. Hawrylak, Y. B. Lyanda-Geller, T. L. Reinecke, A. Babinski, M. Potemski, V. B. Timofeev, and A. Forchel, *Fine structure in the excitonic emission of InAs/GaAs quantum dot molecules*, Phys. Rev. B **71**, 125335 (2005).

[92] I. Shtrichman, C Metzner, B. D. Gerardot, W. V. Shoenfeld, and P. M. Petroff, *Photoluminescence of a single InAs quantum dot molecule under applied electric field*, Phys. Rev. B **65**, 081303 (2002).

[93] A. Nazir, B. W. Lovett, S. D. Barrett, J. H. Reina, and G. A. D. Briggs, *Anticrossings in Förster coupled quantum dots*, Phys. Rev. B **71**, 045334 (2005).

[94] B. D. Gerardot, S. Strauf, M. J. A. de Dood, A. M. Bychkov, A. Badolato. K. Hennessy, E. L. Hu, D. Bouwmeester, and P. M. Petroff, *Photon statistics from coupled quantum dots*, Phys. Rev. Lett. **95**, 137403 (2005).

[95] M. Scheibner, I. V. Ponomarev, E. A. Stinaff, M. F. Doty, A. S. Bracker, C. S. Hellberg, T. L. Reinecke, and D. Gammon, *Photoluminescence spectroscopy of the molecular biexciton in vertically stacked InAs-GaAs quantum dot pairs*, Phys. Rev. Lett. **99**, 197402 (2007).

[96] M. Scheibner, M. Yakes, A. S. Bracker, I. V. Ponomarev, M. F. Doty, C. S. Hellberg, L. J. Whitman, T. L. Reinecke, and D. Gammon, *Optically mapping the electronic structure of coupled quantum dots*, Nature Phys. **4**, 291-295 (2008).

[97] H. J. Krenner, E. C. Clark, T. Nakaoka, M. Bichler, C. Scheurer, G. Abstreiter, and J. J. Finley, *Optically probing spin and charge interactions in a tunable artificial molecule*, Phys. Rev. Lett. **97**, 076403 (2006).

[98] M. Scheibner, M. F. Doty, I. V. Ponomarev, A. S. Bracker, E. A. Stinaff, V. L. Korenev, T. L. Reinecke, and D. Gammon, *Spin fine structure of optically excited quantum dot molecules*, Phys. Rev. B **75**, 245318 (2007).

[99] G. Bester, J. Shumway, and A. Zunger, *Theory of excitonic spectra and entanglement engineering in dot molecules*, Phys. Rev. Lett. **93**, 047401 (2004).

[100] G. Bester, A. Zunger, and J. Shumway, *Broken symmetry and quantum entanglement of an exciton in $In_xGa_{1-x}As/GaAs$ quantum dot molecules*, Phys. Rev. B **71**, 075325 (2005).

[101] M. Z. Maialle and M. H. Degani, *Mixed singlet-triplet trion states in quantum dot molecules: A spatial-dependent spin-splitting effect*, Phys. Rev. B **76**, 7 (2007).

[102] B. Szafran and F. M. Peeters, *Signatures of lateral coupling of double quantum dots in the exciton photoluminescence spectrum*, Phys. Rev. B **76**, 195442 (2007).

[103] M. F. Doty, M. Scheibner, I. V. Ponomarev, E. A. Stinaff, A. S. Bracker, V. L. Korenev, T. L. Reinecke, and D. Gammon, *Electrically tunable g factors in quantum dot molecular spin states*, Phys. Rev. Lett. **97**, 197202 (2006).

[104] M. F. Doty, J. I. Climente, M. Korkusinski, M. Scheibner, A. S. Bracker, P. Hawrylak, and D. Gammon, *Antibonding ground states in InAs quantum-dot molecules*, Phys. Rev. Lett. **102**, 047401 (2009).

[105] T. Unold, K. Mueller, C. Lienau, T. Elsaesser, and A. D. Wieck, *Optical control of excitons in a pair of quantum dots coupled by the dipole-dipole interaction*, Phys. Rev. Lett. **94**, 137404 (2005).

[106] L. Wang, A. Rastelli, S. Kiravittaya, M. Benyoucef, and O. G. Schmidt, *Self-assembled quantum dot molecules*, Adv. Mater. **21**, 2601 (2009).

[107] G. Muñoz-Matutano, M. Royo, J. I. Climente, J. Canet-Ferrer, D. Fuster, P. Alonso-González, I. Fernández-Martínez, J. Martínez-Pastor, Y. González, L. González, F. Briones, and B. Alén. *Charge control in laterally coupled double quantum dots*, Phys. Rev. B **84**, 041308(R) (2011).

[108] Z. R. Wasilewski, S. Fafard, and J. P. McCaffrey, *Size and shape engineering of vertically stacked self-assembled quantum dots*, J. Cryst. Growth **201-202**, 1131 (1999).

[109] J. M. Garcia, G. Medeiros-Ribeiro, K. Schmidt, T. Ngo, J. L. Feng, A. Lorke, J. Kotthaus, and P. M. Petroff, *Intermixing and shape changes during the formation of InAs self-assembled quantum dots*, Appl. Phys. Lett. **71**, 2014 (1997).

[110] G. Costantini, A. Rastelli, C. Manzano, P. Acosta-Diaz, R. Songmuang, G. Katsaros, O. G. Schmidt, and K. Kern, *Interplay between thermodynamics and kinetics in the capping of InAs/GaAs(001) quantum dots*, Phys. Rev. Lett. **96**, 226106 (2006).

[111] M. F. Doty, M. Scheibner, A. S. Bracker, and D. Gammon, *Single semiconductor quantum dots*, edited by P. Michler (Springer, Berlin, 2009).

[112] E. Madelung, *Die mathematischen Hilfsmittel des Physikers*, 2nd edition (Julius Springer, Berlin, 1925).

[113] A. Boyer de la Giroday, N. Sköld, I. Farrer, D. A. Ritchie, and A. J. Shields, *Excitonic couplings and Stark effect in individual quantum dot molecules*, J. Appl. Phys. **110**, 083511 (2011).

[114] A. Greilich, S. G. Carter, D. Kim, A. S. Bracker, and D. Gammon, *Optical control of one and two hole spins in interacting quantum dots*, Nature Photon. **5**, 702-708 (2011).

[115] H. Y. Ramírez and S.-J. Cheng, *Tunneling effects on fine-structure splitting in quantum-dot molecules*, Phys. Rev. Lett. **104**, 206402 (2010).

[116] J. Vanier, *Atomic clocks based on coherent population trapping: a review*, Appl. Phys. B **81**, 421 (2005).

[117] P. M. Boffey, The New York Times C1 (1 June 1982).

[118] *Molecular beam epitaxy*, edited by A. Y. Cho (AIP, New York, 1994).

[119] M. J. Kelly, *Low-dimensional semiconductors: Materials, physics, technology, devices* (Clarendon, Oxford, 1995).

[120] D. C. Tsui, H. L. Störmer, and A. C. Gossard, *Two-dimensional magnetotransport in the extreme quantum limit*, Phys. Rev. Lett **48**, 1559 (1982).

[121] http://www.physik.uni-kl.de/hillebrands/research/methods/molecular-beam-epitaxy.

[122] N. N. Ledentsov, *Growth processes and surface phase equilibria in molecular beam epitaxy*, Springer Tracts in Modern Physics **156** (Springer, Berlin, 1999).

[123] M. Hata, T. Isu, A. Watanabe, and Y. Katayama, *Real-time observation of molecular beam epitaxy growth on mesa-etched GaAs substrates by scanning microprobe reflection high-energy electron diffraction*, Appl. Phys. Lett. **56**, 2542 (1990).

[124] F. C. Frank and J. H. Van der Merwe, *One-dimensional dislocations. I. Static theory*, Proc. R. Soc. London Ser. A **198**, 205 (1949).

[125] M. Volmer and A. Weber, *Keimbildung in übersättigten Gebilden*, Z. Physik. Chem. **119**, 277 (1926).

[126] I. N. Stranski and L. Krastanow, *Zur Theorie der orientierten Ausscheidung von Ionenkristallen aufeinander*, Sitzungsber. Akad. Wiss., Math.-Naturwiss. **146**, 797 (1938).

[127] J. Klein, *Epitaktische Heterostrukturen aus dotierten Manganaten*, PhD thesis, University of Cologne (2001).

[128] C. W. Farley, G. J. Sullivan, M. J. Mondry, and D. L. Miller, *Arsenic flux interruptions-induced RHEED oscillations and measurements of As coverage on the growing (001) MBE GaAs surface*, J. Cryst. Growth **96**, 19 (1989).

[129] C. T. Foxon and B. A. Joyce, *Interaction kinetics of As_4 and Ga on {100} GaAs surfaces using a modulated molecular beam technique*, Surface Sci. **50**, 434 (1975).

[130] T. Kudo, T. Inoue, T. Kita, and O. Wada, *Real time analysis of self-assembled InAs/GaAs quantum dot growth by probing reflection high-energy electron diffraction chevron image*, J. Appl. Phys. **104**, 074305 (2008).

[131] P. B. Joyce, T. J. Krzyzewski, G. R. Bell, B. A. Joyce, and T. S. Jones, *Composition of InAs quantum dots on GaAs(001): Direct evidence for (In,Ga)As alloying*, Phys. Rev. B **58**, 15981(R) (1998).

[132] K. Watanabe, N. Koguchi, and Y. Gotoh, *Fabrication of GaAs quantum dots by modified droplet epitaxy*, Jpn. J. Appl. Phys., Part 2 **39**, L79 (2000).

[133] A. Hartmann, L. Loubies, F. Reinhardt, and E. Kapon, *Self-limiting growth of quantum dot heterostructures on nonplanar {111}B substrates*, Appl. Phys. Lett. **71**, 1314 (1997).

[134] A. Rastelli, S. Stufler, A. Schliwa, R. Songmuang, C. Manzano, G. Costantini, K. Kern, A. Zrenner, D. Bimberg, and O. G. Schmidt, *Hierarchical self-assembly of GaAs/AlGaAs quantum dots*, Phys. Rev. Lett. **92**, 166104 (2004).

[135] C. Heyn, A. Stemmann, T. Köppen, C. Strelow, T. Kipp, M. Grave, S. Mendach, and W. Hansen, *Dynamics of self-assembled droplet etching*, Appl. Phys. Lett. **95**, 173110 (2009).

[136] R. García and R. Pérez, *Dynamic atomic force microscopy methods*, Surf. Sci. Rep. **47**, 197-301 (2002).

[137] M. Shayegan, K. Karrai, Y. P. Shkolnikov, K. Vakili, E. P. De Poortere, and S. Manus, *Low-temperature, in situ tunable, uniaxial stress measurements in semiconductors using a piezoelectric actuator*, Appl. Phys. Lett. **83**, 5235 (2003).

[138] S.-E. Park and T. T. Shrout, *Ultrahigh strain and piezoelectric behavior in relaxor based ferroelectric single crystals*, J. Appl. Phys. **82**, 1804 (1997).

[139] M. D. Biegalski, K. Dörr, D. H. Kim, and H. M. Christen, *Applying uniform reversible strain to epitaxial oxide films*, Appl. Phys. Lett. **96**, 151905 (2010).

[140] C. Thiele, K. Dörr, O. Bilani, J. Rödel, and L. Schultz, *Influence of strain on the magnetisation and magneto electric effect in* $La_{0.7}A_{0.3}MnO_3$*/PMN-PT(001) (A=Sr,Ca)*, Phys. Rev. B **75**, 054408 (2007).

[141] A. Herklotz, J. D. Plumhof, A. Rastelli, O. G. Schmidt, L. Schultz, and K. Dörr, *Electrical characterization of PMN-28%PT(001) crystals used as thin-film substrates*, J. Appl. Phys. **108**, 094101 (2010).

[142] R. J. Warburton, C. Schäflein, D. Haft, F. Bickel, A. Lorke, K. Karrai, J. M. Garcia, W. Schoenfeld, and P. M. Petroff, *Optical emission from a charge-tunable quantum ring*, Nature **405**, 926-929 (2000).

[143] F. Ding, R. Singh, J. D. Plumhof, T. Zander, V. Křápek, Y. H. Chen, M. Benyoucef, V. Zwiller, K. Dörr, G. Bester, A. Rastelli, and O. G. Schmidt, *Tuning the exciton binding energies in single self-assembled InGaAs/GaAs quantum dots by piezoelectric-induced biaxial stress*, Phys. Rev. Lett. **104**, 067405 (2010).

[144] C. H. Tsau, S. M. Spearing, and M. A. Schmidt, *Fabrication of wafer-level thermocompression bonds*, J. Microelectromech. Syst. **11**, 641 (2002).

[145] R. Trotta, P. Atkinson, J. D. Plumhof, E. Zallo, R. O. Rezaev, S. Kumar, S. Baunack, J. R. Schröter, A. Rastelli, and O. G. Schmidt, *Nanomembrane quantum-light-emitting diodes integrated onto piezoelectric actuators*, Adv. Mater. **24**, 2668 (2012).

[146] P. Atkinson, E. Zallo, and O. G. Schmidt, *Independent wavelength and density control of uniform GaAs/AlGaAs quantum dots grown by infilling self-assembled nanoholes*, J. Appl. Phys. **112**, 054303 (2012).

[147] S. Kumar, R. Trotta, E. Zallo, J. D. Plumhof, P. Atkinson, A. Rastelli, and O. G. Schmidt, *Strain-induced tuning of the emission wavelength of high quality GaAs/AlGaAs quantum dots in the spectral range of the* ^{87}Rb D_2 *lines*, Appl. Phys. Lett. **99**, 161118 (2011).

[148] N. Akopian, R. Trotta, E. Zallo, S. Kumar, P. Atkinson, A. Rastelli, O. G. Schmidt, and V. Zwiller, *An artificial atom locked to natural atoms*, arXiv:1302.2005 (2013).

[149] R. Trotta, E. Zallo, C. Ortix, P. Atkinson, J. D. Plumhof, J. van den Brink, A. Rastelli, and O. G. Schmidt, *Universal recovery of the energy-level degeneracy of bright excitons in InGaAs quantum dots without a structure symmetry*, Phys. Rev. Lett. **109**, 147401 (2012).

[150] R. Trotta, E. Zallo, E. Mägerl, O. G. Schmidt, and A. Rastelli, *Independent control of exciton and biexciton energies in single quantum dots via electroelastic fields*, Phys. Rev. B **88**, 155312 (2013).

[151] R. Trotta, J. Wildmann, E. Zallo, O. G. Schmidt, and A. Rastelli, *Highly entangled photons from hybrid piezoelectric-semiconductor quantum dot devices*, Nano Lett. **4**, 3439 (2014).

[152] E. Zallo, P. Atkinson, A. Rastelli, and O. G. Schmidt, *Controlling the formation of quantum dot pairs using nanohole templates*, J. Cryst. Growth **338**, 232 (2012).

[153] E. Zallo, P. Atkinson, L. Wang, A. Rastelli, and O. G. Schmidt, *Epitaxial growth of lateral quantum dot molecules*, Phys. Status Solidi B **249**, 702 (2012).

[154] E. Zallo, R. Trotta, V. Křápek, Y. H. Huo, P. Atkinson, F. Ding, T. Šikola, A. Rastelli, and O. G. Schmidt, *Strain-induced active tuning of the coherent tunneling in quantum dot molecules*, Phys. Rev. B **89**, 241303(R) (2014).

[155] K. Brunner, G. Abstreiter, G. Böhm, G. Tränkle, and G. Weimann, *Sharp-line photoluminescence and two-photon absorption of zero-dimensional biexcitons in a GaAs/AlGaAs structure*, Phys. Rev. Lett. **73**, 1138 (1994).

[156] M. Jo, T. Mano, and K. Sakoda, *Two-step formation of gallium droplets with high controllability of size and density*, Cryst. Growth Des. **11**, 4647 (2011).

[157] V. Mantovani, S. Sanguinetti, M. Guzzi, E. Grilli, M. Gurioli, K. Watanabe, and N. Koguchi, *Low density GaAs/AlGaAs quantum dots grown by modified droplet epitaxy*, J. Appl. Phys. **96**, 4416 (2004).

[158] M. Abbarchi, C. A. Mastrandrea, T. Kuroda, T. Mano, K. Sakoda, N. Koguchi, S. Sanguinetti, A. Vinattieri, and M. Gurioli, *Exciton fine structure in strain-free GaAs/$Al_{0.3}Ga_{0.7}As$ quantum dots: Extrinsic effects*, Phys. Rev. B **78**, 125321 (2008).

[159] S. Kiravittaya, M. Benyoucef, R. Zapf-Gottwick, A. Rastelli, and O. G. Schmidt, *Ordered GaAs quantum dot arrays on GaAs(001): Single photon emission and fine structure splitting*, Appl. Phys. Lett. **89**, 233102 (2006).

[160] L. Wang, V. Křápek, F. Ding, F. Horton, A. Schliwa, D. Bimberg, A. Rastelli, and O. G. Schmidt, *Self-assembled quantum dots with tunable thickness of the*

wetting layer: Role of vertical confinement on interlevel spacing, Phys. Rev. B **80**, 085309 (2009).

[161] C. Heyn, M. Klingbeil, C. Strelow, A. Stemmann, S. Mendach, and W. Hansen, *Single-dot spectroscopy of GaAs quantum dots fabricated by filling of self-assembled nanoholes*, Nanoscale Res. Lett. **5**, 1633 (2010).

[162] D. Gammon, E. S. Snow, B.V. Shanabrook, D. S. Katzer, and D. Park, *Homogeneous linewidths in the optical spectrum of a single gallium arsenide quantum dot*, Science **273**, 87-90 (1996).

[163] M. Ghali, K. Ohtani, Y. Ohno, and H. Ohno, *Generation and control of polarization-entangled photons from GaAs island quantum dots by an electric field*, Nat. Commun. **3**, 661 (2012).

[164] N. Gisin and R. Thew, *Quantum communication*, Nature Photon. **1**, 165-171 (2007).

[165] P. Alonso-González, J. Martín-Sánchez, Y. González, B. Alén, D. Fuster, and L. González, *Formation of lateral low density In(Ga)As quantum dot pairs in GaAs nanoholes*, Cryst. Growth Des. **9**, 2525 (2009).

[166] C. Heyn, A. Stemmann, T. Köppen, Ch. Strelow, T. Kipp, M. Grave, S. Mendach, and W. Hansen, *Highly uniform and strain-free GaAs quantum dots fabricated by filling of self-assembled nanoholes*, Appl. Phys. Lett. **94**, 183113 (2009).

[167] J. Osaka, N. Inoue, Y. Mada, K. Yamada, and K. Wada, *In-situ observation of roughening process of MBE GaAs surface by scanning reflection electron microscopy*, J. Cryst. Growth **99**, 120 (1990).

[168] J. A. Venables, *Rate equation approaches to thin film nucleation kinetics*, Philos. Mag. **27**, 697 (1973).

[169] J. H. Neave, B. A. Joyce, and P. J. Dobson, *Dynamic RHEED observations of the MBE growth of GaAs*, Appl. Phys. A **34**, 179 (1984).

[170] J. W. Faust, A. Sagar, and H. F. John, *Molten metal etches for the orientation of semiconductors by optical techniques*, J. Electrochem. Soc. **109**, 824 (1962).

[171] H. C. Gatos and M.C. Lavine, *Characteristics of the (111) surfaces of the III-V inter metallic compounds*, J. Electrochem. Soc. **107**, 427 (1960).

[172] D. P. Miller, J. P. Harper, and T. R. Perry, *High-temperature oxidation and vacuum dissociation studies on the A{111} and B{$\bar{1}\bar{1}\bar{1}$} surfaces of gallium arsenide*, J. Electrochem. Soc. **108**, 1123 (1961).

[173] K. Shiraishi, *Ga adatom diffusion on an As-stabilized GaAs(001) surface via missing As dimer rows: First principles calculation*, Appl. Phys. Lett. **60**, 1363 (1992).

[174] T. Isu, M. Hata, and A. Watanabe, *Real-time μ-RHEED observations of GaAs surfaces during growth with alternating source supply*, J. Cryst. Growth **111**, 210 (1991).

[175] S. Koshiba, Y. Nakamura, M. Tsuchiya, H. Noge, H. Kano, Y. Nagamune, T. Noda, and H. Sakaki, *Surface diffusion processes in molecular beam epitaxial growth of GaAs and AlAs as studied on GaAs(001)-(111)B facet structures*, J. Appl. Phys. **76**, 4138 (1994).

[176] J. D. Plumhof, V. Křápek, L. Wang, A. Schliwa, D. Bimberg, A. Rastelli, and O. G. Schmidt, *Experimental investigation and modeling of the fine structure splitting of neutral excitons in strain-free GaAs/$Al_xGa_{1-x}As$ quantum dots*, Phys. Rev. B **81**, 121309(R) (2010).

[177] Y. H. Huo, A. Rastelli, and O. G. Schmidt, *Ultra-small excitonic fine structure splitting in highly symmetric quantum dots on GaAs (001) substrate*, Appl. Phys. Lett. **102**, 152105 (2013).

[178] L. O. Mereni, V. Dimastrodonato, R. J. Young, and E. Pelucchi, *A site-controlled quantum dot system offering both high uniformity and spectral purity*, Appl. Phys. Lett. **94**, 223121 (2009).

[179] H. J. Kimble, M. Dagenais, and L. Mandel, *Photon antibunching in resonance fluorescence*, Phys. Rev. Lett. **39**, 691 (1977).

[180] M. H. Baier, A. Malko, E. Pelucchi, D. Y. Oberli, and E. Kapon, *Quantum-dot exciton dynamics probed by photon-correlation spectroscopy*, Phys. Rev. B **73**, 205321 (2006).

[181] H. J. Kimble, *The quantum internet*, Nature **453**, 1023-1030 (2008).

[182] A. J. Hudson, R. M. Stevenson, A. J. Bennett, R. J. Young, C. A. Nicoll, P. Atkinson, K. Cooper, D. A. Ritchie, and A. J. Shields, *Coherence of an entangled exciton-photon state*, Phys. Rev. Lett. **99**, 266802 (2007).

[183] G. Juska, V. Dimastrodonato, L. O. Mereni, A. Gocalinska, and E. Pelucchi, *Towards quantum-dot arrays of entangled photon emitters*, Nature Photon. **7**, 527 (2013).

[184] R. Singh and G. Bester, *Lower bound for the excitonic fine structure splitting in self-assembled quantum dots*, Phys. Rev. Lett. **104**, 196803 (2010).

[185] J.-W. Pan, D. Bouwmeester, H. Weinfurter, and A. Zeilinger, *Experimental entanglement swapping: Entangling photons that never interacted*, Phys. Rev. Lett. **80**, 3891 (1998).

[186] A. Dousse, J. Suffczyński, A. Beveratos, O. Krebs, A. Lemaître, I. Sagnes, J. Bloch, P. Voisin, and P. Senellart, *Ultrabright source of entangled photon pairs*, Nature **466**, 217-220 (2010).

[187] T. Kuroda, T. Mano, N. Ha, H. Nakajima, H. Kumano, B. Urbaszek, M. Jo, M. Abbarchi, Y. Sakuma, K. Sakoda, I. Suemune, X. Marie, and T. Amand, *Symmetric quantum dots as efficient sources of highly entangled photons: Violation of Bell's inequality without spectral and temporal filtering*, Phys. Rev. B **88**, 041306(R) (2013).

[188] M. Missous and T. Taskin, *Very low resistance non-alloyed and in situ ohmic contacts to n-GaAs using delta-doped surface layers*, Semicond. Sci. Technol. **8**, 1848-1853 (1993).

[189] A. Jackson, P. Pinsukanjana, L. Coldren, and A. Gossard, *Monitoring Ga and In desorption and In surface segregation during MBE using atomic absorption*, J. Cryst. Growth **175-176**, 244 (1997).

[190] M. Gong, W. Zhang, G.-C. Guo, and L. He, *Exciton polarization, fine-structure splitting, and the asymmetry of quantum dots under uniaxial stress*, Phys. Rev. Lett. **106**, 227401 (2011).

[191] C. Santori, D. Fattal, M. Pelton, G. S. Solomon, and Y. Yamamoto, *Polarization-correlated photon pairs from a single quantum dot*, Phys. Rev. B **66**, 045308 (2002).

[192] D. F. V. James, P. G. Kwiat, W. J. Munro, and A. G. White, *Measurement of qubits*, Phys. Rev. A **64**, 052312 (2001).

[193] A. Peres, *Separability criterion for density matrices*, Phys. Rev. Lett. **77**, 1413 (1996).

[194] E. Placidi, F. Arciprete, V. Sessi, M. Fanfoni, F. Patella, and A. Balzarotti, *Step erosion during nucleation of InAs/GaAs(001) quantum dots*, Appl. Phys. Lett. **86**, 241913 (2005).

[195] X. Xu, D. A. Williams, and J. R. A. Cleaver, *Splitting of excitons and biexcitons in coupled InAs quantum dot molecules*, Appl. Phys. Lett. **86**, 012103 (2005).

[196] M. K. Yakes, C. D. Cress, J. G. Tischler, and A. S. Bracker, *Three-dimensional control of self-assembled quantum dot configurations*, ACS Nano **4**, 3877 (2010).

[197] P. S. Wong, G. Balakrishnan, N. Nuntawong, J. Tatebayashi, and D. L. Huffaker, *Controlled InAs quantum dot nucleation on faceted nanopatterned pyramids*, Appl. Phys. Lett. **90**, 183103 (2007).

[198] R. Songmuang, S. Kiravittaya, and O. G. Schmidt, *Formation of lateral quantum dot molecules around self-assembled nanoholes*, Appl. Phys. Lett. **82**, 2892 (2003).

[199] H. Heidemeyer, C. Müller, and O. G. Schmidt, *Highly ordered arrays of In(Ga)As quantum dots on patterned GaAs(001) substrates*, J. Cryst. Growth **261**, 444 (2004).

[200] S. Suraprapapich, Y. M. Shen, V. A. Odnoblyudov, Y. Fainman, S. Panyakeow, and C. W. Tu, *Self-assembled lateral Bi-quantum-dot molecule formation by gas-source molecular beam epitaxy*, J. Cryst. Growth **301**, 735 (2007).

[201] O. G. Schmidt, Ch. Deneke, S. Kiravittaya, R. Songmuang, H. Heidemeyer, Y. Nakamura, R. Zapf-Gottwick, C. Müller, and N. Y. Jin-Phillip, *Self-assembled nanoholes, lateral quantum-dot molecules, and rolled-up nanotubes*, IEEE J. Sel. Top. Quantum Electron. **8**, 1025 (2002).

[202] P. Atkinson, M. B. Ward, S. P. Bremner, D. Anderson, T. Farrow, G. A. C. Jones, A. J. Shields, and D. A. Ritchie, *Site-control of InAs quantum dots using ex-situ electron-beam lithographic patterning of GaAs substrates*, Jpn. J. Appl. Phys. **45**, 2519 (2006).

[203] P. Atkinson, O. G. Schmidt, S. P. Bremner, and D. A. Ritchie, *Formation and ordering of epitaxial quantum dots*, C. R. Phys. (France) **9**, 788 (2008).

[204] D. Leonard, K. Pond, and P. M. Petroff, *Critical layer thickness for self-assembled InAs islands on GaAs*, Phys. Rev. B **50**, 11687 (1994).

[205] B. Lita, R. S. Goldman, J. D. Phillips, and P. K. Bhattacharya, *Interdiffusion and surface segregation in stacked self-assembled InAs/GaAs quantum dots*, Appl. Phys. Lett. **75**, 2797 (1999).

[206] M. Abramowitz and I. A. Stegun, *Handbook of mathematical functions with formulas, graphs and mathematical tables* (Dover Publications, NewYork, 1972).

[207] A. Palma, E. Semprini, A. Talamo, and N. Tomassini, *Diffusion constant of Ga, In and As adatoms on GaAs(001) surface: Molecular dynamics calculations.*, Mat. Sci. and Engin. B **37**, 135 (1996).

[208] X. Q. Shen and T. Nishinaga, *Inter-surface diffusion of In on (111)A-(001) InAs nonplanar substrates in molecular beam epitaxy*, J. Cryst. Growth **146**, 374 (1995).

[209] G. R. Bell, T. S. Jones, and B. A. Joyce, *Direct observation of anisotropic step activity on GaAs(001)*, Surf. Sci. **429**, L492 (1999).

[210] D. G. Hill, K. L. Lear, and J. S. Harris, Jr., *Two selective etching solutions for GaAs on InGaAs and GaAs/AlGaAs on InGaAs*, J. Electrochem. Soc. **137**, 2912 (1990).

[211] A. Greilich, Ş. C. Bădescu, D. Kim, A. S. Bracker, and D. Gammon, *Optical measurement and modeling of interactions between two hole spins or two electron spins in coupled InAs quantum dots*, Phys. Rev. Lett. **110**, 117402 (2013).

[212] C. Zener, *Non-adiabatic crossing of energy levels*, Proc. R. Soc. Lond. A **137**, 696-702 (1932).

[213] Y. Hu, H. O. H. Churchill, D. J. Reilly, J. Xiang, C. M. Lieber, and C. M. Marcus, *A Ge/Si heterostructure nanowire-based double quantum dot with integrated charge sensor*, Nat. Nanotechnol. **2**, 622-625 (2007).

[214] G. Burkard, G. Seelig, and D. Loss, *Spin interactions and switching in vertically tunnel-coupled quantum dots*, Phys. Rev. B **62**, 2581 (2000).

[215] J. Planelles, J. I. Climente, F. Rajadell, M. F. Doty, A. S. Bracker, and D. Gammon, *Effect of strain and variable mass on the formation of antibonding hole ground states in InAs quantum dot molecules*, Phys. Rev. B **82**, 155307 (2010).

[216] F. M. Ross, J. Tersoff, and R. M. Tromp, *Coarsening of self-assembled Ge quantum dots on Si(001)*, Phys. Rev. Lett. **80**, 984 (1998).

[217] F. H. L. Koppens, J. A. Folk, J. M. Elzerman, R. Hanson, L. H. Willems van Beveren, I. T. Vink, H. P. Tranitz, W. Wegscheider, L. P. Kouwenhoven, and L. M. K. Vandersypen, *Control and detection of singlet-triplet mixing in a random nuclear field*, Science **309**, 1346-1350 (2007).

[218] P. W. Fry, I. E. Itskevich, D. J. Mowbray, M. S. Skolnick, J. J. Finley, J. A. Barker, E. P. O'Reilly, L. R. Wilson, I. A. Larkin, P. A. Maksym, M. Hopkinson, M. Al-Khafaji, J. P. R. David, A. G. Cullis, G. Hill, and J. C. Clark, *Inverted electron-hole alignment in InAs-GaAs self-assembled quantum dots*, Phys. Rev. Lett. **84**, 733 (2000).

[219] R. M. Stevenson, R. M. Thompson, A. J. Shields, I. Farrer, C. J. Lobo, D. A. Ritchie, M. L. Leadbeater, and M. Pepper, *Exciton complexes in individual quantum dots as a single-photon source*, Physica E **13**, 423-426 (2002).

[220] J. Wang, D. Shang, H. Mao, J. Yu, Q. Zhao, P. Yang, and H. Xing, *Strain effects on resonant parameters in asymmetric $In_{1-x}Ga_xAs$ quantum dot molecules*, Physica B **408**, 98 (2013).

[221] G. Bester, X. Wu, D. Vanderbilt, and A. Zunger, *Importance of second-order piezoelectric effects in zinc-blende semiconductors*, Phys. Rev. Lett. **96**, 187602 (2006).

[222] N. Sköld, A. Boyer de la Giroday, A. J. Bennett, I. Farrer, D. A. Ritchie, and A. J. Shields, *Electrical control of the exciton fine structure of a quantum dot molecule*, Phys. Rev. Lett. **110**, 016804 (2013).

[223] M. F. Doty, J. I. Climente, A. Greilich, M. Yakes, A. S. Bracker, and D. Gammon, *Hole-spin mixing in InAs quantum dot molecules*, Phys. Rev. B **81**, 035308 (2010).

[224] R. N. Bhargava and M. I. Nathan, *Stress dependence of photoluminescence in GaAs*, Phys. Rev. **161**, 695 (1967).

[225] J. E. Avron, G. Bisker, D. Gershoni, N. H. Lindner, E. A. Meirom, and R. J. Warburton, *Entanglement on demand through time reordering*, Phys. Rev. Lett. **100**, 120501 (2008).

Declaration

Hiermit erkläre ich an Eides statt, dass ich die am heutigen Tag eingereichte Dissertation zum Thema "Control of electronic and optical properties of single and double quantum dots via electroelastic fields" unter der Betreuung von Herrn Prof. Dr. Oliver G. Schmidt selbständig erarbeitet, verfasst und Zitate kenntlich gemacht habe. Andere als die angegebenen Hilfsmittel wurden von mir nicht benutzt.
Die Dissertation wurde in dieser oder ähnlicher Form an keiner anderen Stelle zum Zwecke eines Promotionsverfahrens eingereicht. Es wurde von mir bisher kein Promotionsverfahren an anderer Stelle beantragt.

Dresden 08. October 2014

(Eugenio Zallo)

Publications, contributed talks, posters

Publications

- F. J. R. Schülein, **E. Zallo**, P. Atkinson, O. G. Schmidt, R. Trotta, A. Rastelli, A. Wixforth, and H. J. Krenner. *Fourier synthesis and timbre tuning of radio frequency nanomechanical pulses.* (accepted in Nat. Nanotechnol.)

- **E. Zallo**, R. Trotta, V. Křápek, Y. H. Huo, P. Atkinson, F. Ding, T. Šikola, A. Rastelli, and O. G. Schmidt. *Strain-induced active tuning of the coherent tunneling in quantum dot molecules.* Phys. Rev. B **89**, 241303(R) (2014).

- R. Trotta, J. Wildmann, **E. Zallo**, O. G. Schmidt, and A. Rastelli. *Highly entangled photons from hybrid piezoelectric-semiconductor quantum dot devices.* Nano Lett. **4**, 3439 (2014).

- M. Gong, B. Höfer, **E. Zallo**, R. Trotta, J. Luo, O. G. Schmidt, and C. Zhang. *Statistical properties of exciton fine structure splitting and polarization angle in quantum dot ensembles.* Phys. Rev. B **89**, 205312 (2014).

- D. Grimm, R. B. Wilson, B. Teshome, S. Gorantla, M. H. Rümmeli, T. Bublat, **E. Zallo**, G. Li, D. G. Cahill, and O. G. Schmidt. *Thermal conductivity of hybrid semiconducting/metal superlattices.* Nano Lett. **14**, 2387 (2014).

- S. Kumar, **E. Zallo**, Y. H. Liao, P. Y. Lin, J. D. Plumhof, P. Atkinson, F. Ding, R. Trotta, S. Cheng, A. Rastelli, and O. G. Schmidt. *Heavy hole-light hole mixing dependent polarization properties of neutral excitonic states of GaAs/AlGaAs quantum dots.* Phys. Rev. B **89**, 115309 (2014).

- Y. H. Huo, B. J. Witek, S. Kumar, J. R. Cardenas, J. X. Zhang, N. Akopian, R. Singh, **E. Zallo**, R. Grifone, D. Kriegner, R. Trotta, F. Ding, J. Stangl, V. Zwiller, G. Bester, A. Rastelli, and O. G. Schmidt. *A light-hole exciton in a quantum dot.* Nature Phys. **10**, 46-51 (2014).

- J. Zhang, F. Ding, **E. Zallo**, B. Hoefer, L. Hang, S. Kumar, R. Trotta, A. Rastelli, and O. G. Schmidt. *A nanomembrane-based wavelength controllable high speed single-photon-emitting diode.* Nano Lett. **13**, 5808 (2013).

- R. Trotta, **E. Zallo**, E. Magerl, O. G. Schmidt, and A. Rastelli. *Indipendent control of exciton and biexciton energies in single quantum dots via elecro-elastic fields.* Phys. Rev. B **88**, 155312 (2013)

- J. D. Plumhof, R. Trotta, V. Křápek, **E. Zallo**, P. Atkinson, S. Kumar, A. Rastelli, and O. G. Schmidt. *Tuning of the valence band mixing of excitons confined in GaAs/AlGaAs quantum dots via piezoelectric-induced anisotropic strain.* Phys. Rev. B **87**, 075311 (2013)

- N. Akopian, R. Trotta, **E. Zallo**, A. Rastelli, O. G. Schmidt, and V. Zwiller. *Artificial atoms locked to natural atoms.* arxiv.org/abs/1302.2005 (2013).

- R. Trotta, **E. Zallo**, C. Ortix, P. Atkinson, J. D. Plumhof, J. v. d. Brink, A. Rastelli, and O. G. Schmidt. *Universal recovery of the bright-exciton level-degeneracy in quantum dots without structural symmetry.* Phys. Rev. Lett. **109**, 147401 (2012); (Editors' suggestion and selected for a Viewpoint in Physics, see physics.aps.org/articles/v5/109)

- P. Atkinson, **E. Zallo**, and O. G. Schmidt. *Indipendent wavelength and density control of uniform GaAs/AlGaAs quantum dots grown by infilling self-assembled nanoholes.* J. Appl. Phys. **112**, 054303 (2012)

- R. Trotta, P. Atkinson, J. D. Plumhof, **E. Zallo**, R. Rezaev, S. Kumar, S. Baunack, J. Schröter, A. Rastelli, and O. G. Schmidt. *Nanomembrane quantum-light-emitting diodes integrated onto piezoelectric actuators.* Adv. Mat. **24**, 2668 (2012)

- **E. Zallo**, P. Atkinson, L. Wang, A. Rastelli, and O. G. Schmidt. *Epitaxial growth of lateral quantum dot molecules.* Phys. Status Solidi B **249**, 702 (2012)

- A. Rastelli, F. Ding, J. D. Plumhof, S. Kumar, R. Trotta, Ch. Deneke, A. Malachias, P. Atkinson, **E. Zallo**, T. Zander, A. Herkloltz, R. Singh, V. Křápek, J. R. Schröter, S. Kiravittaya, M. Benyoucef, R. Hafenbrak, K. D. Jöns, D. J. Thurmer, D. Grimm, G. Bester, K. Dörr, P. Michler, and O. G. Schmidt. *Controlling quantum dot emission by integration of semiconductor nanomembranes onto piezoelectric actuators.* Phys. Status Solidi B **249**, 687 (2012)

- **E. Zallo**, P. Atkinson, A. Rastelli, and O. G. Schmidt. *Controlling the formation of quantum dot pairs using nanohole templates.* J. Cryst. Growth **338**, 232 (2012)

- S. Kumar, R. Trotta, **E. Zallo**, J. D. Plumhof, P. Atkinson, A. Rastelli, and O. G. Schmidt. *Strain-induced tuning of the emission wavelength of high quality GaAs/AlGaAs quantum dots in the spectral range of the ^{87}Rb D_2 lines.* Appl. Phys. Lett. **99**, 161118 (2011)

- E. Placidi, **E. Zallo**, M. Fanfoni, F. Arciprete, F. Patella and A. Balzarotti. *Comparative study of low temperature growth of InAs and InMnAs quantum dots.* Nanotechnology **22**, 195602 (2011)

Proceedings

- *Single quantum dot locked to atomic transition.* 2012 Conference on lasers and electro-optics (CLEO). San Jose, CA, May 06-11, 2012
- *Reshaping the optical properties of quantum dots via strain and electric fields.* 25th International Conference on Indium Phosphide and Related Materials (IPRM), Kobe, Japan, May 19-23, 2013.

Contributed talks

- **E. Zallo**. *Control of electronic and optical properties of single and double quantum dots via growth and electroelastic fields.* Invited, Cavendish Laboratory, University of Cambridge, Cambridge, UK, Dec 10, 2014.
- **E. Zallo**. *Control of electronic and optical properties of single and double quantum dots via growth and electroelastic fields.* Invited, Paul-Drude-Institut für Festkörperelektronik, Berlin, Germany, Nov 11, 2014.
- **E. Zallo**. *Strain-induced active tuning of the coherent tunneling in quantum dot molecules.* 8th International Conference on Quantum Dots, Pisa, Italy, May 11-16, 2014.
- **E. Zallo**. *Strain-induced active tuning of the coherent tunneling in quantum dot molecules.* 78th Annual Meeting of the DPG and DPG Spring Meeting of the SAMOP, Symposium Quantum Repeater, Berlin, Germany, Mar 17-18, 2014.
- **E. Zallo**. *Strain-induced active tuning of the coherent tunneling in quantum dot molecules.* Invited, University of Rome *Tor Vergata*, Rome, Italy, Oct 11, 2013.
- **E. Zallo**. *Strain-induced active tuning of the coherent tunneling in quantum dot molecules.* Deutscher MBE Wokshop, IFW Dresden, Dresden, Germany, Sep 30, 2013.
- **E. Zallo**, P. Atkinson, Y. Huo, R. Trotta, S. Kumar, J. D. Plumhof, A. Rastelli, and O. G. Schmidt. *Fine tuning of the light emission of GaAs/AlGaAs quantum dots grown by infilling self-assembled nanoholes.* Workshop "Site controlled Epitaxy 2012", Heraklion (Crete), Greece, Apr 30, 2012.
- **E. Zallo**, P. Atkinson, R. Trotta, S. Kumar, J. D. Plumhof, A. Rastelli, and O. G. Schmidt. *Tuning the emission of GaAs quantum dots.* 75th Annual Meeting of the DPG and DPG Spring Meeting, Dresden, Germany, Mar 18, 2011.

Posters

- **E. Zallo**, R. Trotta, V. Křápek, Y. H. Huo, P. Atkinson, F. Ding, A. Rastelli, and O. G. Schmidt. *Strain-induced active tuning of the coherent tunneling in*

quantum dot molecules. Sino-German Symposium. Würzburg, Germany, Sep 16-21, 2013.

- **E. Zallo**, P. Atkinson, A. Rastelli, and O. G. Schmidt. *Epitaxial growth of lateral quantum dot molecules*. Workshop of the DFG Research Group 'Positioning a single nanosctructure', Villa Vigoni (Como), Italy, Sep 12-14, 2011.

- **E. Zallo**, P. Atkinson, A. Rastelli, and O. G. Schmidt. *Controlling the formation of quantum dot molecules using nanohole templates*. 16th International Conference on Molecular Beam Epitaxy, Berlin, Germany, Ago 22-27, 2010.

Summary of my contributions to the publication list

Phys. Rev. B **89**, 241303(R) (2014): Sample growth and optimisation, AFM measurement, PL characterisation, device processing, PL measurement of the devices, data analysis, theoretical modelling, manuscript writing.
Nano Lett. **4**, 3439 (2014): Sample growth and optimisation.
Phys. Rev. B **89**, 205312 (2014): Sample growth and optimisation, data analysis.
Nano Lett. **14**, 2387 (2014): Sample growth and optimisation.
Phys. Rev. B **89**, 115309 (2014): Sample growth and optimisation, AFM measurement, PL characterisation, data analysis, writing part of the manuscript.
Nature Phys. **10**, 46-51 (2014): Sample growth and optimisation.
Nano Lett. **13**, 5808 (2013): Sample growth and optimisation, data analysis.
Phys. Rev. B **88**, 155312 (2013): Sample growth and optimisation, device processing, PL measurement of some devices, data analysis, writing part of the manuscript.
Phys. Rev. B **87**, 075311 (2013): Sample growth and optimisation.
arxiv.org/abs/1302.2005 (2013): Sample growth and optimisation, AFM measurement, PL characterisation.
Phys. Rev. Lett. **109**, 147401 (2012): Sample growth and optimisation, PL characterisation, PL measurement of devices, data analysis.
J. Appl. Phys. **112**, 054303 (2012): Sample growth and optimisation, AFM measurement, PL characterisation, data analysis, writing part of the manuscript.
Adv. Mat. **24**, 2668 (2012): Sample growth and optimisation.
Phys. Status Solidi B **249**, 702 (2012): Sample growth and optimisation, AFM measurement, data analysis, manuscript writing.
Phys. Status Solidi B **249**, 687 (2012): Sample growth and optimisation, data analysis.
J. Cryst. Growth **338**, 232 (2012): Sample growth and optimisation, AFM measurement, data analysis, theoretical modelling, manuscript writing.
Appl. Phys. Lett. **99**, 161118 (2011): Sample growth and optimisation, AFM measurement, PL characterisation, data analysis, writing part of the manuscript.
Nanotechnology **22**, 195602 (2011): Sample growth and optimisation, AFM measurement, data analysis, theoretical modelling.

Curriculum vitae

Personal information:

Name:	Eugenio Zallo
Born:	September 12, 1983
Place of birth:	Frascati (Rome), Italy
Citizenship:	Italian

Education:

Jul 2002:	Classical lyceum of Frascati (Rome) *Marco Tullio Cicerone* High school diploma (classical studies)
2002-2007:	University of Rome *Tor Vergata*, Rome Studies of physics
May 2007:	Degree: B.Sc. (Laurea Triennale) in Physics (108/110) Thesis: *Theory and applications of ricorsive method of Lanczos-Haydock* Supervisor: Prof. Michele Cini
2007-2010:	University of Rome *Tor Vergata*, Rome. Studies of condensed matter physics
Jan 2010:	Degree: M.Sc. (Laurea Specialistica) in Physics (110/110 summa cum laude) Thesis: *Nucleation and growth of InMnAs quantum dots on GaAs(001) surfaces* Supervisors: Dr. Ernesto Placidi and Prof. Adalberto Balzarotti
2010-2015:	Leibniz Institute for Solid State and Materials Research Dresden, Dresden Institute for Integrative Nanosciences, Scientific employee
March 2015:	Degree: Dr. rer. nat. (PhD) at Technische Universität Chemnitz, Chemnitz Thesis: *Control of electronic and optical properties of single and double quantum dots via electroelastic fields* Supervisors: Prof. Dr. Oliver G. Schmidt and Prof. Dr. Armando Rastelli